Technische Universität München
TUM School of Natural Sciences

SPATIOTEMPORAL COMPLEXITY IN A BIRHYTHMIC SYSTEM: AN EXPERIMENTAL STUDY

ANTON PATRICIO ROBERT TOSOLINI

Vollständiger Abdruck der von der TUM School of Natural Sciences der Technischen Universität München zur Erlangung eines

Doktors der Naturwissenschaften (Dr. rer. nat)

genehmigten Dissertation.

Vorsitz: Prof. Dr. Martin Zacharias

Prüfer*innen der Dissertation:
1. Prof. Dr. Katharina Krischer
2. Prof. Dr. Oliver Steinbock

Die Dissertation wurde am 20.04.2023 bei der Technischen Universität München eingereicht und durch die TUM School of Natural Sciences am 12.07.2023 angenommen.

SPATIOTEMPORAL COMPLEXITY IN A BIRHYTHMIC SYSTEM: AN EXPERIMENTAL STUDY

ANTON TOSOLINI

Dissertation
Nonequilibrium Chemical Physics - Department of Physics
Technical University of Munich

SUPERVISOR:
Prof. Dr.Katharina Krischer

ABSTRACT

We investigate various spatiotemporal phenomena during the oscillatory electrodissolution of silicon in a fluoride-containing electrolyte using electrochemical measurements, combined with a spatially resolved ellipsometric imaging set-up.

The work is divided into two parts. First we examine the behaviour of p-doped working electrodes, which display spatially homogenous oscillations. We show that there are two distinct types of periodic oscillations which are separated in the parameter plane by a region of more complex oscillations. Within the region of complex oscillations, there exist two bistable branches, each connected to one of the two limit cycles, and each following a distinct path towards chaos. We suggested that the complex oscillations arise due to an intrinsic coupling of the two limit cycles via a shared variable and identified the magnitude of the resistance, inserted into the external circuit, to play an important role for this coupling.

In the second part we turn our focus towards n-doped working electrodes for which spatial symmetry breaking can be observed. We present the different spatiotemporal patterns typically found in the system and connect them with the respective limit cycle to which they belong. We subsequently investigate the role of the two main coupling parameters, the external resistance and the illumination intensity, on the spatial coherence and temporal complexity of dynamics. We confirm once more, that, apart from the homogenising linear global coupling, the external resistor causes an intrinsic coupling between the two limit cycles, resulting in complex and even chaotic temporal behaviour. We also demonstrate that the reduction of the illumination intensity causes pattern formation and decreases the spatial coherence of the dynamics.

ACKNOWLEDGMENTS

I want to thank Prof. Dr. Katharina Krischer for her supervision and for giving me the opportunity to write my dissertation in her group.

I also want to thank Dr. Konrad Schönleber for his mentoring and for always being available to give helpful advice.

In particular, I want to express my gratitude to Dr. Maximilian Patzauer for our many fruitful discussions on our shared experimental setup and our respective research. But also for the non-work related discussions and activities which have always been a lot of fun.

Special thanks also go to Dr. Sindre Haugland for the many interesting discussions and for his patience in providing me with insights into his research. This enabled us to discover parallels between my measurements and his theoretical work, which allowed me to contribute some experimental findings to his impressive research.

I also want to thank Dr. Felix Kemeth for his support and patience in helping me in the beginning of my programming efforts.

I want to express my gratitude to Yukiteru Murakami for his help with the calibration of the illumination setup as part of his master's thesis, which I supervised during this doctoral project.

My thanks also goes to Juliane Wiehl for her many interesting work-related and unrelated consultations.

I would like to thank Dr. Malo Duportal, for sharing his interesting insights into the physical properties of oxides. His inspiring motivation to solve scientific riddles helped to uncover some of the hitherto unknown physiochemical properties in our system, which might be of great help for future projects on this topic. Apart from that it was a lot of fun to share the office with him.

I also want to thank Siegfried Schreier for his help in setting up a "Laser box" to increase the safety of my experimental setup.

In addition want to thank Seungjae Lee for sharing his office with me and always taking his time to patiently discuss theoretical concepts.

The balance between fruitful collaboration and and off-topic but welcome distractions was to a large part the spirit of this group which made the work here especially enjoyable. Therefore I want to thank the entire group.

In addition I want to thank Denice for her support and patience, especially during the last part of this project. And finally I want to thank my Mother for always supporting me in my decisions and always being there for me. It was especially the support from Denice and my Mother which helped me to pursue my goals.

CONTENTS

1

EMERGENCE OF COMPLEXITY

Mankind has always tried to predict or even control the outcome of certain events. In the ancient Greece it were thinkers and philosophers like Thales of Miletus or Pythagoras of Samos who tried to foresee the movement of the stars and laid the foundation of mathematics and astronomy. But a good explanation for the movement of an object and the mathematical tools to describe its trajectory were missing until Newton set a milestone for the research on dynamics in the middle of the 17th century. He invented differential equations and derived his laws of motion and gravitation which allowed him to explain Kepler's laws of planetary motion and especially solving the two body problem [62, 92, 100] .

This was a huge success and, one thought, one had the mathematical tools and theoretical framework to find the solutions for ever more complex problems. But unfortunately, as it turned out, larger systems often display a complexity which cannot be described by a theory which relies on linear superposition. If we stay at the description of planetary motion for example, just adding a third body to the two body system, hence considering the three body problem, turned out to be impossible to be solved analytically [92]. The three body system represents nicely the majority of systems found in nature, as it shows nonlinear effects which make it impossible to find analytical solutions for the trajectories of their variables.

It was Poincaré who demonstrated at the end of the 19th century that, in order to describe this kind of systems, one needs to find the answer to different questions than usually asked. Instead of asking for a solution of the system at all times he would rather ask where the system would end up after infinite time has passed [92]. More specifically he developed a geometrical approach which allowed him to figure out if a solution of the system is stable or not, i.e. whether the trajectory of a system converges towards the solution or diverges. This helped him to find answers to important questions of the three body problem and laid the foundation of the studies of nonlinear dynamics [21, 73].

The nonlinear dynamics approach to study a system is often to find its long time behaviour. One starts to search for steady states in a system, which are so-called fixed points in phase space. The phase space is spanned by all the variables which are essential to describe the dynamics of the system and is thus the space in which any trajectory of the system is embedded. However, the long time behaviour of a system is not necessary a steady state, hence a fixed point in the phase space, but can be of different dimension and geometrical shape. The long time behaviour of a system for a given set of parameters lives on an invariant subset of the phase space which is called attractor, as a trajectory would converge towards it. Hence an attractor is stable, in contrast to repellers which are unstable, and thus a trajectory would diverge from them. Among others, the long time behaviour of a system can be periodic, which is displayed as a so called limit cycle in phase space [72, 92]. If there is more than one incommensurable frequency there are quasiperiodic attractors which live on the surface of tori, but also strange attractors exist, which show locally exponential separation of close by trajectories and thus render the motion chaotic.

Often in nonlinear systems we have the case that for a given set of parameters there is not only one stable state, i.e. one attractor on which the system settles but two or more attractors, hence the system is bi- or multi-stable. On which attractor the system will end up, strongly depends on the initial conditions [71]. Such bi- or multistabilities can have all kinds of different configurations. The simplest one is the coexistence of two or more stable fixed points, i.e. steady states, which can be found in systems described by evolution equations with three or more roots [92]. Another one is the bistability between a steady state and an oscillatory state as can be found in the dynamics of a Josephson junction [52]. Among others there is also the possibility of two oscillatory states being stable for the same parameters. A system with two coexistent stable limit cycles is referred to as birhythmic [28] and in the case of two coexisting strange attractors one speaks of bichaoticity [87].

Birhythmicity and multi-rhythmicity has caught a lot of attention and has been proven to be important in many biological systems [38]. It has most commonly been reported in theoretical studies, such as in studies on the electrical activity of periodically stimulated cardiac cells [40, 69, 104] or on nerve cells, which are regulated through mutual inhibition [15, 19, 99], but also experimental studies have reported birhythmic behaviour for example on the light-entrainable and methamphetamin-sensitive circadian oscillators [68].

But birhythmicity is not limited to biological systems. The first time it was reported in 1976, when it was discussed in a model for a continuous stirred tank reactor with consecutive exothermic reactions [27]. The first experimental finding of birhythmicity has been reported in a Q-switched gas Laser in 1982 [6]. The first finding in a experimental chemical system has been in a system of two chemical oscillators which are coupled through a common species [4, 5]. Another example is the exothermic oxidation of hydrogen in a continuously stirred tank reactor [14, 43]. Other birhythmic experimental systems include electronic oscillators [16], the Belousov–Zhabotinsky reaction in a stirred flow reactor, [48, 54, 77] and acetaldehyde oxidation in a continuously stirred tank reactor [39].

In theoretical studies of normal form type equations birhythmicity has been found in studies on septic van der Pol oscillators [8, 103] and model equations describing an energy harvesting system [17]. Models of two-frequency oscillators were demonstrated to support chimera states [76]. The same is true for bistable phase models [105]. In spatially extended systems, birhythmicity has so far only been investigated in theoretical works. Stich et al. [89, 90] investigated a reaction-diffusion system close to a supercritical pitchfork-Hopf bifurcation near the onset of birhythmicity. They constructed this system by coupling the complex Ginzburg-Landau equation (CGLE), which can be seen as the normal form for an oscillatory reaction-diffusion system close to the Hopf bifurcation [34], to an equation describing an imperfect pitchfork bifurcation. They found self-organised target patterns to be a generic kind of spatiotemporal patterns in the presence of birhythmicity. Shortly after, they presented a more detailed investigation of the emergence of wave sinks and sources in the CGLE with a controlled local shift in the oscillation frequency [91]. Later it was shown that a birhythmic medium can also exhibit turbulent dynamics and even chimera states for certain parameters [13, 35].

The experimental system in the centre of this Thesis, i.e. the oscillatory electrodissolution of silicon (Si), is a system exhibiting birhythmicity and spatiotemporal dynamics. It constitutes a reaction-diffusion system and thus, the theoretical studies of reaction-diffusions systems modelled by the CGLE also have a certain significance for our work. The electrodissolution of silicon electrodes in a fluoride containing electrolyte can be split in two processes. In a first step Si is electrochemically oxidised in one of the following two processes [55, 96, 97].

$$\begin{aligned} \mathrm{Si} + 2\mathrm{H_2O} + \gamma \mathrm{h}^+ &\longrightarrow \mathrm{Si(OH)_2} + 2\mathrm{H}^+ + (2-\gamma)\mathrm{e}^- \\ \mathrm{Si(OH)_2} &\longrightarrow \mathrm{SiO_2} + \mathrm{H_2} \end{aligned} \tag{1.1}$$

or

$$\begin{aligned} \mathrm{Si} + 4\mathrm{H_2O} + \gamma \mathrm{h}^+ &\longrightarrow \mathrm{Si(OH)_4} + 4\mathrm{H}^+ + (4-\gamma)\mathrm{e}^- \\ \mathrm{Si(OH)_4} &\longrightarrow \mathrm{SiO_2} + 2\mathrm{H_2O} \end{aligned} \tag{1.2}$$

where γ is the number of valence band holes involved in the electrochemical oxidation step. Eq.1.1 presents the divalent case and Eq.1.2 presents the tetravalent case. Note that the respective second steps of Eq.1.1 and 1.2 are purely chemical.

Subsequently, the formed $\mathrm{SiO_2}$ is etched by a fluoride species in a purely chemical reaction according to one of the following equations [22].

$$SiO_2 + 6HF \longrightarrow SiF_6^{2-} + 2H_2O + 2H^+ \tag{1.3}$$

$$SiO_2 + 3HF_2^- + H^+ \longrightarrow SiF_6^{2-} + 2H_2O \tag{1.4}$$

$$SiO_2 + 2HF + 2HF_2^- \longrightarrow SiF_6^{2-} + 2H_2O \tag{1.5}$$

The etch rate is mainly determined by two parameters. The primary fluoride species present at the Si surface and its concentration [44]. The former is controlled by the pH value [88] which we control via the concentration of sulfuric acid and the latter depends on the concentration of NH_4F in the electrolyte. According to [22] in our electrolyte the etching is dominated by Eq.1.3. The formation of the oxide and its etching are two competing processes which lead to the oscillations. The oscillation mechanism itself, however is not understood. Our experiment combines electrochemical dissolution measurements on a silicon working electrode with spatiotemporally resolved in-situ ellipsometric measurements, which can detect relative changes of the optical pathway through the thin oxide layer. The oxide layer is formed at the surface of the working electrode [57]. The oscillatory character of the system is known since the late 1950s [96] and has since then been the subject to various investigations [22–26, 31, 32, 53, 74, 109]. The oscillatory Si system shows a multitude of dynamical phenomena reaching from simple periodic oscillations to quasiperiodic and chaotic oscillations [26, 63, 83, 85]. It displays bi- and multistabilities which even include birhythmicity [102]. With the ellipsometric set-up our group could even show that the ellipsometric signal of illuminated n-doped silicon working electrodes exhibits spatiotemporal symmetry breaking, i.e. spatiotemporal pattern formation [56]. These spatiotemporal patterns include spatial clustering, turbulence and even chimera states [56, 57, 86].

As it was found that the oscillations in the silicon system emerge from a Hopf bifurcation [58, 85] and as the CGLE can be viewed as the normal form of a reaction-diffusion system close to a Hopf bifurcation, our group did numerical experiments on a modified version of the CGLE, the MCGLE, and could reproduce the experimentally observed antiphase and subharmonic cluster states as well as turbulence and even chimera states [80, 81]. The modification accounted for a peculiar phenomenon observed in the experiments. The global variables exhibit periodic oscillations, despite the irregular spatiotemporal dynamics displayed on the working electrode. The modification of the CGLE consisted of a global coupling term and showed that global nonlinear coupling gives rise to a new route to chimera states [80, 81].

These findings substantiate that the silicon system is not only interesting as to find the origin of the oscillations but it has also proven to be a great experimental model system for the complex behaviour of spatially extended oscillatory media. Up to the beginning of this doctoral thesis project our group has reported a large variety of interesting dynamical phenomena which have been each for itself carefully investigated. What has been missing is an overview of how these dynamics are related to one another and how they are related to the external coupling parameters of our experiment. This thesis aims to, at least partly, give an answer to these questions.

In this thesis we will show that a multitude of the different dynamical phenomena found during the electrodissolution of silicon are a result of an inherent birhythmicity in the system. We will show that depending on the kind and strength of the applied external coupling, also the two oscillation mechanisms in the system may be coupled in different ways. The couplings are a linear global coupling introduced by an external resistor and in the case of n-doped silicon, a nonlinear nonlocal coupling through the motion of valence band holes, introduced by the illumination. The coupling between the two oscillation mechanisms can lead to all kinds of deviations from simple periodic homogeneous oscillations, including period doubling, motion on a 2-torus, chaotic oscillations as well as spatial antiphase clustering or the spatial coexistence of the two oscillators in a frequency locked configuration. It is to the best of our knowledge the first experimental investigation of a spatially extended experimental system displaying birhythmicity.

The thesis is structured as follows:

In chapter 2 we introduce the experimental system. We describe the electrochemical set-up followed by a description of the ellipsometric imaging set-up and the treatment of the data collected. Finally, a detailed description of the set-up and the handling of the illumination is given which is realised by an liquid crystal on silicon spatial light modulator, implemented as part of this thesis project.

Chapter 3 deals with the dynamics of p-doped silicon which is purely homogeneous. We investigate the emergence of non-periodic homogenous oscillations, which we will relate to the inherent birhythmicity in the system, more specifically the coupling of the two oscillation mechanisms to each other.

In chapter 4 we investigate the electrodissolution of n-doped silicon, where the oscillations in the global current are accompanied by spatial pattern formation. Here, we focus on the impact of birhythmicity on the pattern formation and the role of the two coupling parameters, i.e. magnitude of the external resistance of the external resistor and the illumination intensity.

In chapter 5 we summarise the results, draw conclusions and give an outlook.

2

THE EXPERIMENTAL SET-UP

This thesis investigates the electrodissolution of silicon in a fluoride containing electrolyte. We especially focus on the effect of different types of coupling on the dynamics of the current and the optical pathway through the silicon-oxide layer, which is formed at the surface of a silicon working electrode (WE) under anodic potentials. Therefore an electrochemical set-up in combination with an ellipsometric imaging set-up is employed and, for the case of measurements with n-doped Si, complimented with an illumination system. Note that the electrochemical cell and the ellipsommetric imaging set-up was implemented by Iljana Miethe [56, 57]. Small modifications of the set-up were later performed by Konrad Schönleber [85], Andreas Heinrich [41], Elmar Miterreiter [59] and Maximilian Patzauer [64]. Some of the data treatment in this thesis was done using Matlab code code written by Konrad Schönleber in combination with a matlab gui created by Carla Zensen [107]. An illumination set-up which allows for controlled spatially heterogeneous illumination by employing a spatial light modulator (SLM) was implemented in the framework of this thesis. In this chapter, the different parts of the experiment are described in detail. First we start with the electrochemical set-up, which includes the electrode preparation, the electrochemical cell and the electrolyte. We continue by an introduction of the ellipsometric imaging system followed by a description of the data recording hardware and data treatment. Finally, we explain the illumination set-up and its operation.

2.1 ELECTROCHEMICAL SET-UP

In this section we will describe the electrochemical set-up in more detail. We start with the electrical configuration followed by a description of the working electrode preparation and the custom made three electrode electrochemical cell and finally the electrolyte.

2.1.1 *Electrical Configuration*

For the measurements with p-doped WEs we mainly used a FHI-2740 potentiostat (electronic laboratory of the Fritz- Haber-Institut, Berlin, Germany) to control the voltage between working electrode WE and reference electrode (REF). Later, we switched to a Biologic SP-300 potentiostat with which mainly experiments with n-doped silicon were performed. To stabilise the oscillations, often an external electrical resistor in series with the WE needs to be introduced between potentiostat and the WE. As mentioned above, we also want to investigate the effect of different types of couplings on the dynamics of the system. The resistor introduces one of these couplings as it introduces a potential drop, which is proportional to the global current, that, in turn, results in an effective electrode potential U_{el} according to

$$U_{el} = U_{app} - R_{ext}Aj \tag{2.1}$$

where U_{app} is the applied potential, R_{ext} the external resistance, A the active WE area and j the current density. We use a variable resistor, which can be adjusted manually.

2.1.2 *Working Electrode*

As working electrodes (WE) we use (111) single crystal silicon samples with a polished surface. We use either n-doped or p-doped silicon with a resistivity of 1-10 Ωcm or 5-25Ωcm, respectively. A back contact is realised by evaporating 200 nm of aluminium onto the unpolished side. Subsequently the back contact is thermally annealed to assure an ohmic contact. For the p-doped wafer this is done by baking the wafer at 400 °C and $5 \cdot 10^{-5}$ bar. The n-doped waver is baked at 200 °C and 1 atm. Furthermore, to remove any organic residue on the active electrode surface and to ensure a well defined initial oxide layer we plasma oxidise the electrodes.

For the experiment, the working electrode is placed on a custom made polytetrafluorethylen (PTFE) sample holder which allows it to electrically contact the WE from the back with a wire and conductive silver paste. We seal the sample with red silicone rubber (Scrintex 901, Ralicks GmbH), letting an area of 15-25 mm^2 uncovered as active electrode area. After the silicone has dried, the WE is cleaned by first rinsing it with Acetone (Merck, p.a.) and subsequently immersing it first in acetone for 10 min, followed by methanol (5 min), ethanol (5 min) and finally ultra pure water (18.2 MΩcm) (5 min). All the organic cleaning solvents used are AnalaR NORMAPUR GRADE (VWR Chemicals). All glassware is cleaned by rinsing it thoroughly with ultra pure water.

2.1.3 *Cell*

An on top sketch of the custom made electrochemical cell is depicted in Fig.2.1. It is constructed as cylinder, with the WE placed in its centre, facing a sapphire window. The window allows for an illumination of the WE, which is needed in the case of n-doped silicon. The counter electrode (CE) is a circular shaped platinum (99.999%, Chempur) wire placed between the window and the working electrode. The circular

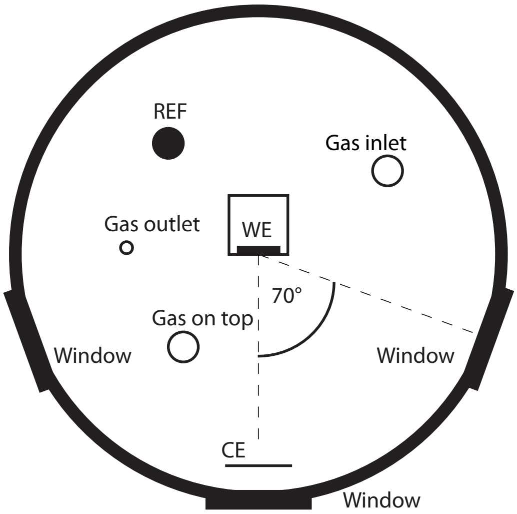

Figure 2.1: On top sketch of the cell configuration

shape of the CE ensures a homogeneous electric field at the WE and makes homogeneous illumination of the WE through the window possible. The two windows on the side are for the light beam of the ellipsometric imaging set-up. They are placed such that the light has an incident angle of roughly 70 ° onto the optical axis of the WE. The reference electrode (REF) is placed slightly behind the WE as depicted in Fig.2.1.

2.1.4 *Electrolyte*

If not stated otherwise, we use 500 ml of an aqueous electrolyte containing 142 mM sulphuric acid (H_2SO_4) and 60 mM ammonium fluoride (NH_4F). To diminish oxygen in the electrolyte and ensure reproducible initial conditions the electrolyte is purged with argon 5.0 through a glas frit. For the experiment, the gas flow through the electrolyte and the glas frit is removed and replaced by a gas inlet which keeps an argon atmosphere on top of the electrolyte to avoid diffusion of oxygen into the electrolyte. All the chemicals used for preparing the electrolyte are Suprapur grade (Merck)

2.2 ELLIPSOMETRIC IMAGING

The electrochemical measurements are combined with an ellipsometrical imaging set-up to detect inhomogeneities and changes of the optical path length through the electrolyte | silicon oxide | silicon interface at the WE surface. These changes are in part due to a changing silicon oxide layer thickness, but we also detect changes in the refractive index. However, in the framework of this thesis we are especially interested in the dynamical behaviour of the system, hence we interpret the ellipsometric signal as some representative dynamical variable rather than as specific physical property.

Fig.2.2 depicts the ellipsometric imaging set-up. As light source we use a LED (Linos, HILED, 470 nm). Its emited light first passes a collimator lens followed by a Glan Thompson Prism after which it is linearly polarised. Subsequently, it passes a $\lambda/4$-plate resulting in a elliptical polarised beam as the phase of the p-polarised gets shifted by $\Pi/2$ with respect to the s-polarised component. As the elliptically polarised light traverses the transparent SiO_2 film, the ratio of the p- and the s-polarised component changes according to the optical path length through the film. To maximise the contrast, the incident angle between the light beam and the WE was chosen to be $70\,^\circ$ which is close to the Brewster angle of water and silicon [56]. Note that the WE surface is photo sensitive and especially in the case of n-doped silicon, long exposures to the LED light without performing measurements should be avoided as it changes the WE surface and thus the initial conditions.

The LED light is reflected at the surface of the WE and consecutively passes an imaging lens. The imaging lens maps the signal onto the detector of the CCD camera (JAI CV-A50). Between the imaging lens and the detector, the light passes a Glan Thompson Prism which acts as analyser. The analyser gives an intensity signal, which is proportional to the projection of the ratio of the p- and s-polarised component of the beam onto its polarisation plane. The camera signal is digitised using a frame grabber card (PCI-1405, National Instruments).

The oscillation amplitude is sufficiently small compared the total value of the signal, such that a linear correlation between optical pathway change and signal response can be assumed during oscillations.

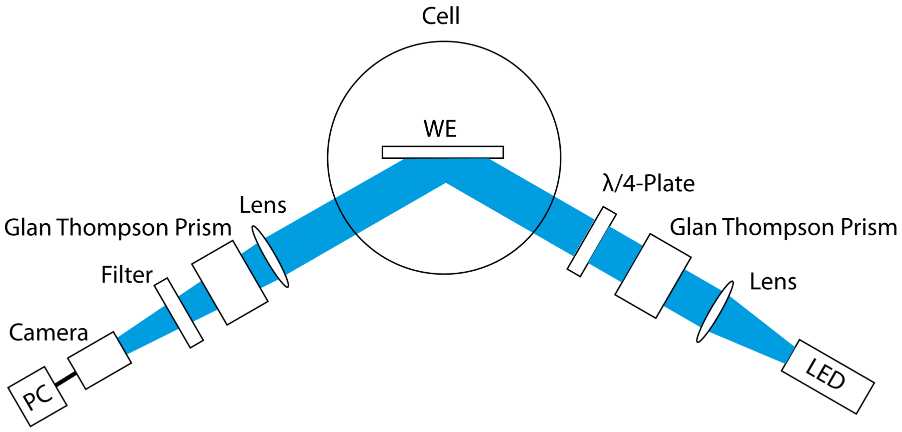

Figure 2.2: On top sketch of the ellipsometric imaging set-up

The frame rate of the CCD camera was 30 Hz. During the measurements the spatial average of the ellipsometric signal ξ was calculated from the single frames and sampled 10 times per second. The spatially resolved signal was averaged over 30 frames and saved with a rate of 1 Hz. Throughout this thesis, ξ is given as percentage of an saturation threshold up to which the the CCD responds linearly to the ellipsometric signal. The spatially resolved ellipsometric data displays spatial heterogeneities of the ellipsometric signal in arbitrary units.

2.3 DATA TREATMENT

2.3.1 *Correction and Smoothing of Ellipsometric Images*

For the spatially resolved ellipsometric data we face the problem that there are slight intensity variations across the WE, which come from the light source or might be introduced in the beam path. In addition to this, the contrast correlates positively with the absolute intensity of the system, which means that darker spots will show smaller amplitudes than brighter spots in an actual homogenous process at the WE. Therefore we corrected the data as follows:

$$\xi(\vec{x},t) = \frac{\left(\xi_{raw}(\vec{x},t) - A_m(\xi_{raw}(\vec{x},t))\right)}{\xi_{ref}(\vec{x},t_0)} \tag{2.2}$$

where $\xi(\vec{x},t)$ is the corrected signal at position $\vec{x}$ and time t and $\xi_{raw}(\vec{x},t)$ is the signal at the respective position and time. $A_m(\xi_{raw}(\vec{x},t))$ is the moving temporal average of the raw signal at $\vec{x}$ and t and $\xi_{ref}(\vec{x},t_0)$ is a reference frame which we usually took at the OCP in the beginning of the measurement day. As moving average we used a Savitzky-Golay filter with a second degree polynomial and a 1001 point window. The subtraction of the moving average results in an oscillation around zero and the division by the reference frame enhances the signal at dark spots and reduces the signal at the bright spot which results in an overall more homogeneous image.

In addition to the above correction of the spatially resolved ellipsometric images, we also applied a spatial smoothing by averaging over a region of 5x5 pixels.

2.3.2 *Data Analysis*

For some considerations it is necessary to define a local phase and local amplitude of the ellipsometric signal. Therefore, we took the analytical signal $\mathcal{Q}(\vec{x},t)$ of the local ellipsometric signal $\xi(\vec{x},t)$, which is defined as follows

$$\mathcal{Q}(\vec{x},t) = \xi(\vec{x},t) - i\mathcal{H}(\xi(\vec{x},t)) \tag{2.3}$$

where $\mathcal{H}(\xi(\vec{x},t))$ is the Hilbert transform of $\xi(\vec{x},t)$. Now the phase $\Phi(\vec{x},t)$ is defined as the angle between the positive real axis and $\mathcal{Q}(\vec{x},t)$ and the amplitude $A(\vec{x},t)$ is the absolute value of the analytical signal

[33, 70]. If necessary, we smoothed the signal in time direction by applying a Savitzky-Golay filter with a second degree polynomial and a 15 point window.

2.4 ILLUMINATION

Valence band holes act as main charge carrier in the oxidation steps. In particular, the first oxidation step has to involve the capture of a valence band hole (as opposed to the injection of an electron into the conduction band). Consequently, in the case of n-doped Si the WE must be adequately illuminated to generate enough holes for the oxidation steps. As light source we use a helium-neon laser (HeNe Laser 632.8 nm, 15 mW, Polarized, Thorlabs). Originally, the illumination was set up such that it was approximately homogeneous over the WE surface and its intensity could be controlled by a linear polariser according to Malu's law [64]. Part of this Thesis was to implement an illumination set-up which allows for finely resolved spatially heterogeneous illumination patterns. This is realised with a liquid crystal on silicon spatial light modulator (LCOS-SLM) (LCOS-SLM X10468-06, 792 600 pixels, Hamamatsu Photonics). The experimental details of the implementation of the SLM as well as the optical set-up will be discussed in the following.

2.4.1 *Illumination Set-up*

The illumination set-up is depicted in Fig.2.3. As light source we use a helium-neon laser (HeNe Laser 632.8 nm, 15 mW, Polarized, Thorlabs). The beam first passes a gray filter, which is used for a coarse adjustment of the intensity range, followed by a Glan-Thompson prism to assure the alignment between the polarisation of the laser light and the orientation of the liquid crystals in the SLM. Subsequently the beam is expanded by a factor of ten such that it covers the whole active SLM area. If the SLM is operated in the hologram mode, a lens is needed to map the image onto the image plane. In this case we use the combination of a Fresnel lens, digitally loaded onto the SLM and two physical lenses as depicted in Fig.2.3 to separate the focal point of the light reflected at the inactive part of the SLM from the one reflected at the active part. By placing a pin directly into the focal point of the first physical lens, the light from the inactive part of the SLM, the so-called zeroth order beam, can be filtered out of the beam path [108]. In that way only the part of the beam which is actively controlled by the SLM passes the lens system and a clear image is mapped onto the WE. The size of the image as well as the position of the image plane depends on the one hand on the focal lengths of the two physical lenses as well as the focal length of the virtual Fresnel lens loaded onto the SLM. On the other hand it depends on the distances between the lenses and can be calculated using optical transfer matrices as follows:

$$D_3 L_3 D_2 L_2 D_1 L_1 \begin{pmatrix} x_1 \\ \theta_1 \end{pmatrix} = \begin{pmatrix} x_{im} \\ \theta_{im} \end{pmatrix} \tag{2.4}$$

$$D_i = \begin{pmatrix} 1 & d_i \\ 0 & 1 \end{pmatrix} \quad \text{and} \quad L_i = \begin{pmatrix} 1 & 0 \\ -1/f_i & 1 \end{pmatrix} \tag{2.5}$$

with the optical transfer matrix of space D_i which relates to a distance d_i between two optical elements and the transfer matrix L_i which corresponds to a thin lens with a focal length of f_i [37]. x_1 is the initial distance between the optical axis of the lens and the ray upon entering the first lens and θ_1 is the initial angle between the ray and the optical axis. x_{im} is the distance between the ray and the centre in the image plane and θ_{im} is the angle between the ray and the optical axis in the image plane. Note that this set-up can be arbitrarily extended by optical elements. However, for each new element which is added at the end of the beam path, the respective optical transfer matrix needs to be multiplied from the left to Eq.2.4. Note also, for the calculation, the focal length f_1 of the first lens, i.e. the Fresnel lens loaded onto the SLM is multiplied by -1 as the beam is reflected at the SLM. In addition the incident angle θ_1 was assumed to be zero. This is justified as we only searched for the rough values of f_1, d_1, d_2 and d_3 which satisfied some experimental boundaries. The fine adjustment of these parameters was then done experimentally.

Between the last lens and the WE, a 7:3 beam splitter cube is placed, such that 30% of the illumination is send to another 7:3 beam splitter cube which deflects the weaker part of the beam onto a CMOS (DCC3260M, Thorlabs) camera and the stronger one onto a power meter (PM16-120, 400-1100 nm, Thorlabs). Note that the optical path lengths between the lens and CMOS and the lens and the power meter is the same as the one between lens and WE, including the cell windows and the electrolyte. We use the power meter and the camera to characterise the illumination pattern and intensity on the electrode. Experimentally we found that the intensity which reaches the WE is 3.21 times as high as the intensity which reaches the measurement diode [60].

2.4.2 *Spatial Light Modulator*

To investigate the influence of the charge carrier concentration on the dynamics during the electrodissolution of n-doped Si, it proved helpful to be able to control the intensity and shape of the illumination. This

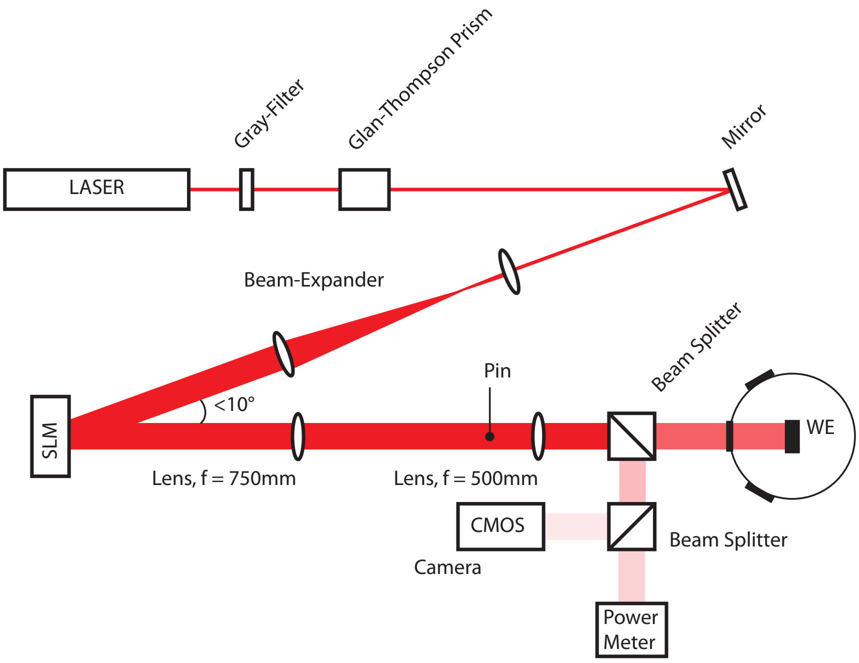

Figure 2.3: On top sketch of the illumination set-up

is realised with a LCOS-SLM. As the name implies the device consists of a two-dimensional array of liquid crystal cells on a reflective silicon substrate. The anisotropic optical properties of the liquid crystals can be exploited by changing their orientation upon a change of the electric field in the cells. A change of the orientation of the crystals introduces a shift in the phase of a coherent light beam passing the crystal layer. The SLM used in this thesis allows for a pixel wise shift of the phase between 0 and 2π with an 8-bit resolution.

The SLM comes with a software that has a build in iterative fourier transform algorithm (IFTA) [1] which creates holograms of any grey scale input image. This hologram is loaded onto the SLM such that, as the phase of the coherent light beam is shifted upon reflection, the original input image is created at an infinite distance from the SLM. An imaging lens introduced behind the SLM maps the original image onto the image plane of the lens.

There are some important points that need to be paid attention to when operating the SLM. One is that the SLM does not really control the illumination intensity but rather the contrast between different pixels. If we increase the intensity at a certain position, the intensity elsewhere is decreased. The overall illumination intensity in the image plane stays approximately constant for different input images. As the image size in our setup is much larger than the WE, we create a certain illumination pattern with a well defined local illumination intensity by creating the desired contrast pattern on the WE area and ′dumping′ excess intensity on pixels at the edge of the image, which will not contribute to the WE illumination. If we increase the illumination intensity on the WE, the illumination in the ′dump′ area becomes darker. If we just want to adjust the intensity of an homogeneous area, the size of the dump area will control the intensity resolution of the grey values in the illuminated area. If we want to locally increase the illumination intensity on the WE but hold the remaining WE illuminated constant at the initial value, we need an area of the same size as the one changed on the WE which is in turn darkened in the ′dump′ area at the edge of the illumination intensity.

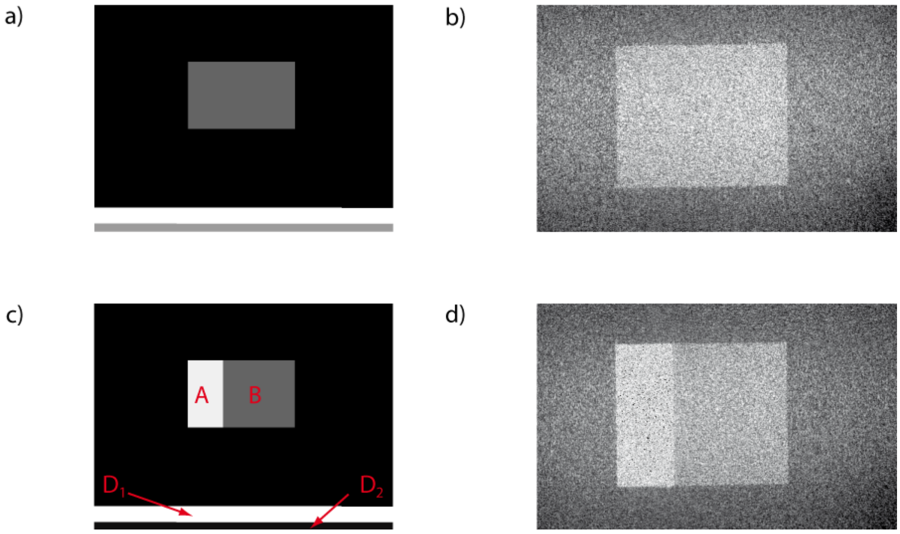

Figure 2.4: Examples of input images and their respective output images. a) is the input image for an homogeneously illuminated WE and b) is the output of a) measured by the CMOS and plotted with a logarithmic intensity scale. c) is the input image for an heterogeneously illuminated WE, where the region marked as B is equally illuminated as the one in a) and A is higher illuminated. D_1 and D_2 mark two regions in the dump area. d) depicts the output image of c), plotted with a logarithmic intensity scale. Note that the output images are too large for the CMOS to capture the WE illumination and the dump area together.

Fig.2.4 depicts the desired input image and the output image recorded with the CMOS of two images created for a measurement series in which the intensity of 1/3 of the illuminated area is increased while the remaining 2/3 of the illuminated area are kept constant. Fig.2.4 a) and b) belong to an image which illuminates the WE homogeneously. Fig.2.4 a) is the desired input image which was created as 8bit grey scale bitmap image. One can see the grey area in the middle, which is intended to illuminate the WE. At the lower edge one can see a bright bar which serves as the dump area. Usually, for the intensity control of a homogeneously illuminated area one does not need to split the ′dump′ area, however in this case, as we want to create heterogeneous patterns in the measurement series we need the additional degree of freedom. In Fig.2.4 b) one can see the output image recorded by the CMOS in the image plane of the lens system. Note that we applied a logarithmic scaling to the grey values of the image to enhance the contrast between dark areas. Note that the output image is larger than the CMOS detector and thus the bright lower edge of the input imager is cut off.

In Fig.2.4 c) and d) we see the input image and the resulting output image, of an illumination pattern where the rightmost 1/3 of the illuminated area is brighter than the remaining part. In Fig.2.4 d) we can see that the bottom of the 'dump' area is much darker than in a). For a better understanding of the intensity control we mark the 1/3 of the illuminated region where the intensity is increased as A, the 2/3 which are kept at a constant intensity as B and the two parts of the 'dump' area as D_1 and D_2. For the areas F of the different regions the following holds:

$$F_B = F_{D_1} \tag{2.6}$$

$$F_A = F_{D_2} \tag{2.7}$$

While the grey values G of the regions A and B can be chosen freely, the respective grey values in the 'dump' have to be set as follows:

$$G_{D_1} = 255 \tag{2.8}$$

$$G_{D_2} = 255 - G_A \tag{2.9}$$

To keep the remaining 2/3 constant we set the grey value in D_2 to G_{D_2} by subtracting G_A from 255. This works with any shape as long as the respective areas are of the same size. For a coarse adjustment of the range of the intensity we use grey filters between the laser and the Glan-Thompson prism as depicted in Fig.2.3.

We chose the active WE area such that its illumination fits completely onto the active detector area of the power meter, and, correspondingly calculate the illumination density on the WE i_{ill}^{WE} is given by:

$$i_{ill}^{WE} = 3.21 \cdot \frac{I_{ill}^{Diode}}{F_{ill}}, \tag{2.10}$$

where I_{ill}^{Diode} is the overall intensity measured by the diode and F_{ill} is the area of the illuminated rectangle in the image plane of the illumination set-up. The factor 3.21 was determined experimentally and translates the intensity measured on the diode to the intensity on the WE. F_{ill} is measured with the CMOS as we know the area of each pixel is $34.3 \mu m^2$. We use the built-in ruler function in the Thorlabs software of the CMOS to measure the number of pixels along the length and the height of the illuminated area and multiply this with the pixel area.

In the case of a heterogeneous illumination like the one depicted in Fig.2.4 d) the intensity of the differently illuminated parts is determined as follows. As a reference for the illumination density we take a homogeneous illumination pattern. We can measure the overall intensity of the illuminated area with the measurement diode and we know its area. We also know that the brighter part is 1/3 of the illuminated area and we assured that the illumination density in B stays approximately constant. Hence the illumination density in the bright part on the WE $i^{WE}_{A_{het}}$ is:

$$i^{WE}_{A_{het}} = 3.21 \cdot (I^{Diode}_{het} - \frac{2}{3} \cdot I^{Diode}_{hom}) \cdot \frac{3}{F_{ill}}, \tag{2.11}$$

where I^{Diode}_{het} is the overall intensity of the heterogeneous image on the measurement diode and I^{Diode}_{hom} is the overall intensity of the homogenous image on the measurement diode. Note that the shape and active areas of the WE vary each measurement day. Hence also the illuminated area needs to be adjusted for each new WE and thus the illumination intensities for given grey values also vary each day. This means that the actual output intensity of an input image has to be measured again for each measurement day. Hence suitable input images should be created and chosen after the experiment is set-up and before the measurement series begins. Note that the WE is photosensitive. Exposure to illumination without an applied voltage should be avoided as it changes the surface and thus the initial conditions. In the case of n-doped silicon no voltage should be applied without sufficient illumination intensity on the WE as this also changes the surface and thus the initial conditions.

3

THE OSCILLATORY ELECTRODISSOLUTION OF P-DOPED SILICON

In this chapter we give an overview over the dynamical behaviour during the oscillatory electrodissolution of p-doped silicon. Self-sustained oscillations during the electrodissolution of silicon in fluoride containing electrolytes were first reported by Turner in the 1950ies [96]. Since then, they have been object of intensive research [23, 26, 31, 32, 53, 75, 109]. In our group we investigate the oscillatory behaviour from a nonlinear dynamics point of view. This means we investigate the long time behaviour of the dynamics and its dependence on certain parameters. Following this ansatz, many very interesting dynamical phenomena have been discovered. In [84] Schönleber identified two different types of oscillations which can be found in the system, which he coined low amplitude oscillations (LAOs) and high amplitude oscillations (HAOs). However, in contrary to what will be discussed later, he conjectured the HAOs to evolve from the LAOs and share the same underlying feedback mechanism. In addition to the LAOs and the HAOs a multitude of more complex and non-periodic oscillations have been reported [63, 83, 94].

One of the most surprising findings with this set-up, however, was the possibility of pattern formation during the oscillatory electrodissolution of an illuminated n-doped silicon electrode [57, 58]. Although the dynamical behaviour of p-doped silicon is in many ways found to be quite similar to the n-doped case, Miethe et al. showed that for p-doped silicon the current oscillations are accompanied by spatially homogeneous oscillations of the ellipsometric signal [58].

The overall aim of this study is to investigate the influence of coupling on the dynamics of the system, especially in relation to the conjectured birhythmicity in the system. Hence, we will in this chapter, lay special focus on the resistance of the external resistor, as it controls the magnitude of a linear global coupling and, as we will discuss later, seems to have an additional effect on the reaction. The case of p-doped Si WEs give us the opportunity to investigate the influence of the coupling induced by the external resistor separately from the nonlinear nonlocal coupling involved in the n-doped case, which will be discussed in the next chapter. Hence, it is possible to identify which dynamical features can emerge from the influence of the external resistor alone. This led to our decision to focus first on the dynamics during the electrodissolution of p-doped silicon, which will be presented in this chapter.

First, to introduce the system, the already known state of knowledge is revisited, followed by a detailed characterisation of the different dynamic regimes and bifurcations between them. Finally, the new findings are discussed and brought into context with the previous knowledge in the last part of this chapter.

The results presented in this chapter have partly been published in [95].

3.1 REVISITING THE SYSTEM

In this section a brief introduction to the p-doped silicon system is given to equip the reader with sufficient insights for the results part. Therefore we first introduce the steady state behaviour without any external resistor, followed by a short introduction of the oscillations.

3.1.1 *The Steady State without Coupling*

Often the first approach in electrochemistry, when studying a new system, is to look at a cylcic voltammogram (CV), where the applied voltage is swept between two points at a constant scan rate while the current response is measured. This provides some information on which processes and effects are most prominent for certain applied voltages. For a sufficiently slow scan rate the CV can be assumed to approximately map the system steady state [64]. This is roughly the case for the CV depicted in Fig.3.1, where the applied voltage was scanned between 0.00 V vs. SHE and 8.65 V vs. SHE with a scan rate of 2 mV/s.

Following the graph from 0 V vs. SHE towards higher voltages, the current increases quite fast in the beginning, until it reaches a local maximum at roughly 0.6 V vs. SHE. After this comparable small peak in the CV, the current rises again for increasing voltage, until it reaches its maximum of roughly 0.65 mA/cm^2 at a voltage of approximately 2 V vs. SHE. After that the current settles on a plateau at roughly 3 V vs. SHE. The current on this plateau remains approximately constant up to potentials of about 7 V vs SHE from where it grows with the potential.

The small first peak is associated with the formation of pores [36, 50], whereas the voltage region after it and to the left side of the large peak is referred to as the electropolishing region [18, 29]. In this region the formation of SiO_2 is slower than its chemical etching, hence no passivating oxide layer can form and the current increases with the applied voltage. As the current reaches its maximum an oxide layer has formed which passivates the electrode and hence limits the current. As the oxide thickness increases with potential the current is further decreased until it reaches the plateau where the current density is solely determined by the chemical etch rate of SiO_2 and thus

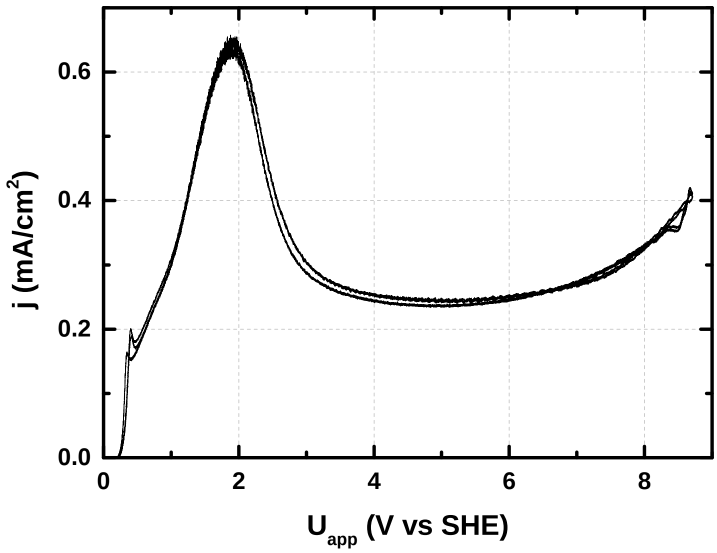

Figure 3.1: Cyclic voltammogramm of p-doped silicon with a scan rate of 2 mV/s

voltage independent. The voltage region where the current decreases with increasing potential is henceforth referred to as the negative differential resistance (NDR) branch. Note that systems with NDR are notorious for showing interesting dynamical features like bistability and oscillations [46].
As the current increases again for applied voltages higher than 7 V vs. SHE, it is believed that morphologic changes in the oxide lead to a decreased passivating effect for such high voltages [65, 83, 109].

3.1.2 *Oscillations and Bistability*

The onset of the above described current plateau is also the onset of the oscillatory behaviour, manifesting itself either in an oscillatory transient to the steady state, which thus turned into a focus, or in sustained oscillations [65]. In 2012 Schönleber et al. were the first to suggest that the system exhibits two different types of oscillations and coined them low amplitude oscillations (LAOs) and high amplitude oscillations (HAOs) [84]. Inserting an external resistor into the external circuit, the stable focus is destabilised at a critical resistance in a Hopf bifurcation, resulting in stable LAOs [26, 85]. Note that in a certain voltage region sustained oscillations have also been found without an external resistor [65]. Fig.3.2 depicts one exemplary time series of each oscillation type, where Fig.3.2a) shows the LAOs, a rather sinusoidal type of oscillations and Fig.3.2b) the HAOs which seem to have a more relaxational character and in addition a much higher amplitude than the LAOs. In this chapter we will point out that we belief that they

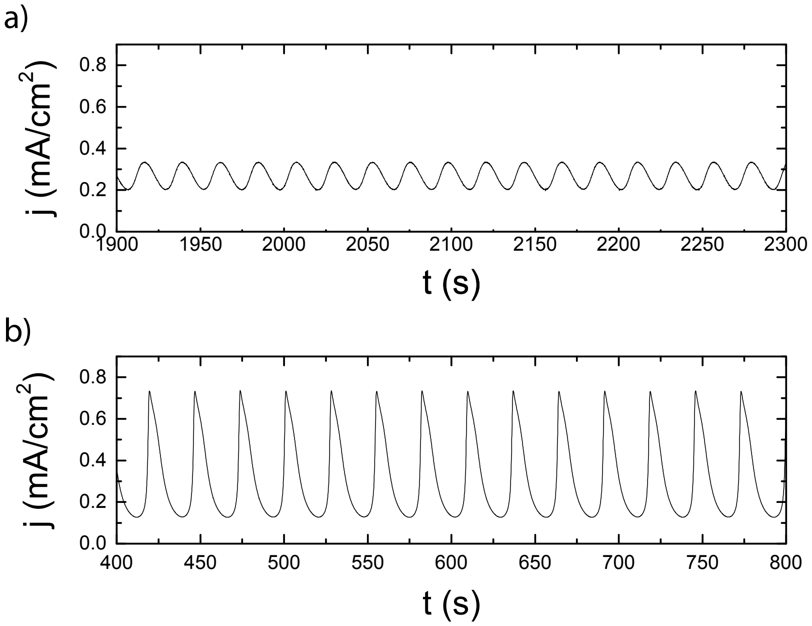

Figure 3.2: Time series of current density oscillations with $R_{ext}A$=6 kΩcm^2 measured under potentiostatic conditions. a) LAOs at 4.98 V vs. SHE and b) HAOs at 6.85 V vs. SHE. Figure taken from [95]

arise from two different limit cycles leading to inherent birhythmicity. In this thesis we will show how this inherent birhythmicity influences and characterises the oscillatory behaviour of the system.

Whether the system attains one of the two limit cycles or attains a steady state strongly depends on the initial conditions, for a certain set of parameters. Patzauer was the first to report a bistability between the node on the electropolishing branch and oscillations that had so far not been found at those parameters [63]. This bistability was further characterised in [94] and is best understood when revisiting which effect an external resistor in series with the WE has on the system. As described in Chapter 2, an external resistance R_{ext} between the potentiostat and the WE introduces a linear global coupling which reduces the effective potential drop U_{el} at the WE|electrolyte interface for any increase in current according to 2.1. Or, in other words, it introduces a linear load line into the CV, with a negative slope proportional to the resistance of the external resistor. The intersections of this load line with the system steady state in the absence of the resistor are the system solutions and the load line's intersection with the abscissa gives the parameter, i.e. the applied voltage U_{app}, corresponding to these solutions. To visualise what this means Fig.3.3 depicts a CV with an applied external resistance of 6 kΩcm^2. The forward scan is coloured black and the backward scan red. Superimposed in grey is the CV from Fig.3.1 on which a virtual linear load of 6 kΩcm^2 is added according to 2.1.

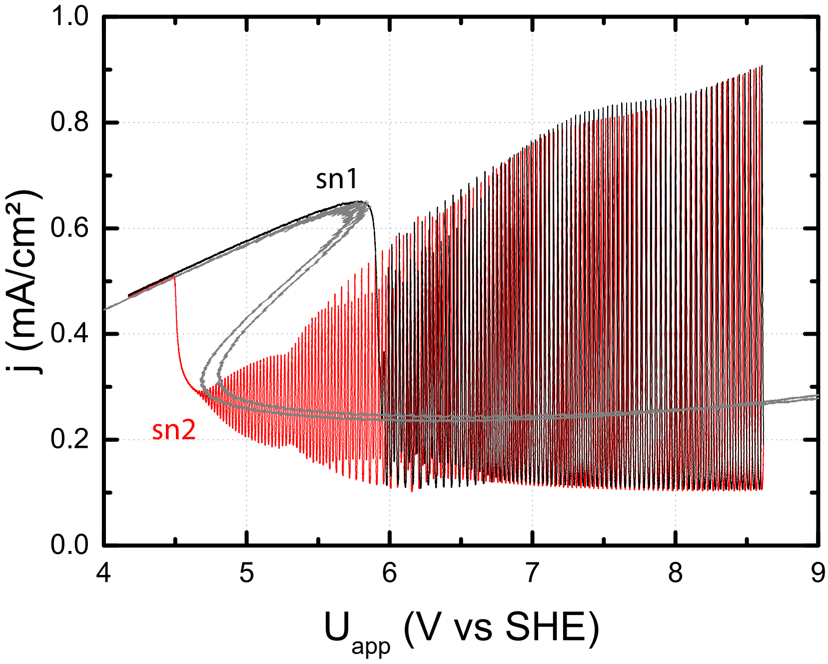

Figure 3.3: Cyclic voltammogramm of p-doped silicon with a scan rate of 1 mV/s and an external resistor of 6kΩcm^2 . Black is the forward scan, red is the backward scan. Superimposed in grey, a CV (2 mV/s) measured without external resistor, with an added virtual linear load of 6kΩcm^2.

Following the black curve from low to high potentials it first rises almost linearly, until a critical potential marked as sn1 is reached where the current suddenly drops down and the system exhibits oscillations. The amplitude of the oscillations increases with increasing applied potential.

On the way back to lower voltages the red curve follows basically the same behaviour as in the forward scan, except that at the sn1 point it stays in the oscillatory regime until the sn2 point where it suddenly leaves the oscillatory branch and abruptly moves to the non oscillatory branch where the scan started from.

Note that on the forward scan the current follows the superimposed grey curve exactly until the sn1 point which also coincides with the turning point of the superimposed curve. At the sn1 point the grey curve turns and heads towards smaller voltages and currents, until it reaches a second turning point which coincides with the sn2 point. On the lower branch of the grey curve towards higher voltages the current of the CV under load oscillates around the CV under virtual load.

Note that opposed to the subtraction of the linear load from the applied voltage of a measurement with applied external resistance, which yields the effective potential drop U_{el} at the WE, the addition of a virtual load to the curve does not have any physical meaning. However, it visualises nicely how the fixed points change their position with respect to U_{app} as an external resistor is inserted. The solution of the system, i.e. the current response, is shifted towards higher applied voltages. This effect increases with the current such that the system is effectively tilted in a way that the electropolishing branch shifts above the NDR branch, rendering the latter unstable. Hence the grey curve represents fixed points of the system and also visualises the unstable NDR branch between the sn1 and sn2 points. With this in mind it becomes apparent that the sn1 and sn2 points mark saddle node bifurcations. Note that the focus on the plateau is destabilised and a limit cycle is created by the applied external resistor. In the potential range where autonomous oscillations exist also without external resistor, an external resistor increases the oscillation amplitude drastically. Hence the scan does not follow the plateau of the superimposed grey curve, but oscillates around it.

In addition to the LAOs and the HAOs a multitude of more complex and non-periodic oscillations have been reported [63, 83, 94]. In [94] a bistability between a possible Ruelle-Takens-Newhouse scenario and a period doubling cascade has been conjectured.

3.1.3 *Linear Global Coupling in Reaction Diffusion Systems*

The external resistor introduces a linear global coupling and acts on the effective potential drop across the WE | electrolyte interface according to Eq.2.1. Hence, the governing equation for a reaction diffusion system with a linear global coupling can be expressed by the following equation.

$$\begin{aligned} \frac{\partial \vec{u}}{\partial t} &= f(\vec{u},\vec{v}) + \epsilon_1 \vec{\nabla}^2 \vec{u} + \kappa(R_{ext})(\langle \vec{u} \rangle - \vec{u}) \\ \frac{\partial \vec{v}}{\partial t} &= g(\vec{u},\vec{v}) + \epsilon_2 \vec{\nabla}^2 \vec{v} \end{aligned} \tag{3.1}$$

with the variables $\vec{u}$ and $\vec{v}$, the diffusion constants ϵ_1 and ϵ_2, the coupling constant κ, the reaction functions f and g and the spatial average of $\vec{u}$, $\langle \vec{u} \rangle$. Both equations contain a reaction term and a diffusion term, and the first equation has an additional term for the global linear coupling. When looking at Eq.3.1 it becomes clear that, for the homogenous case, the spatial derivatives as well as the coupling term becomes zero and only the reaction terms remain. We know that the external resistance introduces a global linear coupling but also has an important effect on the dynamics of the electrodissolution on p-doped silicon, which is homogeneous. Thus we can conclude, that at least one of the reaction terms also depends on the external resistance R_{ext}. Hence, in the p-doped case the governing equations probably rather look like

$$\begin{aligned} \frac{\partial \vec{u}}{\partial t} &= f(\vec{u}, \vec{v}, R_{ext}) \\ \frac{\partial \vec{v}}{\partial t} &= g(\vec{u}, \vec{v}) \end{aligned} \tag{3.2}$$

Note that Eq.3.1 and Eq.3.2 are just generalised examples of reaction diffusion systems, shown to demonstrate the difference between homogenous and heterogeneous cases and to point out that R_{ext} affects both, the homogenous dynamics and the strength of the global coupling. The equations are not an expression for the dynamics of the silicon system, as they lack at least one essential variable, which will be discussed later in this chapter.

3.2 THE U-R PARAMETERPLANE OF P-DOPED SILICON

The following section aims to provide the aforementioned big picture by adding up the results and findings gained in the scope of this thesis with the previously existing knowledge. As already mentioned, no illumination is necessary to drive the oxidation reaction in the case of p-doped silicon. In the following measurements we always used the same electrolyte which was always equally stirred, we had no temperature control and tried to keep the active WE area constant. This leaves us with the external resistance and the applied voltage as our only bifurcation parameters. Fig.3.4 depicts which types of dynamics are found for which sets of parameters in the U_{app}-$R_{ext}A$-parameter plane.

The figure shows a coloured area which marks the region where stable oscillations can be found. This region is, almost completely, encircled by a dashed orange line which represents a Hopf bifurcation. If we start looking at low applied voltages we see that the region of stable oscillations starts in a relatively narrow interval at roughly 4 V vs. SHE, between 1 kΩcm^2 and 2 kΩcm^2, and widens in $R_{ext}A$ direction with increasing applied voltage until it reaches roughly 19 kΩcm^2 for the highest applied potentials of around 8.65 V vs. SHE.

On the left side, i.e. the low resistance side, the onset of the oscillations changes towards smaller external resistances when increasing the potential from the lower boundary until it reaches 0 kΩcm^2 at 4.65 V vs. SHE. It stays at 0 kΩcm^2 until 6 V vs. SHE. The voltage range of zero external resistance oscillations is obviously also the region where no Hopf bifurcation is observed on the low resistance side. Above this potential range, the critical R_{ext} needed to find stable oscillations increases slightly with the potential, until it reaches 1 kΩcm^2 for the highest investigated voltages.

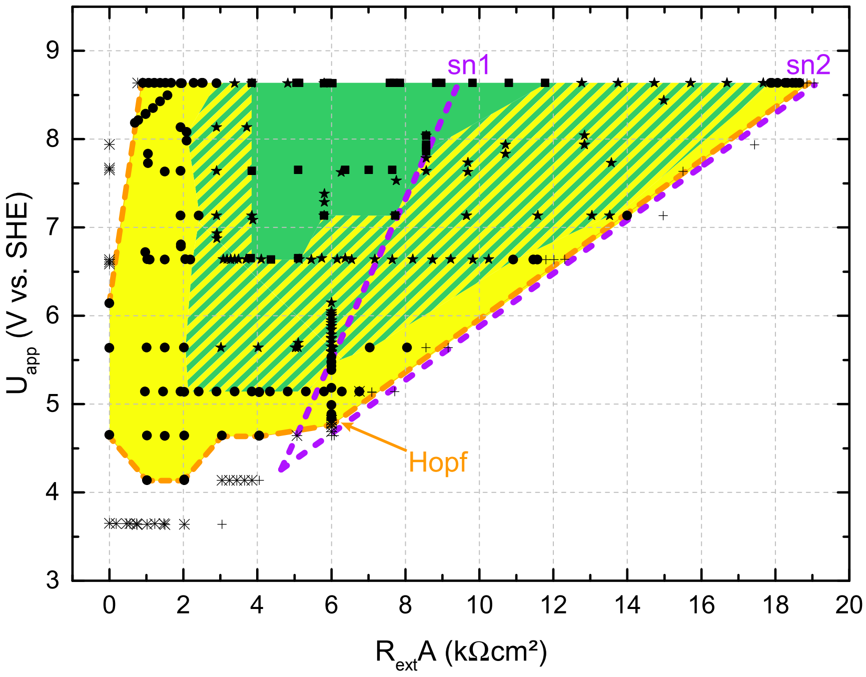

Figure 3.4: Investigated U_{app}-$R_{ext}A$ parameter plane. Orange dashed curve is the Hopf bifurcation, purple dashed are saddle node bifurcations. Green area marks HAOs region, yellow area marks LAOs region and the yellow and green striped area is where multiperiodic and aperiodic oscillations arise. The different dynamics are marked with: (+) stable nodes, (∗) stable foci, (•) LAOs, ■ HAOs and (★) multiperiodic and aperiodic oscillations. Figure taken from [95]

The coloured area is divided into three different parts. The outer part in yellow marks the region where LAOs are found and the inner green part is where HAOs are found. The low external resistance border of the green area is independent of U_{app} at a constant value of $R_{ext}A$, whereas the $R_{ext}A$ values at the right border of the green region increase with U_{app}. Between the yellow and green areas is a region which is green and yellow striped. In the striped region one finds exclusively more complex and non-periodic oscillations.

The measurement points mark the dynamical features measured at the respective parameters. LAOs are marked as discs, HAOs are marked as squares and oscillations which are not simple periodic are marked as stars. Stable nodes are marked as asterisks and stable foci as plusses. Note that for some parameters in the green area it is also possible to find non simple-periodic oscillations besides the HAOs.

There is a dashed purple line which marks the saddle node bifurcation sn2 from Fig.3.3 on the high $R_{ext}A$ side of the oscillations, for slightly higher $R_{ext}A$ values than at the Hopf bifurcation. In addition, there is a second dashed purple line marking the saddle node bifurcation sn1 from Fig.3.3. These two saddle node bifurcations seem to start, at the same parameters for lower potentials. The sn1, has a steeper slope and therefore crosses every region of the coloured area instead of passing it like the sn2 does. The area between the two saddle node bifurcation curves is the region of the bistability between the node on the electropolishing branch and the oscillatory region.

Note that it is only possible for the system to attain the oscillatory branch of this bistability if there is an initial oxide layer formed on the WE [83], e.g. if the system comes from any of the oscillatory states left of sn1 in Fig.3.4.

Overall Fig.3.4 shows that the LAOs emerge from a Hopf bifurcation and encircle the oscillatory parameter region from the low voltage side. For U_{app} larger than 6.5 V vs. SHE there is a parameter region where HAOs can be found. For the HAOs a minimal external $R_{ext}A$ value is needed which seems to be independent of U_{app}. However the maximal $R_{ext}A$ value for which HAOs can be found increases with U_{app}. The drop of the effective potential seems to induce the transition at the higher $R_{ext}A$ values, as ever higher potentials are necessary to stay in the HAOs' region for increasing $R_{ext}A$ values. The reason for the seemingly complete independence of the onset of HAOs from U_{app} at the low resistor side remains unclear. The LAOs and the HAOs region are separated by a region where merely more complex or non-periodic oscillations exist. It is noticable that these more complex oscillation types coexist with HAOs but not with LAOs.

3.3 ON THE RISE AND FALL OF THE LOW AMPLITUDE OSCILLATIONS

Previous findings characterise especially the oscillations found below $2\,\mathrm{k\Omega cm^2}$ and above 5.65 V vs. SHE as LAOs [84]. The oscillations in the yellow region between the two saddle node bifurcations in Fig.3.4 were assumed to be of a different kind [63, 83, 94]. This was because they are found for significantly different parameters as the previously known LAOs and have a much lower amplitude and a higher frequency. In the following we will explain why we belief that these oscillations are also LAOs. For both, the previously known LAOs and these oscillations, it has been shown that close to the onset of the oscillations the squared amplitude of the current is linearly dependent on the resistance indicating that they arise in a Hopf bifurcation [63, 83], with the resistance acting as bifurcation parameter.

In a measurement series indicated by the the LAOs at 5.15 V vs. SHE in Fig.3.4 we could show that the LAOs regime extends into the bistable region between the two saddle node bifurcations and that the oscillations at the high resistance border of the oscillatory region are connected with the LAOs region via the lower voltage areas of the oscillatory regime. Thus we conclude that they are both the same type of oscillations and henceforth call both LAOs. To gain more insight into the system's behaviour in the bistable region close to the sn2 saddle node bifurcation a careful parameter scan has been performed at the low voltage border of the oscillations at $6\,\mathrm{k\Omega cm^2}$. For the system to attain oscillatory states in the bistable region, it is necessary to have an initial oxide layer on the WE, therefore we started by applying a voltage of 6.90 V vs. SHE. After some periods we switched the potential to 4.90 V vs. SHE, where LAOs are expected, kept the applied potential constant until the oscillations stabilised and recorded the time series. Then we changed to a lower applied potential by sweeping it at a rate of 1 mV/s to the desired value, we waited for the system to settle, recorded the time series and proceeded. During the whole process the external resistance was kept constant at $6\,\mathrm{k\Omega cm^2}$.

Fig.3.5 a) shows a projection of those measurements into the phase plane spanned by the spatial average of the ellipsometric signal ξ and the current density j. The black lines depict attractors of the system and the red line is a transient recorded after a potential variation. The plot shows one comparably large closed cycle which was measured with an applied voltage of 4.90 V vs. SHE, a smaller limit cycle measured at 4.84 V vs. SHE and a stable focus measured at 4.82 V vs. SHE. Note that the intersections of the two limit cycles and during the transient indicate strongly, that there exists at least one more essential variable besides the ellipsometric signal ξ and the current density j.

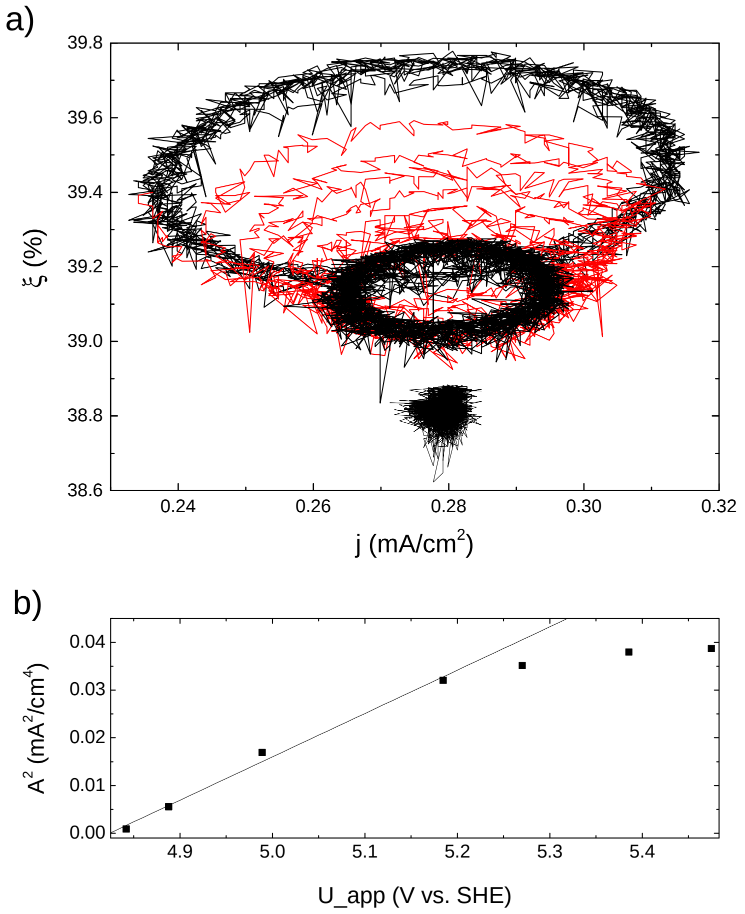

Figure 3.5: a) LAOs and stable focus in the ξ-j phase plane. The red curve marks the transient after the potential variation. The black curves are attractors. The large cycle was measured at 4.90 V vs. SHE, the small one at 4.84 V vs. SHE and the stable focus at 4.82 V vs. SHE. b) The squared amplitude A^2 of the current density LAOs plotted against the applied potential. a) and b) measured with $R_{ext}A$=6 kΩcm^2. Figure taken from [95]

In Fig.3.5 a) it can be seen that the applied voltage acts as bifurcation parameter and destabilises a focus, resulting in LAOs which grow in amplitude with the potential.
In Fig.3.5 b) the squared amplitude of the current density is plotted against the applied potential and marked as squares. The line is a linear fit through the first four measurement points. It can be seen that close to the bifurcation the squared amplitude of the oscillations grows approximately linearly with the applied potential indicating that the focus is destabilised in a supercritical Hopf bifurcation. Hence we can confirm that the LAOs are at the onset of the oscillatory region when coming from low voltages in the U-R parameter plane. They emerge from a supercritical Hopf bifurcation, for which both the applied potential and the resistor may act as bifurcation parameter and thus encircles the oscillations in the U-R parameter plane except for the range of zero external resistor oscillations. Note that the region where the stable focus exists close to the sn2 saddle node bifurcation is extremely narrow and thus experimentally difficult to reach. If the parameter variations are not performed sufficiently slow, one will push the system across both, the Hopf bifurcation and the saddle node bifurcation, such that it will attain the stationary node on the electropolishing branch.

Between the HAOs and the LAOs is a parameter region in which only non simple-periodic oscillations in a multitude of different shapes can be found. It is already speculated, that within this region there is a bistability between an attractor undergoing a possible Ruelle-Takens-Newhouse scenario, and one that traverses a period doubling cascade [94].

The Ruelle-Takens-Newhouse scenario describes a route into deterministic chaos [61, 78], where three sequential Hopf bifurcations first create a stable limit cycle then a 2-torus and finally render the dynamics chaotic by creating a 3-torus which is always unstable [3].

In the period doubling cascade, also known as Feigenbaum scenario, the system undergoes an infinite sequence of so called period doubling bifurcations, each doubling the number of periods needed to close the limit cycle [30]. The repeated doubling of the limit cycle period fills the phase space with unstable solutions until they are so close together that chaotic windows emerge.

In the following we revisit these two scenarios and investigate their emergence in more detail. We will show that the 2-torus arises due to a periodic forcing of the LAOs by the HAOs which is induced as the two oscillation mechanisms are coupled via the external resistor. We will discuss that the torus breakdown is probable not the result of a tertiary Hopf bifurcation and therefore the system does not follow the Ruelle-Takens-Newhouse scenario. It is much more likely that the 2-torus breaks down as the coupling strength between the two oscillation mechanisms exceeds a certain limit and the surface of the 2-torus loses its smoothness which results in a strange attractor [2, 7].

To elucidate the origin of the torus, we started from the LAOs at 6 kΩcm^2 and varied U_{app} towards more anodic potentials. We proceeded in the same manner as above, i.e. we scanned the potential with 1 mV/s to the desired value, waited for the transient to fade and recorded the time series and continued. The resistor was kept constant during the whole process.

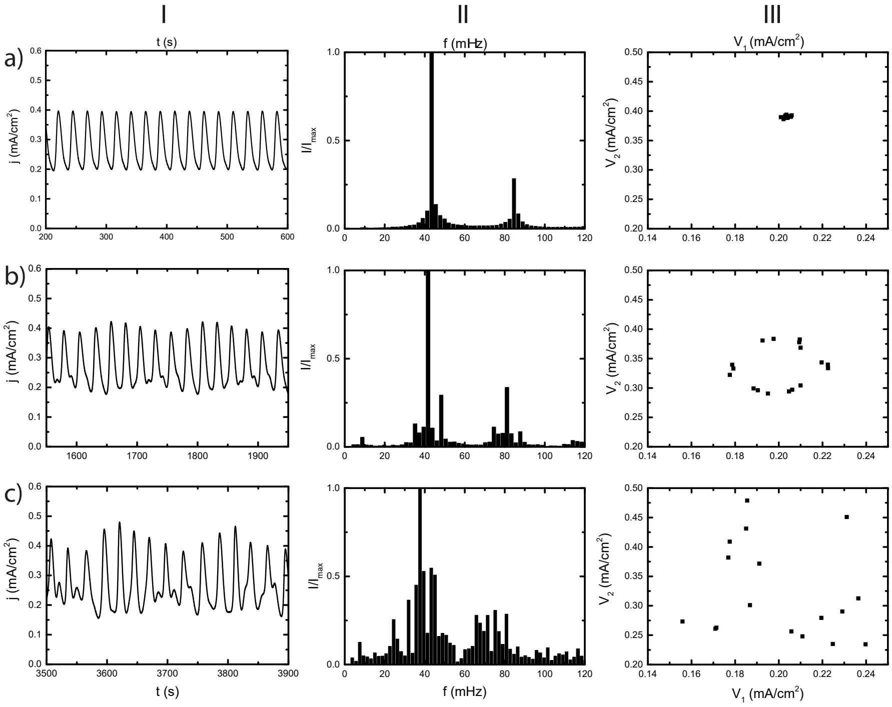

Figure 3.6: Table of time series (I), normalised frequency spectrum (II) and Poincaré section at a) 5.54 V vs. SHE, b) 5.69 V vs. SHE and c) 5.95 V vs. SHE all measured with $R_{ext}A$=6 kΩcm^2 [95]. Figure taken from [95].

Fig.3.6 a), b) and c) shows exemplary states which arise upon an increase of the potential. The first column depicts the time series, the second column the frequency spectrum, normalised to the magnitude of the main frequency and the third column the Poincaré section of the respective state. To construct the Poincaré sections we first chose a suitable current density value j_0 and measured the times t_k at which the falling branch of the current density oscillations took this value, i.e. $j(t{=}t_k){=}j_0$. Our new variables V_1 and V_2 were then defined by

$$V_1(t_k) = j(t_k - 3T/4) \text{ and } V_2(t_k) = j(t_k - T/4) \tag{3.3}$$

where T is the oscillation period corresponding to the dominant frequency of the normalised frequency spectrum. A Poincaré section maps the intersections of the dynamics in an n-dimensional space with an n-1-dimensional subspace and thereby reduces the dimensionality. This means for example that a limit cycle in a 3 dimensional

phase space mapped on a plane will be a fixed point, a 2-torus will be mapped as an invariant circle and a strange attractor will be mapped on some submanifold, often of complex shape.
Column I of Fig.3.6 a) depicts the time series of simple periodic LAOs measured at 5.54 V vs SHE and an applied external resistor of 6 kΩcm^2. Their shape is relatively sinusoidal and the amplitude is roughly 0.2 mA/cm^2 and constant. In column II the normalised frequency spectrum of the time series shows two distinct peaks with almost no background. The larger peak at roughly 45 mHz corresponds to the oscillation frequency and the second peak at roughly 90 mHz is the first harmonic of the main frequency. In the Poincaré section the dynamic is mapped on a fixed point which is expected for a stable limit cycle.

Fig.3.6 b) shows a state that was recorded after the potential was increased to 5.69 V vs. SHE. The time series in column I shows a distinct modulation of the oscillations. The minimum amplitude is still roughly 0.2 mA/cm^2 but the maximum increased slightly to roughly 0.3 mA/cm^2. In addition to the modulation of the oscillations, there are small outliers which arise on the rising and falling branch of some peaks. When looking at the normalised frequency spectrum in column II one sees that the main peak and its first harmonic shifts towards smaller frequencies compared to the one in Fig.3.6 a). In addition to the main peak and its harmonic, a number of other peaks, of which the most prominent lies close to 50 mHz, emerge in the spectrum. The position of the peak below 10 mHz is in the same order of magnitude as the frequency of the envelope, observed in the time series of Fig.3.6 b). In the Poincaré section in column III one sees that this dynamic is mapped onto a circular shaped invariant limit set.
The behaviour in the time series of Fig.3.6 b) reminds one of beat oscillations which would result from a second frequency appearing in the dynamics. In the case of beat oscillations, the frequency of the envelope usually corresponds to the difference of the two main frequencies of the system. The peak slightly below 10 mHz which seems to correspond to the frequency of the envelope together with the main frequency slightly above 40 mHz indicates strongly that the signal close to 50 mHz corresponds to a second oscillations frequency in the system causing the modulation of the oscillations. Other peaks arise at linear combinations of the two main frequencies. The conjectured second frequency seems then to be confirmed by the circular invariant limit set in the Poincaré section which corresponds to motion on a 2-torus. Fig.3.7 depicts the squared average radius $\langle r \rangle^2$ of the circular limit sets plotted against the applied potential. The good linear fit through those points indicates a linear dependence of $\langle r \rangle^2$ on the bifurcation parameter U_{app} which is the universal behaviour of limit cycles close to Hopf bifurcations. Hence we conclude that, as we increase U_{app} from 5.54 V vs. SHE to 5.69V vs. SHE with an

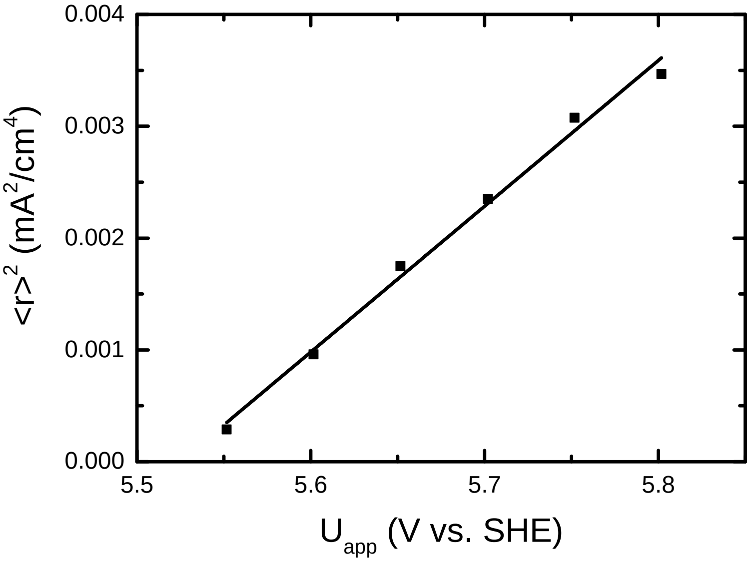

Figure 3.7: The squared average radius $\langle r\rangle^2$ of the circular shaped invariant limit sets in the Poincaré sections plotted vs. U_{app}. The line is a linear fit through the points. [95]

external resistor of 6 kΩcm^2, the system undergoes a secondary Hopf bifurcation after which it exhibits motion on a 2-torus. Note that $\langle r\rangle^2$ is calculated according to

$$\langle r\rangle^2 = \langle \|\vec{x_i} - \langle\vec{x}\rangle\|\rangle^2, \tag{3.4}$$

where the average radius $\langle r\rangle$ is the average distance of the points $\vec{x_i}$ in the Poincaré section to the average of all points $\langle\vec{x}\rangle$ of the Poincaré section.

The applied potential was then further increased to 5.95 V vs. SHE. The corresponding time series is plotted in Fig.3.6 c). The amplitude of the oscillations is larger compared to the one from Fig.3.6 b) and the outliers are more distinct and seemingly less regular. Omitting the outliers, the minimal amplitude is still roughly 2 mA/cm^2, however the maximal amplitude seem to have increased further. Overall, on first sight the behaviour resembles the one from Fig.3.6 b), i.e. modulated oscillations with slight irregularities. However on a closer look, it becomes apparent that the irregularities are more pronounced than in the time series above. Looking at the second column of 3.6 c) we see that the background of the normalised frequency spectrum is drastically increased. The main frequency is now slightly below 40 mHz which is still close to the one of the two spectra above but now the spectrum also shows a high background. This background is dense and has a continuous character which makes it almost impossible to identify single peaks. The points in the Poincaré section in the third column seem to be randomly scattered.

We thus conclude that even though the time series of 3.6 c) is reminiscent of the beat oscillations, it is different in that the irregularities are more prominent. The normalised frequency spectrum of this state is characterised by a large background, which can point towards chaotic motion. Another indication for deterministic chaos is the random cluster of points this attractor is mapped to in the Poincaré section. Note that due to the experimental character and especially the large time scale it is difficult to prove that the system exhibits deterministic chaos. However, since it is known that a torus breakdown often creates a strange attractor, together with the large background in the normalised frequency spectrum and the breakdown of the circle in the Poincaré section in 3.6 c) we conclude that the system ends up exhibiting chaotic motion.

Note that that motion on a 2-torus will often be the result of an oscillator with a certain frequency being periodically forced with another frequency. This can be realised by coupling two oscillators with different frequencies. What kind of dynamics arise from such a configuration depends on the coupling strength and the ratio of their frequencies. If the coupling strength is zero and the ratio of the two frequencies is rational, the motion would live on the surface of a torus but would be periodic. However the Lebesgue's measure of all rational frequency ratios is zero. As the coupling strength is increased also the parameter range of periodic solutions increases. Around the rational ratios of the frequencies are parameter regions for which the motion will be periodic although the ratio of the frequencies would deviate from a rational value. These regions are called Arnold tongues. The width of the Arnold tongues increases with the coupling strength, until, at a certain value of the coupling strength, the Lebesgue's measure of the solutions outside the Arnold tongue will be zero. Note that the trajectory of the non-rational solutions will fill the surface of the torus densely after an infinite period of time but will never close, hence the motion is quasiperiodic and we call the attractor a 2-torus. [7]

It can be concluded that the LAOs emerge from a Hopf bifurcation and as the potential is further increased the system undergoes a secondary Hopf bifurcation resulting in motion on a 2-torus. Later we will show that the 2-torus arises due to the LAOs being intrinsically coupled to the HAOs. Upon further increase of the applied potential, the strength of this coupling seems to increase as well. A probable scenario is then, that, as the potential is further increased, the coupling strength exceeds a certain limit. As it exceeds this limit, the 2-torus eventually breaks down and the system attains a strange attractor. Often the torus breakdown is accompanied by a loss of smoothness of its surface [2, 7].

The shift towards smaller frequencies for higher potentials is believed to be related to an increase in oxide thickness, as we also observe an increase of the temporal average of ξ. However, the connections between potential, oxide layer thickness and frequency are not well understood so far. Apart from the emergence of a secondary frequency, the quasiperiodic and chaotic oscillations seem to be strongly related to the LAOs, since at least the basic physical mechanism does not seem to change. It rather looks as if there is some impact on the LAOs which creates the modulation and as this impact grows, it creates a strange attractor. Note that as the potential is further increased, the system abruptly changes its behaviour and attains a state belonging to a period doubling cascade which will be discussed in the following section.

3.4 ON THE HIGH AMPLITUDE ROUTE TO CHAOS

After we just showed how the complex behaviour which arises from simple periodic LAOs still seems to be strongly related to the LAOs, we will now put our focus on HAOs. In this paragraph we will investigate the response of the system as we move from simple periodic HAOs, like the one depicted in Fig.3.2 b) at 6 kΩcm^2, towards lower potentials. We will show that, the system traverses a period doubling cascade as we pass through the striped region of Fig.3.4 until even a period doubled torus can be found. Period doubling cascades in the 1/2 Arnold tongue above critical values of the coupling strength and even period doubled tori have been reported in [49, 79, 98]. Note that the measurement series on the HAOs was conducted with an external resistor corresponding to a resistance of 6 kΩcm^2 and the potential variations were conducted in the same manner as for the measurement series on the LAO branch discussed above.

Fig.3.8 shows a time series of the current density measured at 6.05 V vs. SHE. The maxima alternate between high current values and lower values. The same holds for the minima. This time series is representative for the states found when entering the striped region of Fig.3.4 from the simple periodic HAOs. For this type of oscillations it is often easier to employ next-maximum maps to further elucidate the attractor. In next maximum maps the maxima of a time series are plotted against their respective preceding maxima. In this way, one can read the exact value and relative order in which the maxima appear, and thus one gets a clearer picture of the attractor than when looking at time series.

Fig.3.9 depicts the next-maximum map of a selection of states found upon the reduction of U_{app}, starting from a simple periodic HAO state, shown as the dark blue point which was measured at 6.85 V vs SHE. At 6.55 V vs. SHE marked by the two turquoise points is a period two (P2) state, at 6.35 V vs. SHE the pink points arrange on two bands, suggesting that they belong to a chaotic two band attractor (C2). Further reducing U_{app} to 6.15 V vs. SHE results in oscillations which show four points in the next-maximum map, hence a period-four (P4)

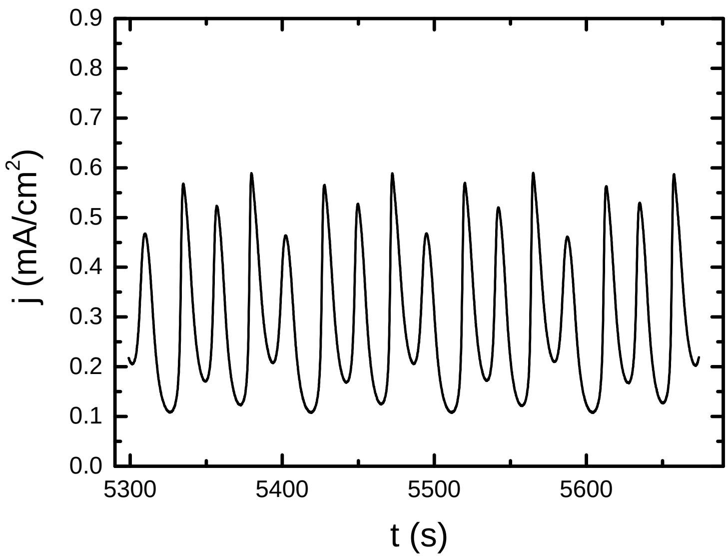

Figure 3.8: Time series of a state from the period doubling cascade measured at $U_{app} = 6.05\,V$ vs. SHE with $R_{ext}A$=6 kΩcm^2.

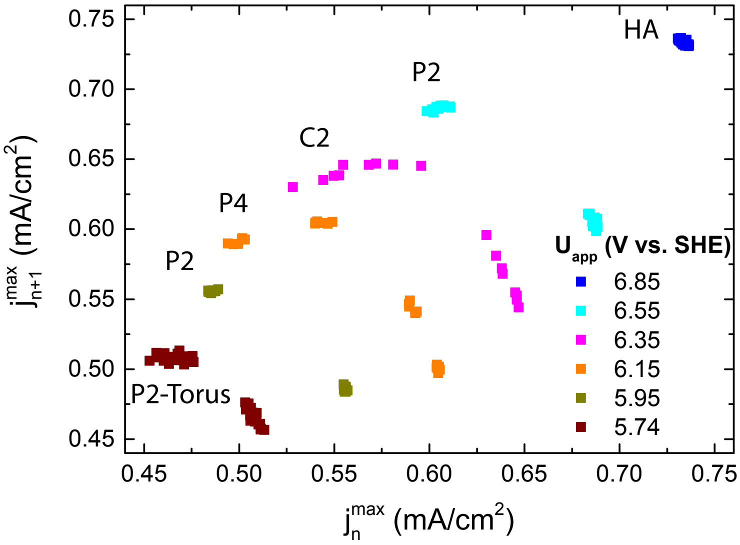

Figure 3.9: Next-maximum-maps of different states in the period doubling cascade. Simple periodic HAOs are coloured blue, the P2-state is coloured in cyan, the chaotic two-band attractor in pink, the P4-state in orange a second P2-state in olive and the P2-torus is coloured in brown. $R_{ext}A$=6kΩcm^2 [95]

state. At 5.95 V vs. SHE, there are again only two points in the next maximum map marked in olive green. At the end of this cascade, at 5.74 V vs. SHE, there is an attractor which resembles a P2 behaviour but when zooming in it shows that each of the clusters forms an invariant circular limit set and thus this state constitutes a period two torus (P2-Torus). The higher periodic solutions arise from traversing a period doubling cascade [94, 95]. Fig.3.9 shows nicely that the higher periodic and chaotic states evolve from the simple periodic HAOs.

So far we have shown that we can find two different types of oscillations, the LAOs and the HAOs, in separated regions of the U_{app}-R_{ext} parameter plane. Between these parameter regions, there is a region in which we find complex oscillations. Some of the complex oscillations can be related to LAOs and others emerge from HAOs. The fact that these complex oscillations arise where the LA and HA limit cycles approach each other in parameter space, hints towards an intrinsic coupling of the two limit cycles which results in the complex behaviour.

3.5 BICHAOTICITY, A BISTABILITY OF COMPLEX OSCILLATIONS

Above we have already identified two different oscillations types in the system, the LAOs and the HAOs, and investigated their emergence and decay. Both types of oscillations undergo different types of scenarios in which their motion changes from simple periodic to more complex and finally to chaotic motion. We claim those more complex dynamics still to be strongly related to their respective simple periodic limit cycle they emerge from, due to their similar shape and behaviour. Another interesting feature is that those two scenarios overlap in parameter space, i.e. they are bistable.

To characterize this hysteresis we conducted a finely resolved parameter scan analogously to the above described procedure, i.e. scanning from one potential value to the other with a rate of 1 mV/s, waiting for the transient to settle and then recording the time series. The external resistor was held constant at 6 kΩcm^2. We started from simple periodic LAOs at 5.40 V vs. SHE and scanned towards higher voltages. Whenever the system underwent a qualitative change in its behaviour, we changed the scan direction to measure the hysteresis. Fig.3.10 shows the average current density of the time series recorded in this process. The discs mark oscillations attributed to LAOs and the squares mark oscillations related to the HAOs. The black points are measurements on the forward scan, i.e. where we scanned from lower to higher voltages and the red points are recorded on the backward scan. The arrows also indicate the scan direction.

Starting from the simple periodic LAOs at 5.40 V vs. SHE the average current density decreases with increasing applied potential in the whole LAOs region. The slope of the decrease is relatively steep for

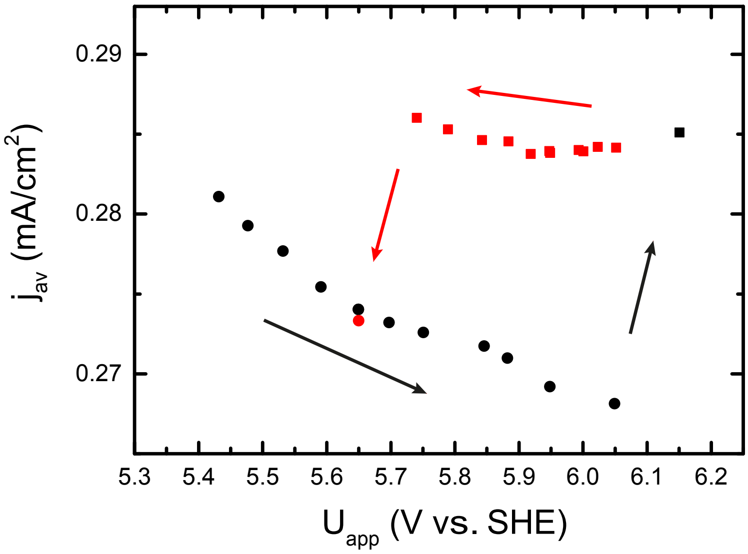

Figure 3.10: The average current density of the oscillations plotted vs U_{app}. (•) mark LAOs and (■) mark HAOs. Black points are measured after the potential was increased and red points were measured after the potential was decreased. Figure taken from [95].

smaller voltages between 5.40 V vs. SHE and rouhgly 5.65 V vs. SHE. Upon the change from 6.05 V vs. SHE to 6.15 V vs. SHE the dynamic changes drastically as the system attains a state on the HAO branch which has a higher average current density.

After the system has attained a state on the HAO branch, we start to reduce the applied potential again. The average current density does not change significantly when we do so. Rather, it seems independent from the applied voltage and is only slightly increasing with decreasing potential. Especially between 6.10 V vs. SHE and 5.90 V vs. SHE the average current density seems to be constant. When changing the applied potential from 5.74 V vs. SHE to 5.65 V vs. SHE the HAOs branch becomes unstable and the system attains an attractor on the LAO branch. This means that the potential interval, in which a bistability between the two oscillatory branches is found, lies between 6.15 V vs. SHE and 5.74 V vs. SHE for 6 kΩcm^2.

In Fig.3.10, the average current density splits up into two branches, where the branch with higher average current density can be associated with dynamics we claim to be related to HAOs and on the lower branch the system exhibits the dynamics we correlate with LAOs. This underpins further what we already claimed above, i.e. that the 2-torus and the strange attractor which the system attains after the torus breakdown are in fact closely related to the LAOs, whereas the states in the Feigenbaum scenario are closely related to the HAOs.

Note that the region of the bistability lies in the interval of complex dynamics , i.e. the striped region in Fig.3.4. Analogous to birhytmicity, in which two periodic limit cycles are stable at the same parameters, the coexistence of two strange attractors is called bichaoticity. In the presented case we have two different routes into chaos which are bistable.

But how does this bichaoticity emerge? To discuss this question we recall that we can find two different limit cycles in the dynamic of the system. Hence one could say that the system is inherently birhythmic. From all the examples of birhythmicity which have so far been found one could, in a way, distinguish between two different types of birhythmic systems. Fig.3.11 illustrates this thought by exemplary sketches of the phase portraits of the two types. Fig.3.11 a) depicts the simpler case of birhythmicity in two dimensions, i.e. the two stable limit cycles separated by an unstable one, living in the same phase plane. The red point in the centre is an unstable focus and the dashed red circle represents the unstable limit cycle. The grey arrows indicate the vector field. This type of birhythmicity can for example emerge from a saddle node bifurcation of periodic orbits. An example of a system which exhibits this case of birhythmicity in two dimensions is the septic van der Pol oscillator [103]. In general, limit cycles live in at least two dimensions, which means that they need at least two oscillatory variables. Hence two limit cycles in a 2d system share both oscillatory variables, as it is depicted in Fig.3.11 a). In 2d systems the motion cannot become chaotic, as chaos can only emerge in at least 3d systems.

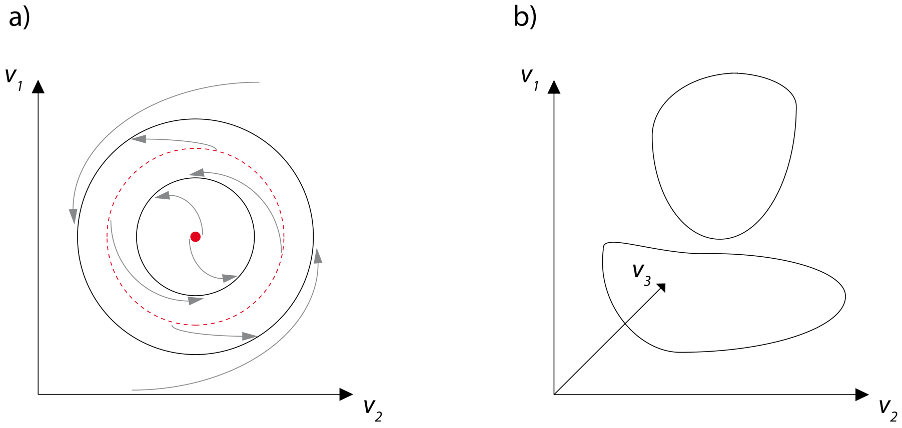

Figure 3.11: Phase portraits of two qualitatively different cases of birhythmicity. In a) two bistable limit cycles (black) separated by an unstable one (dashed red) in a 2D phase space. The red dot is an unstable focus and the arrows indicate the vector field. In b) two limit cycles arbitrarily oriented in a 3D phase space.

Fig.3.11 b) depicts the second type of birhythmicity, which needs at least three dimensions, here indicated by the three axis along the variables v_1,v_2 and v_3. The two closed curves depict two limit cycles which are oriented arbitrary in the three dimensional phase space. The arbitrary orientation in phase space accounts for the possibility that oscillations can also involve more than two oscillatory variables. Thus, in the three dimensional case, depicted in Fig.3.11 b), the two limit cycles share at least one and maximal three oscillatory variables. One example of such a system, i.e. a system where the two limit cycle do not share all oscillatory variables, are two chemical oscillators coupled via one shared species [4, 5]. Between the two limit cycles there has to be a separatrix, which is the invariant manifold that separates the basins of attraction of the two limit cycles. We suggest now, that if the parameters are varied such that the two limit cycles approach each other in phase space, they also approach the separatrix. Eventually, the limit cycles come so close to each other, such that the vector field in their vicinity is, as a consequence of the continuity condition at the separatrix, influenced by the respective other limit cycle. We suggest that this could perturb the trajectory on the limit cycles and render the motion more complex or even chaotic. In this way the motion on the observed limit cycle could be influenced by the other stable limit cycle even before the observed one becomes unstable. In nonlinear dynamic one would say that in the vicinity of the separatrix the limit cycle is influenced by the "ghost" of the other limit cycle.

Note that in such a scenario hysteretic behaviour could arise, as one limit cycle might influence the other one in a different manner than the other way around. The two different types of complex behaviour detected in our experiments, which are even bistable for some parameters, is what makes this system so unique compared to previously reported birhythmic systems. In literature the interaction between the two oscillations led to complex or compound oscillations but not to a hysteresis. In small parameter regions, periodic oscillations were reported to coexist with complex ones, but a bistability of complex oscillations was not detected [4, 5, 28, 43].

We suggest that the complex oscillations in the dynamics of our experiment, as well as the bichaotic behaviour emerge as a consequence of an intrinsic coupling of the two coexisting limit cycles, as described above. The two limit cycles in our case are the LAOs and the HAOs which are simple periodic but separated by a region of the U_{app}-R_{ext} parameter plane where only complex dynamics as well as hysteretic behaviour, i.e. bichaoticity, is found. The chaotic motion displayed by the system also shows that we have at least three essential variables, as this is a necessity for chaos to emerge. Another hint which suggests that the dynamics live in a phase space of dimension higher than two, are the intersections of the transients in the phase plane plot depicted in Fig.3.5. Hence the bichaotic behaviour emerges as a result of an intrinsic birhythmicity, i.e. the bistability of the LAOs and the HAOs limit cycle in phase space. However, the birhythmicity manifests itself as complex oscillations and bichaoticity due to an intrinsic coupling of the two limit cycles.

Unfortunately it is difficult to prove this type of intrinsic entrainment but we can in a first step check for plausibility by naively comparing the frequencies in the normalised frequency spectra of the coexisting states. Fig.3.12 shows exemplary two normalised frequency spectra of two time series, both recorded at 5.84 V vs. SHE. Fig.3.12 a) was initialised on the LAOs branch and Fig.3.12 b) on the HAOs branch. Both frequency spectra are normalised to their respective maximum. Fig.3.12 a) shows a normalised frequency spectrum of a state on the LAOs branch, which resembles the one in Fig.3.6 b). There are three frequencies highlighted with colours. The main frequency f_1 at (40.10 ± 0.69) mHz in red, the second largest frequency f_2 at (45.58 ± 0.69) mHz in green and the envelope frequency f_e at (6.91 ± 0.69) mHz in blue. The main frequency f_1 represents the maximum of the normalised frequency spectrum and thus the main frequency of the time series. As we know from the discussion of Fig.3.6 b), the small peak at frequencies below 10 mHz is the frequency of the envelope. Above we concluded that the second highest frequency f_2 is a good candidate for the second frequency of the 2-torus since the envelope frequency is usually the difference between the poloidal and the toroidal frequency, and $f_2 - f_1$ is in the same range as f_e. In the example of Fig.3.12 a) the difference $f_2 - f_1 = (5.48 \pm 1.38)$ mHz which lies within the uncertainty of f_e and makes it plausible for f_2 to actually be the second frequency.

Fig.3.12 b) depicts the normalised frequency spectrum of a P2 state on the HAO branch also measured at 5.84 V vs SHE. There are four distinct signals which consist of the main frequency f_{HA}, one frequency at exactly $0.5\,f_{HA}$, which arises due to the doubled period, and higher harmonics at $1.5\,f_{HA}$ and $2\,f_{HA}$. The background is negligible. The main frequency f_{HA} is marked in green and lies at (46.03 ± 0.80) mHz which lies within the uncertainty of f_2 from Fig.3.12 a). Also the difference between f_{HA} and the main frequency from Fig.3.12 a) f_1, i.e. f_{HA} - f_1 lies within the uncertainty of the envelope frequency f_e from Fig.3.12 a). This shows that it is definitely in the realm of possibilities that f_2 is not only the second frequency of the 2-torus but might also be strongly correlated to the main frequency f_{HA} of the coexisting P2 state from the HAO branch.

Table3.1 shows the frequencies of two more pairs of coexisting states measured at 5.95 V vs. SHE and 6.05 V vs. SHE. The frequencies are extracted from their respective normalised frequency spectra analogously to the above described states at 5.84 V vs. SHE. The frequencies of all the pairs of coexisting attractors from Table3.1 fit similarly to the hypotheses of the 2-torus arising from a perturbation of the LAOs by the respective coexisting P2 HAO attractor, as the secondary frequency of the 2-torus and the main frequency of the HAOs attractor seem to coincide for each pair. However it should be noted that the relative uncertainties of the frequencies are large, especially for f_e. Also simply comparing the frequencies of two coexisting states to see whether they have influence on each other or not is, from a non-linear dynamic point of view, a bit naive. The interaction due to perturbations in the flow field might be much more complex than just summing up the dynamics. Nevertheless the 2-torus is an attractor defined by its two independent frequencies, we have an inherent birhythmicity in the system and the frequency of the coexisting attractor, i.e. the P2 on the HAO branch, fits well to this narrative.

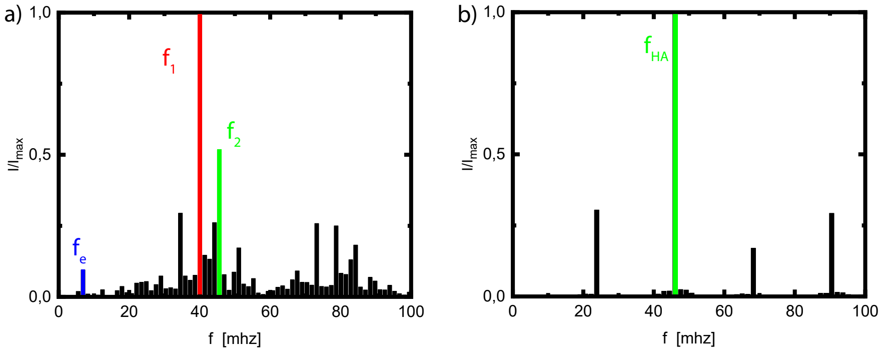

Figure 3.12: Two normalised frequency spectra of time series measured at 5.84 V vs. SHE a) initialised on the LAOs branch and b) initialised on the HAOs branch. In a) the dominant frequency f_1 is coloured red the frequency with the second largest signal f_2 green and the frequency of the envelope f_e is coloured blue. In b) the main frequency f_{HA} is coloured green.

We thus conclude that the LAOs and the HAOs influence each other via an intrinsic coupling. For the two oscillator, the intrinsic coupling results in two qualitatively different scenarios. As the LAOs are influenced by the HAOs limit cycle, a 2-torus emerges and as the strength of the influence exceeds a certain threshold the torus breaks down, possibly due to the loss of smoothness as the surfaces is stretched and folded back on itself [2, 7]. The dynamics on the HAO branch traverse a period doubling scenario.

Type	U_{app} [V vs. SHE]	f_1 [mHz]	f_2 [mHz]	f_e [mHz]	f_{HA} [mHz]
LA	5.84	40.10 ±0.69	45.58 ±0.69	6.91 ±0.69	
HA	5.84				46.03 ±0.80
LA	5.95	38.24 ±0.71	43.91 ±0.71	7.08 ±0.71	
HA	5.95				46.58 ±1.37
LA	6.05	37.54 ±0.86	42.66 ±0.86	6.83 ±0.86	
HA	6.05				45.55 ±1.09

Table 3.1: Table of frequencies in different states all measured with an external resistor yielding $6\,\mathrm{k\Omega cm^2}$. The leftmost column classifies the attractor of the states the second column gives the applied potentials and the rest frequencies from the normalised frequency spectra following the notation of Fig3.12

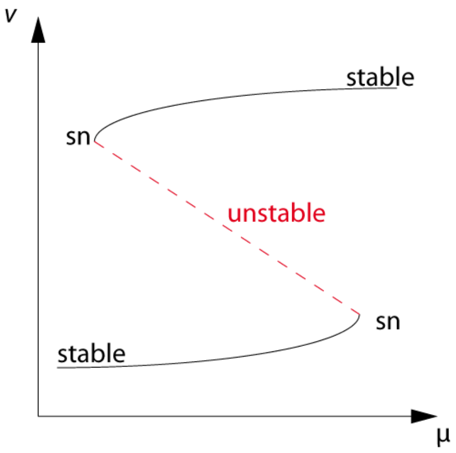

Figure 3.13: Sketch of a bifurcation diagram where a variable v is plotted vs. a parameter μ in a scenario where a hysteresis is confined by two saddle node bifurcations

A hysteresis like the one depicted in Fig.3.10 reminds of a common scenario where the hysteresis of two steady states is confined by two saddle node bifurcations. The scenario is also known for birhythmicity, where two limit cycles are created in a saddle node bifurcation of limit cycles, which might result in two stable limit cycles separated by an unstable one as depicted in Fig.3.11 a). We have sketched this scenario schematically in Fig.3.13. Here v is a variable which is plotted against a parameter μ. The black curves imply stable branches whereas the dashed red curve depicts an unstable branch. At each transition between stable and unstable branch is a saddle node bifurcation. In an experiment one can only measure the stable branches. Nevertheless if the hysteresis is confined by two saddle node bifurcations one knows that there has to be an additional unstable attractor of the same kind. In the case of the above presented bichaoticity it would be interesting two find out, if we see a similar scenario. One could speculate whether the torus bifurcation of the period-2 oscillation close to the existence boundary of the HAOs branch, is part of some kind of saddle node bifurcation where the saddle type limit sets originates from the LAOs branch. Due to the nature of the intrinsic coupling, i.e. the perturbation of a stable limit cycle by the ghost of the coexisting limit cycle, the question arises if the two limit cycles might also be separated by a unstable limit cycle or if the separatrix is more complex. As discussed above, with regard to Fig.3.11 b) we expect the separatrix to be much more complex than an unstable limit cycle, like it would be the case in Fig.3.11 b).

3.6 CONCLUSION

In this chapter we presented a detailed overview of the dynamics in the $R_{ext}A$-U_{app} parameter plane of the oscillatory electrodissolution of p-Si. We showed that the oscillatory region is, from the low voltage side, engulfed by LAOs which emerge from a Hopf bifurcation. For higher external resistances and potentials, a second type of oscillations exist, the so-called HAOs. The HAOs and the LAOs are separated by a region of complex and chaotic oscillations. In addition we presented the two saddle node bifurcation between which we find oscillations which are bistable with the stable node on the electropolishing branch in the CV.

We showed that in the region of the more complex oscillations a bistability between oscillations related to LAOs and oscillations related to HAOs exists. We could demonstrate that the 2-torus in the system emerges from the simple periodic LAOs and that it breaks as a strange attractor is created if one moves closer to the HAOs region in the parameter region. We showed that when coming from simple periodic HAOs and changing the parameters such that one enters the parameter regime of complex oscillations the system traverses a period doubling cascade. We exposed the HAOs oscillations to be the simple periodic oscillations of this period doubling cascade.

We showed that the two different routes into chaos are bistable. Hence we could show that the system is bichaotic. We argued that the complex behaviour as well as the bichaoticity is a result of an intrinsic coupling of the two limit cycles, as they approach each other in phase space upon parameter variations.

4

THE OSCILLATORY ELECTRODISSOLUTION OF N-DOPED SILICON

In this chapter we investigate the dynamics of n-doped silicon which is known to have an additional level of complexity, compared to the p-doped case, as it displays a multitude of different spatiotemporal patterns. The possibility of pattern formation during the oscillatory electrodissolution of n-doped Si has first been reported by Miethe et al. [57, 58]. In further studies on n-doped silicon WEs many interesting patterns have been reported like anti-phase clusters, subclustering and even completely selforganised chimera states as well as frequency clusters [65, 66, 86]. Although these phenomena have been carefully investigated, they have not been brought into context with the parameter space or different kind of couplings. In the n-doped case it is possible to induce other modes of coupling than in the p-doped case, as the amount of photo-generated valence band holes can be controlled via the illumination intensity. This makes it possible to control the strength of a nonlinear nonlocal coupling in the system by reducing the illumination intensity such that the production rate of the photo generated charge carriers is lowered to the same order of magnitude as their consumption rate in the oxidation process. This results in lateral variations of the hole concentration in the space charge layer and thus in the potential landscape, which can lead to pattern formation on the WE [67]. This additional parameter makes it possible to adjust birhythmic behaviour between two periodic limit cycles, and hence, proofs our assumption made in the previous chapter, where we suggested the whole system to be inherently birhythmic. This true form of birhythmicity was shown by Wiehl et al. [102]. In this chapter, as we turn our attention towards n-doped silicon, we show that in this case the dynamical behaviour of the system is also characterised by the inherent birhythmicity and that its behaviour is in many ways comparable to the p-doped case. We also show that the nonlinear nonlocal coupling, introduced by a reduced illumination, can lead to a spatial symmetry breaking. In addition we demonstrate that each spatiotemporal phenomenon can be related to either LAOs, HAOs or the interaction of both. We present all the different kinds of patterns encountered in the investigated parameter range, before we will discuss the influence of the illumination intensity and the external resistance on the dynamics. We will show that reducing the illumination leads to spatially less coherent states and that the external resistance has a homogenising effect on the spatial dynamics but also has similar effects on the temporal dynamics as it has in the case of p-doped Si demonstrated in chapter 3.

4.1 REVISITING THE SYSTEM

In this section, a brief introduction to the n-doped silicon system is given to equip the reader with sufficient insights for the results part. Under high illumination the system with n-doped silicon has merely quantitative differences to the one of p-doped silicon as WE, mainly due to the shift of the electrochemical potential [51, 65]. However, as the illumination intensity is lowered, some qualitative differences arise. These are linked to the response of the system to the limitation of charge carriers. We will demonstrate the role of the illumination intensity with the help of differently illuminated potential scans and revisit especially recent findings of Patzauer and Wiehl [64, 102] concerning the role of the illumination intensity for the birhythmicity in the system, which will help the reader to comprehend the results of this thesis.

Fig.4.1 shows four current-potential curves measured under different illumination intensities, all conducted with a scan rate of 20 mV/s. The black curve is a CV measured with a high illumination intensity of 12.3 mW/cm^2. The coloured curves are forward scans, where the potential was swept up to 8.65 V vs. SHE and then held constant. The red curve shows a scan with an illumination intensity of 1.26 mW/cm^2, the yellow curve was measured with an illumination intensity of 1.16 mW/cm^2 and the purple curve with an illumination intensity of 0.78 mW/cm^2. The measurements were performed by Yukiteru Murakami whose Master thesis [60] was supervised in the scope of this work.

The highly illuminated CV, depicted by the black curve in Fig.4.1, is exemplary for scan rates of 20 mV/s and looks, except for a potential shift of roughly 300 mV towards more cathodic potentials, identical to the ones of p-doped silicon electrodes. The explanation for the peaks and the plateau is thus analogously to the one given above (cf. Fig.3.1). The hysteresis is due to the higher scan rate. This results in a higher difference of the average current between forward and backward scan as the system does not have the time to settle to a quasi-steady state. Once a stable oxide layer has formed, the oscillatory character of the system can also be observed in Fig.3.1 however the amplitude of the oscillations are much smaller than for the black curve in Fig.4.1 measured at a higher scan rate. With a higher scan rate the displacement between the system stable state for a given applied potential and its actual state becomes larger. Hence the perturbation of the attractor is larger with a larger scan rate, which will result in a larger response and thus a larger oscillation amplitude. This holds especially for the backward scan as the equilibrium, upon reduction

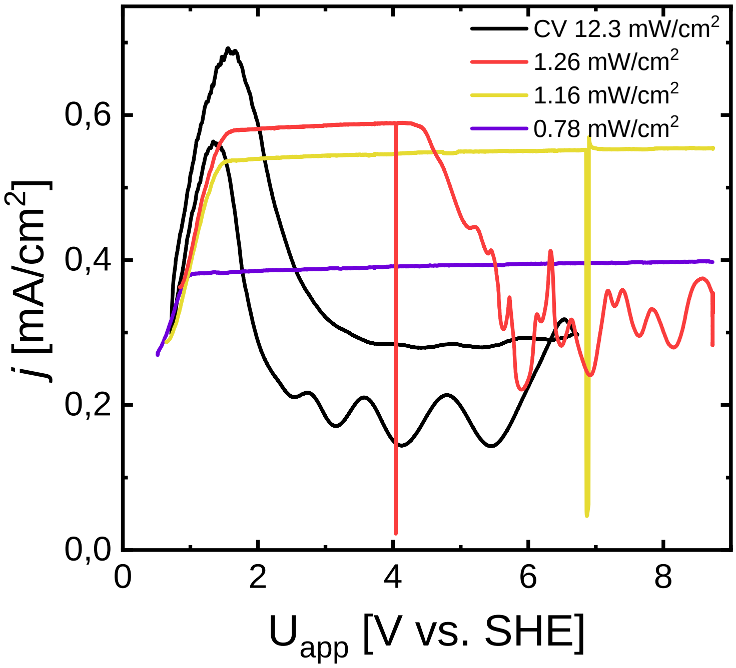

Figure 4.1: Potential scans of n-doped silicon with a scan rate of 20 mV/s. All scans started at 0.65 V vs. SHE. The scan depicted in black was performed under an illumination intensity of 12.3 mW/cm^2 up to an applied voltage of 6.65 V vs. SHE and back. During the other scans the potential was ramped up to 8.65 V vs SHE. The scan depicted in red was conducted under an illumination intensity of 1.26 mW/cm^2, the one in yellow under 1.16 mW/cm^2 and the purple one under 0.78 mW/cm^2.

of the potential, is found by a reduction of the oxide thickness [83] and thus the process is determined by the constant etch rate which is slow compared to electrically driven processes.

All of the potential sweeps performed under limited illumination of the WE, i.e. the red, yellow and purple curve first follow roughly the electropolishing branch of the CV until they run into a current density limit which is determined by the illumination intensity. This is a result of the limited number of photo-generated holes, which are needed for the oxidation process. The system then stays on this high current density plateau, even at potentials where a system with an excess of photo-generated valence band holes would attain much lower current densities and develop an oscillatory character. We suggest that this is because the system under low illumination never leaves the electropolishing branch, as the current, i.e. the oxidation reaction rate, is not large enough to form a stable oxide layer. Once the current limit in the scans with limited illumination intensity is reached, the current density stays almost constant over the plateau's potential range, except for a minuscule linear increase of the current with the applied potential. Only for a sufficiently high illuminated WE the amount of available charge carriers is sufficient for the reaction rate to exceed a threshold and form enough oxide such that the system attains the low current plateau of the CV. The latter can be observed for the scan with an illumination intensity $1.26\,\mathrm{mW/cm^2}$, for which the current drops down into the oscillatory regime at an potential of $4.40\,\mathrm{V}$ vs. SHE. Note that the slight linear increase of the current density on the plateau in the electropolishing regime is due to a higher internal quantum efficiency for higher applied potentials. The internal quantum efficiency is the ratio of the photo-generated charge carriers which contribute to the current density. By increasing U_{app}, the amount of recombinations of electron-hole-pairs in the bulk is reduced as the charge carriers are driven with higher force to the surface and thus their concentration in the bulk is reduced. These findings are extensively discussed in [60]. The two outliers, at roughly $4\,\mathrm{V}$ vs. SHE for the red curve and at roughly $7\,\mathrm{V}$ vs. SHE for the yellow curve are artefacts which result from a short interruption of the illumination.

The reduction of the illumination intensity to a point where the current on the electropolishing branch is limited can in a certain way be viewed as the application of an infinitely large resistor which becomes active at the respective threshold current density. Once the system has overcome the threshold for the formation of a stable oxide layer, it will show a similar bistability between the node on the electropolishing branch and the oxide covered oscillatory branch as the bistability that was demonstrated for p-doped silicon, which is shown in the previous chapter, in the CV under load in Fig.3.3. If we recall Fig.3.3 which shows that the introduction of a resistor introduces a linear load-line with a negative slope proportional to the resistance, it becomes clear how an infinite resistance will lead to a horizontal load-line and thus a cut-off of the current, as we observe it for the low illuminated potential scans in Fig.4.1. Note that a drastic reduction of the illumination intensity when the system is on the oxide covered current plateau will eventually lead to a dissolution of the stable oxide layer and the system will attain some state on the electropolishing branch with a current corresponding to the amount of photo generated valence band holes.

Now that we have a general idea on how the illlumination intensity on the WE can affect the current and therefore the oxidation rate, we can revisit some findings of Patzauer and Wiehl [64, 102] where they have demonstrated a birhythmicity between LAOs and HAOs, which can be found for lower illuminations. Fig.4.2 shows an LAO and an HAO limit cycle in the ξ-j phase plane, both measured at 5.65 V vs. SHE with $R_{ext}A$=1.00 kΩ/cm^2 and an illumination intensity of 1.36 mW/cm^2. The red cycle is an LAO and the black cycle an HAO. The LAOs have been initialised by switching on the illumination and jumping from open circuit potential (OCP) to 5.65 V vs. SHE, whereas the HAOs have been initialised by first illuminating with a higher intensity of 2.79mW/cm^2 as the potential was switched from OCP to 5.65 V vs. SHE. After two periods of the resulting transient oscillations the illumination intensity was reduced to 1.36mW/cm^2 which stabilised the HAOs limit cycle depicted in Fig.4.2 by the black curve and cut off its maximum current. Note that since both measurements have been conducted in the same series, the ellipsometric signal of both measurements are well comparable. The trajectories in Fig.4.2 move counter-clockwise. The median of the ellipsometric signal of the LAOs lies distinctly above the one of the HAOs.

As we follow the current of the HAOs from its minimum towards its maximum, i.e. from left to right on the lower part of the limit cycle, we see that it will run into a relatively sharp maximum before it drops down to a plateau at 0.53 mA/cm^2. The plateau is due to the limitation of the current through the reduced illumination intensity, i.e. the current maximum of the HAOs is cut off by the lack of charge carriers. Would the illumination intensity be further decreased the plateau current would be decreased as well, until it falls below a critical current for which the oxide layer will be dissolved and the system attains a state on the electropolishing branch [42]. We have seen in Chapter 3 that the HAOs can only be found if a certain $R_{ext}A$ value is exceeded. In the case of n-doped silicon the current limit which the HAOs run into seems to take the resistor's role stabilising the HAOs. We thus interpret the sudden lack of charge carriers as an infinite resistance which becomes active for a certain threshold current density which depends on the illumination intensity and stabilises the HAOs. The interpretation of this goes analogously to the idea of

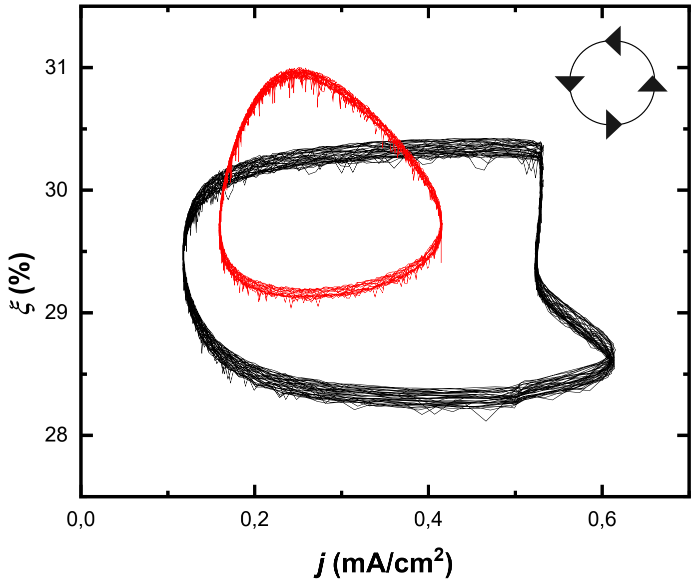

Figure 4.2: A LAOs (red) and an HAOs (black) limit cycle in the phase plane spanned by the current density, j, and the spatial average of the ellipsometric signal, ξ. Both states were measured with a n-doped WE at 5.65 V vs. SHE, $R_{ext}A$=1 kΩcm^2 and an illumination intensity of 1.36 mW/cm^2. The arrows indicate the direction of the trajectory.

the horizontal load line due to an infinite resistor which we brought up in the discussion of the illumination limited potential scans in Fig.4.1. However so far we argued that if both limit cycles approach each other in phase space, they will couple with each other which will result in deviations from periodic behaviour. But this is not the case for the coexistence of the two limit cycles in Fig.4.2. This is why we believe that limiting the current has the stabilising effect for the HAOs, analogously to the effect of an adequate external resistance but without the effect of coupling the two limit cycles like it is the case in section 3.5. This leads to a "classical birhythmicity", i.e. the coexistence of two periodic oscillations.

Reducing the illumination when the system is on an LAO will result in a spatial symmetry breaking on the WE which leads to lower global current instead of cutting off the current maximum, as it is observed for HAOs. Note that pattern formation at low illumination intensities is also observed during HAOs, but in the case of HAOs the current maximum is cut off by a sufficiently reduced illumination intensity. The reason why the LAOs rather undergo a spatial symmetry breaking than running into the current limit but the HAOs just run into it is not clear yet. We just mentioned that the HAOs can be stabilised even for low $R_{\text{ext}}A$ values by reducing the illumination intensity such the current oscillations are cut off. Fig.4.3 illustrates what this means for the parameter space as it exemplary depicts the $R_{\text{ext}}A$-U_{app} parameter plane for an illumination intensity of 1.2 mW/cm^2. The measurements depicted in Fig.4.3 were initialised by jumping from an HAOs state with an illumination intensity of 1.2 mW/cm^2 to the respective applied potential and external resistance. If the system bifurcates and starts exhibiting oscillations associated with the LA limit cycle we count them as LAO state. If the system settled on the HA limit cycle we additionally checked for bistability by perturbing the system with a relatively high illumination intensity above 2.5 mW/cm^2, such that the current maximum during the oscillations was not cut off any more. If the system continues with HAO dynamics, we counted the state as HAO state, but if the system attained an LAO state under the high illumination, we jumped back to the low illumination intensity of 1.2 mW/cm^2. If the system then stayed on the LAO state, we are in the coexistance region of the parameter space but if the system bifurcates back to HAO behaviour, only HAOs are stable for these parameters. Note that for the parameter space depicted in Fig.4.3 we only distinguished between HAO states and LAO states. This means we did neither distinguish between spatially homogenous and heterogeneous dynamics nor between periodic and complex oscillations as a detailed analysis of these phenomena will follow later in this chapter.

The figure shows a coloured area which marks the region where stable oscillations can be found. The oscillatory region starts at 3.65 V vs. SHE and an $R_{\text{ext}}A$ value of 1 kΩcm^2 and widens for larger applied

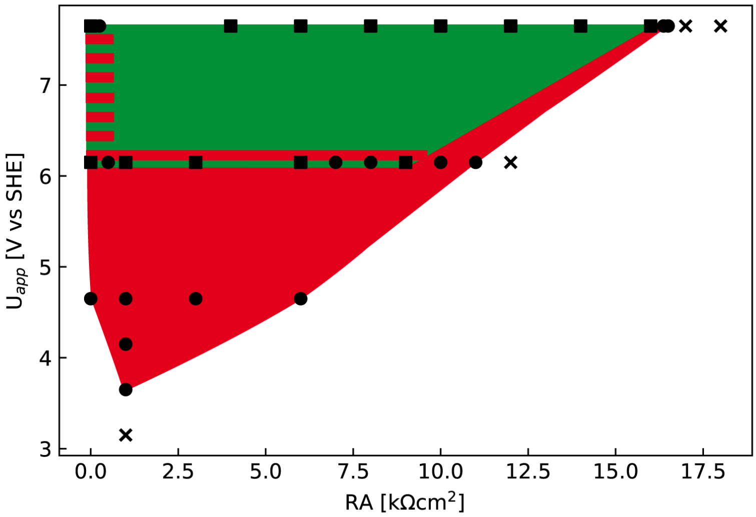

Figure 4.3: Parameter plane of n-doped silicon spanned by the applied voltage and the product of the external resistance and the active WE area at an illumination intensity of 1.2 mW/cm^2. In the red arean LAO states can be found in the green arean HAO states can be found and in the red and green striped area both can be found. The filled circles mark LAO states and the squares mark HAO states. The 'X' mark stable fixed points.

voltages, similar to the parameter plane for p-doped WEs depicted in Fig.3.4. The red coloured area is the parameter region where stable LAOs are found and the green coloured area is the region where stable HAOs are found. The red and green striped area indicates parameter regions in which both oscillation types can be initialised. The dots indicate measured LAOs and the squares are measured HAOs. The crosses indicate stable fixed points. Analogously to the p-doped case, the LAOs region encircles the oscillatory regime from the low voltage side. The main difference between the n-doped case with reduced illumination and the p-doped case is, that the HAOs can be found all the way down to zero applied external resistance. This is attributed to the reduced illumination which cuts off the maximum current during the HAOs which seems to have a stabilising effect on the HA limit cycle similar to the external resistance.

In this section we introduced the illumination intensity as parameter. We demonstrated its differences and analogies to the external resistor. The reduction of the illumination intensity, hence the limitation of charge carriers available for the oxidation process, allows for a bistability between the electropolishing branch and the oxide covered oscillatory branch. In addition, the lack of charge carriers seems to stabilise HAOs. In Chapter 3 we saw similar phenomena and attributed them to the effect of the external resistor. Here we argue that the current limit due to the reduced number of charge carriers acts like an infinitely large resistance and thus has similar effects on the dynamics as the external resistance. However limiting the illumination does not trigger the coupling between the two coexisting limit cycles as the resistor does. Otherwise we would expect deviations from periodic motion due to the intrinsic coupling as described in Chapter 3. Thus, in the n-doped case we find periodic coexisting HAOs and LAOs for sufficiently low $R_{ext}A$ values and illumination intensities.

In addition the illumination intensity plays an important role for the degree of synchrony on the WE as lowering it may result in pattern formation. This aspect will be thoroughly discussed in the following.

4.2 THE DIFFERENT SPATIOTEMPORAL PATTERNS

In this section we will give an overview of the different kinds of spatiotemporal dynamics which can be found during the electrodissolution of n-doped silicon. Of all the parameters we control during the experiment, the two which have the most influence on the homogeneity of the WE are the external resistor and the illumination intensity. Apart from its role in the intrinsic coupling of the two limit cycles creating temporal complexity, the resistor, which introduces a global linear coupling, has an homogenising effect on the spatial dynamics. A reduction of the illumination, hence a reduction of the charge carriers available for the oxidation reaction, on the other hand, introduces a nonlinear, nonlocal coupling, which seems to be a necessary requirement for spatial symmetry breaking. To understand how the nonlinear and nonlocal character of the coupling introduced by an adequate reduction of the illumination intensity comes about, we consider the following. If the illumination intensity is sufficiently low, such that the generation rate G of valence band holes is in the same order of magnitude as the reaction rate I, spatial fluctuations in the potential drop φ along the space charge layer and in the charge carrier density n_h at the WE surface lead to changes in the local current density. In addition these fluctuations lead to lateral motion of valence band holes, which are driven by gradients in their concentration as well as in the electrical field. Eq.4.1 gives an expression for this lateral movement which was derived by Patzauer et al. [67].

$$\frac{\partial n_h}{\partial t} = G - R + \frac{b_h k_B T}{e} \Delta n_h + b_h \mathbf{div}(n_h \mathrm{grad}\varphi), \tag{4.1}$$

with the combined recombination and reaction rates R, the hole mobility b_h, the Boltzmann constant k_b the temperature T and the elementary charge e. It now becomes clear, that Eq.4.1 is a reaction-diffusion equation with an additional nonlinear term. Thus the coupling which depends on both n_h and φ, is nonlinear. The nonlocal character is due to the relation between φ and n_h via Poisson's equation. Nevertheless, the dynamics found on n-doped WEs are also characterised by the inherent birhythmicity of the system, which means all spatial features can either be linked to HAOs, LAOs or are a result of the interaction of both. Consequently the framework of this sections is set to first present typical features found for the spatiotemporal dynamics related to LAOs followed by features observed in states related to HAOs. In the end we will investigate some mixed dynamics. Finally we will discuss where in the parameter space the different patterns are found.

4.2.1 *LAOs and their patterns*

Under high illumination the n-doped silicon system is very similar to the p-doped silicon system and only spatially homogeneous oscillations can be found. This means that under high illumination we can find the simple periodic as well as the more complex states presented in section 3.3. However, as the illumination intensity is reduced a spatial symmetry breaking in the ellipsometric signal can be observed. The characteristic patterns of the states arising during LAOs are wavefronts, irregular in period, direction and shape, which lead to spatiotemporal chaotic dynamics on the WE.

Fig.4.4 depicts a typical state that can be found if the illumination intensity is sufficiently reduced. This state was initialised by first switching the potential from OCP to 6.65 V vs. SHE with an illumination intensity of 2.72 mW/cm^2 and an external resistor yielding a $R_{ext}A$ value of 3.00 kΩcm^2. After two oscillation periods the applied voltage was decreased to 4.65 V vs. SHE which lead to homogeneous LAOs. Once the LAOs were stable the illumination intensity was reduced to 1.1 mW/cm^2 and the $R_{ext}A$ value increased to 5.00 kΩcm^2. At 4126 s the potential was increased to 5.25 V vs. SHE and after the transient had settled the state depicted in Fig.4.4 was recorded.

The colours give the intensity of the ellipsometric signal in arbitrary units, note that Fig.4.4 a) and b) share the same colour map which is indicated by the colour bar on the right side of the figure. Fig.4.4 a) is a snapshot of the electrode at t=4945 s. It is noticeable that regions of highest signal intensity in that snapshot form curved bands which appear to be irregular. On the left side there is a region of rather low signal encircled by a band of high intensity which ends at the left edge of the WE and on the opposite side there is an indication of a similar shape. The lower part of the electrode shows a rather straight and bright band followed by a very dark region at the lower edge of the WE. The magenta coloured line which reaches from the high left corner to the low right corner indicates the 1-dimensional cut along which the time series is depicted in Fig.4.4 b).

We now turn our focus towards the 1D spatiotemporal cut in Fig.4.4 b). The y-axis are the pixels along the cut and the x-axis is the time. Note that the upper side of the cut corresponds to the top left corner of the electrode. At t=4945 s is a magenta coloured dashed

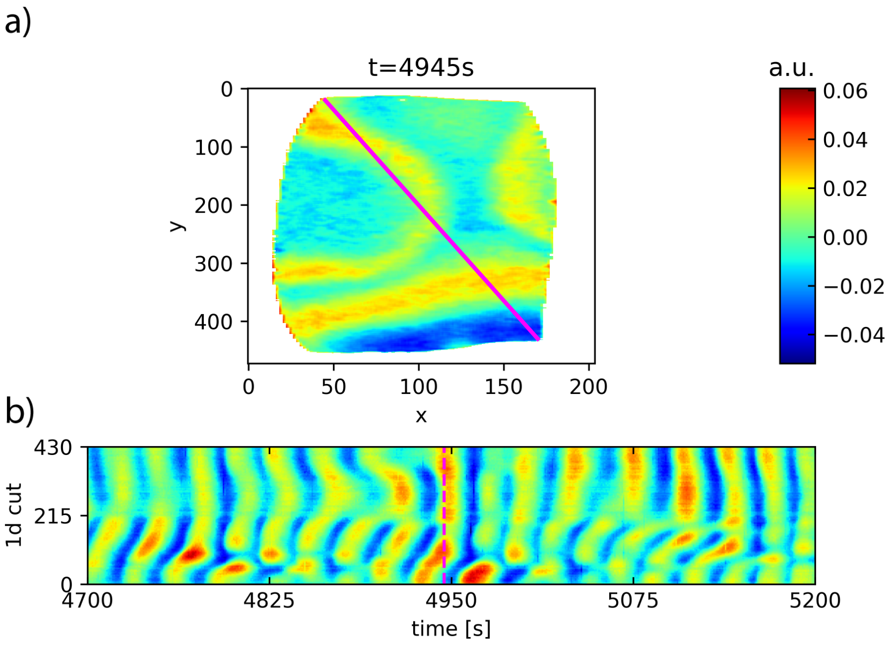

Figure 4.4: LAOs patterns (LAPAs) measured with an n-doped WE at U_{app}=5.25 V vs. SHE $R_{ext}A$=5 kΩcm^2 and an illumination intensity of 1.10mW/cm^2. a) depicts a snapshot of the WE taken at 4945 s and b) is the 1D spatiotemporal cut along the magenta coloured line in a). The top of the cut is the top left corner of the WE and the bottom is the lower right corner. The red dashed line in the cut marks the time of the snapshot.

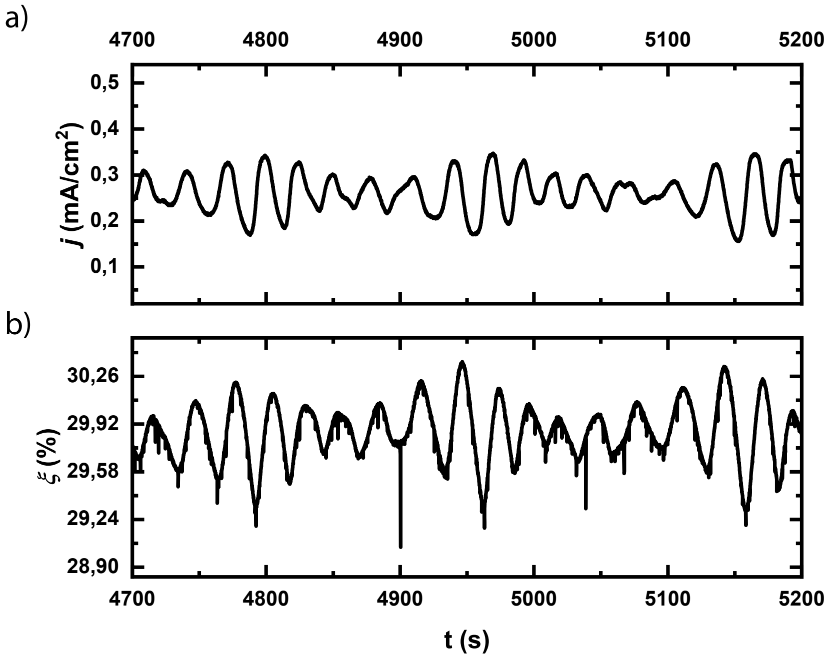

Figure 4.5: Time series of the global signals of the state depicted in Fig.4.4. In a) the current density and in b) the spatial average of the ellipsometric signal are shown. U_{app}=5.25 V vs. SHE, $R_{ext}A$=5 kΩcm^2, illumination intensity of 1.10mW/cm^2

line which indicates when the snapshot of Fig.4.4 a) is taken. It can be seen that the pattern is changing along the time axis and is thus not stationary. In addition, wave-like dynamics can be identified in the time series of the 1d-cut. Direction and shape of these wave fronts change irregularly and point towards changes in velocity or direction of the fronts. The spatial and temporal irregularities lead to spatiotemporal chaos. We have already shown that the LAOs emerge from a Hopf bifurcation. The spatiotemporal data of Fig.4.4 suggests that upon reduction of the illumination intensity the system undergoes a Benjamin-Feir instability which leads to spatial symmetry breaking, i.e. pattern formation. Note that the Benjamin-Feir instability is a well known scenario for pattern formation in reaction-diffusion systems close to a Hopf bifurcation.

Fig.4.5 depicts the time series of the current density in a) and the time series of the spatial average of the ellipsometric signal in b). Note that the time series shows complex behaviour which can be related to the spatial symmetry breaking.

Henceforth we will call this type of pattern LAOs pattern (LAPA).

4.2.2 *HAOs and their Patterns*

During the HAOs one can observe two types of spatially heterogeneous oscillations. The first type is observed during measurements with a low external resistor and high applied voltages and can be described as spatiotemporal chaos. For HAOs with a higher external resistance, the electrode splits up in two or more clusters which then seem to exhibit dynamics reminiscent of those in a period doubling cascade.

Fig.4.6 depicts the time series of the current density j and the spatial average of the ellipsometric signal ξ of an HAO state, which we show as an example of the first type of spatiotemporal pattern during HAOs with low external resistance. The state is initialised by switching from the OCP to 8.15 V vs. SHE with an applied resistor of 1.00 kΩcm^2 and a homogeneous illumination of the WE with an intensity of 3.04 mW/cm^2. After 60 s the illumination was reduced to 1.75 mW/cm^2 and subsequently increased to 1.86 mW/cm^2 after 492 s and finally to 1.99 mW/cm^2 after 847 s.

In the time series of the current density, depicted in Fig.4.6 a), it can be seen, that the maxima of the current density oscillations are cut off due to the low illumination intensity. As we have discussed above, cutting off the maximum of the current oscillations is the only way to stabilise HAOs for such low resistances. The cut off current oscillations are typically only found for HAOs, and are thus, the main reason we identified this state as an HAO state. The resulting current plateaus are all on the same level and have a spike at the end of the plateau, which is different to the HAOs depicted in Fig.4.2, where the spike appears prior to the current plateau like a current overshoot after the steep increase. The amplitude of the spike of the oscillations depicted in Fig.4.6 varies from period to period. Except for the variations of the current spike at the end of the current plateau the oscillations appear to be regular. The oscillations of the spatial average of the ellipsometric signal, depicted in Fig.4.6 b), are also approximately periodic but have slightly deviating maxima and minima.

Now we want to investigate the local behaviour of this state. Fig.4.7 a) shows a snapshot of the WE and Fig.4.7 b) the 1D spatiotemporal cut along the magenta coloured line in Fig.4.7 a). Fig.4.7 c) depicts the time series of the amplitude along the cut and d) is the phase. Amplitude and phase were obtained as described in section 2.3.2.

The snapshot clearly shows inhomogeneities over the entire WE. The signal appears irregular and somewhat cloudy, where most of the ellipsometric signal attains values within a narrow range, except for some isolated isles which appear two to three times brighter than the rest of the WE. In the cut in Fig.4.7 b) one can see the relatively strong variations of the local ellipsometric signal. It seems as if especially the local maximum values of the ellipsometric oscillations differ strongly. The overall oscillation period along the cut seems to stay more or less

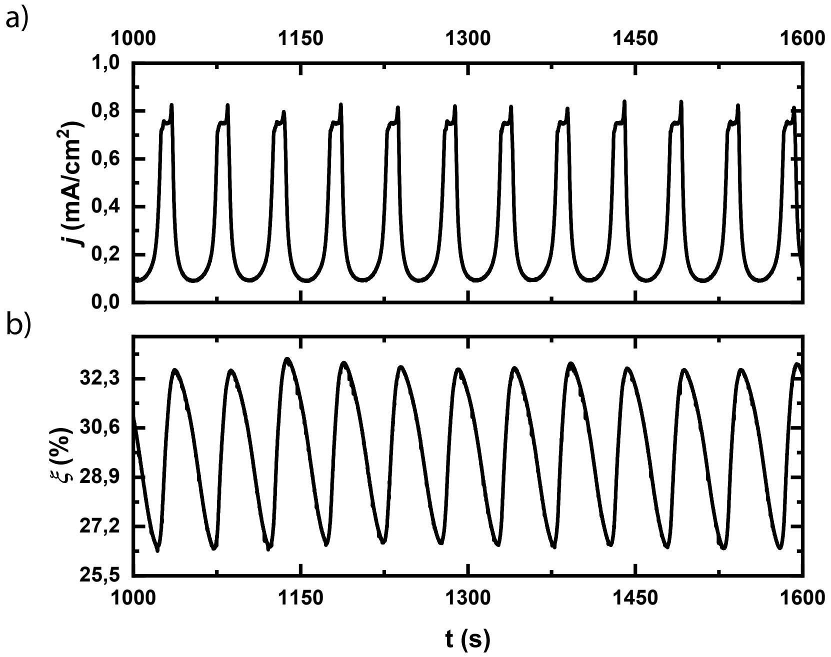

Figure 4.6: Time series of the current density in a) and the spatial average of ξ in b) of the state exhibiting the Type I HAOs patterns (Type I HAPAs) depicted in Fig.4.7. The state is measured at U_{app}=8.15 V vs. SHE, $R_{ext}A$=1 kΩcm^2 and an illumination intensity of 1.99mW/cm^2.

constant during the observed time range, although there seem to be spatiotemporal deviations of the period as well. These observations become even clearer as we take a look at the time series of the amplitude and phase signal along the cut in Fig.4.7 c) and d), respectively. In the amplitude signal one clearly observes distinct variations along the cut, not only in the maxima but also in the minima of the amplitude oscillations. Note that the amplitude of harmonic oscillations would be constant in time, but due to the relaxational character of the HAOs, one also observes periodic behaviour of the amplitude. But in the case at hand we observe spatial variations along the cut of the amplitude signal in addition to the periodic behaviour. Also the positions and intensities of the bright spots vary from period to period. The time series of the phase in Fig.4.7 d) confirms clearly that the overall period stays approximately constant along the cut, as all points on the cut exhibit roughly 12 oscillations in the investigated time range. Nevertheless, also the phase seems to display spatiotemporal chaotic behaviour. To further investigate these irregularities we take a look at the two white lines, drawn into the time series of the 1D-cut of the phase, between 1150 s and 1200 s. Both lines connect the two points of equal phase, i.e. both lines span one oscillation period of the local dynamics. We observe that the top line is much longer than the line below. The same two lines are also drawn into the time series of the

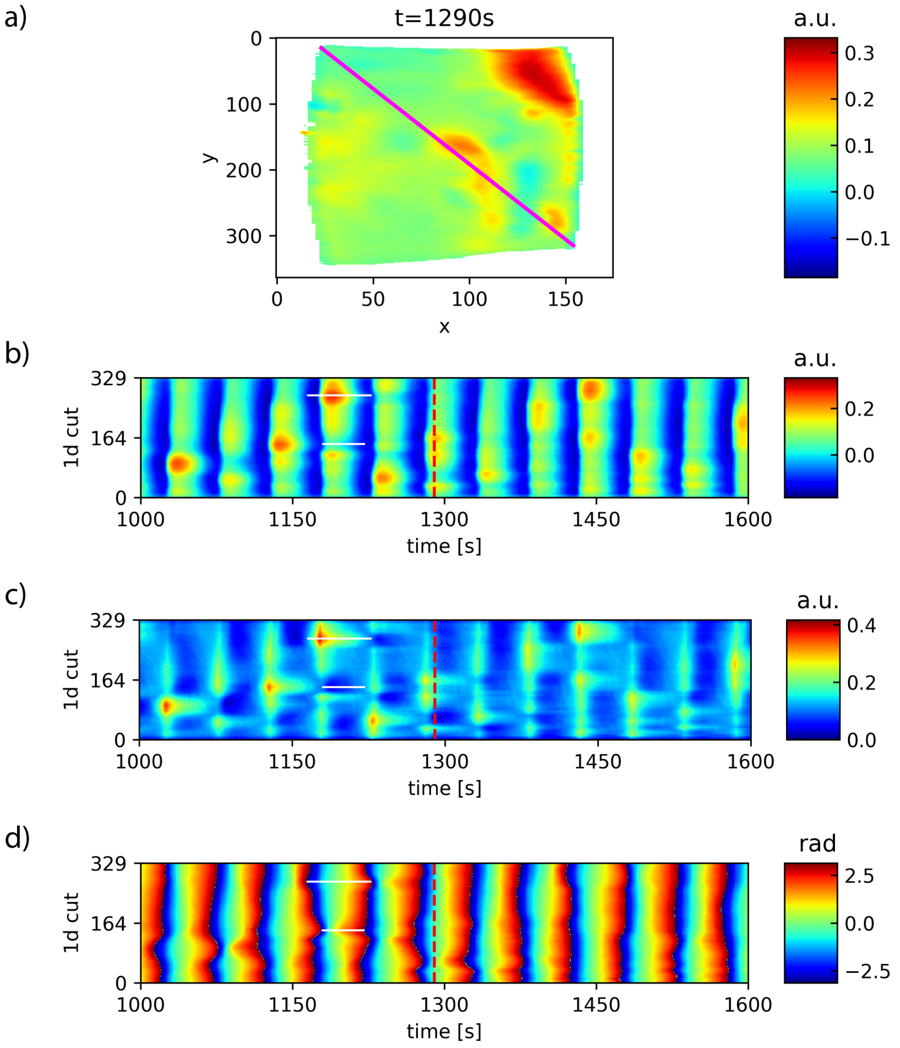

Figure 4.7: Type I HAPAs measured with a n-doped WE at U_{app}=8.15 V vs. SHE $R_{ext}A$=1 kΩcm^2 and an illumination intensity of 1.99mW/cm^2. a) depicts a snapshot of the WE taken at 1290 s and b) depicts the 1D spatiotemporal cut along the magenta coloured line in a). The top of the cut is the top left corner of the WE and the bottom is the lower right corner. The red dashed line in the cut marks the time of the snapshot c) is the amplitude along the 1D spatiotemporal cut. d) is the phase in the 1D spatiotemporal cut in radians. The white lines in the cut, each, covers one period at its positions.

1D-cuts along the amplitude and the ellipsometric signal. In the time series of the 1D-cut of the amplitude we can see that the position where the local oscillation period is long coincides with a particular high maximum of the amplitude oscillation. The position where the period is short, on the other hand, coincides with a particular low amplitude maximum. This behaviour, where large amplitude maxima lead to a longer local oscillation period as low amplitudes seems to be displayed throughout the entire time series of the 1D-cut. Furthermore we observe that wherever the maximum of the amplitude oscillation is particularly large in one period, the maximum of the consecutive period is particularly low. The latter observations also explains why the phase velocity distribution along the cut seems to be approximately flat, if averaged over the observed time frame, i.e. why all the pixels along the cut exhibit roughly 12 oscillation periods during the investigated time frame.

We suggest that the observed spatiotemporal behaviour is best characterised as amplitude turbulence similar to the amplitude chimeras reported by Zakharova et al. [106]. The main similarity to the amplitude chimeras is that the spatiotemporal behaviour is characterised by local amplitude variations with a flat local distribution of the average phase velocity. In [106] the oscillators with low amplitude have, averaged over one period, the same phase velocity as the ones with a high amplitude. In our case, the instantaneous phase velocity of oscillators with a high a instantaneous amplitude is lower then the one for low amplitudes. However, long term phase displacements between the pixels are suppressed by the peculiar phenomenon, that the local time series show a low amplitude maximum in an oscillation period consecutive to one with a high maximum amplitude. Hence, the condition of a flat spatial distribution of the average phase velocity is, in our case, only true if the average is taken over several periods. From here on we will refer to this behaviour as Type I HAOs pattern (Type I HAPA).

A different type of spatiotemporal patterns can be found for HAO states with a large external resistance. Note that we started scanning the parameter space with very slow CVs to get a better overview of the system's general behaviour, as some of the dynamical phenomena can only be found in a narrow parameter region and could be easily skipped if the parameter space is investigated at discrete values under constant conditions. In addition, the dynamics showed themself to be highly sensitive towards the sample's measurement history, which lead to a higher reproducibility of the slow CVs compared to discretely sampling the parameter space. Many of the phenomena which occurred during the scans could also be observed under steady conditions, however not all parameter regions have been revisited in potentiostatic measurements, and thus some of the states, like the ones shown in the following, have so far only been measured during potential sweeps.

Fig.4.8 a) depicts the time series of the current density and b) of the spatial average of the ellipsometric signal, measured during a slow CV with a scan rate of 0.3 mV/s, an external resistor of 6.00 kΩcm^2 and an illumination intensity of 0.95 mW/cm^2. The CV started from an LAO state at relatively low applied voltages, from where the potential was swept towards higher potentials and then back again towards low potentials. Eventually the system would undergo a transition from an LAO state to an HAO state in the forward scan and a transition back to an LAO state in the backward scan. The parameters for which these transitions occur together with the types of transition will be discussed later in this chapter. Fig.4.8 depicts an HAO state which was measured right after the the transition from an LAO state in the forward scan of the CV. Due to the low illumination intensity, the maxima of the current density oscillations depicted in Fig.4.8 a) are cut off and show the typical current plateau similar to the ones in Fig.4.6. The difference is that in Fig.4.8 a) the large current spikes are in the beginning of the current plateau, whereas in the state depicted in Fig.4.6 they are at the end of the plateau. The current plateaus and the current minima seem to be constant whereas the height of the spikes and the width of the plateaus show period-two behaviour. The oscillations of ξ, depicted in Fig.4.8 b) display also a distinct period-two behaviour where the large maximum of ξ follows a large spike in the current density. Now we turn our focus on the spatial features of this state. The snapshot of the WE depicted in Fig.4.9 a) shows a region on the left side of the WE where the local signal is much higher than on the rest of the WE surface. In the cut in Fig.4.9 b) one can see that the electrode has split into two clusters which both seem to exhibit period-two behaviour at first, where the large maximum of the one cluster coincides with the small maximum of the other cluster. However the period-two behaviour in the lower half of the cut seems to fade after some time. Also the region where we observe a distinct period 2 behaviour shrinks in time. To get more insight on the local dynamics the local time series of two points along the cut are plotted in Fig.4.10. Fig.4.10 a) depicts the time series of the ellipsometric signal in $(x, y) = (185, 213)$ and Fig.4.10 b) depicts the one in $(x, y) = (45, 213)$. The time series in Fig.4.10 a) shows a distinct period-two behaviour and has a similar shape as the one of the spatial average of ξ, depicted in Fig.4.8 b). The time series in Fig.4.10 b) shows a period-two behaviour in the beginning, which is by far not as distinct as in Fig.4.10 a) and fades after nine periods. This confirms the observation made above, that the period 2 behaviour is displayed especially in the top part of the cut. It is not really clear whether the state where both cluster perform period-two oscillations would be stable or transient under constant parameters. The state depicted in Fig.4.9 is characterised by a cluster

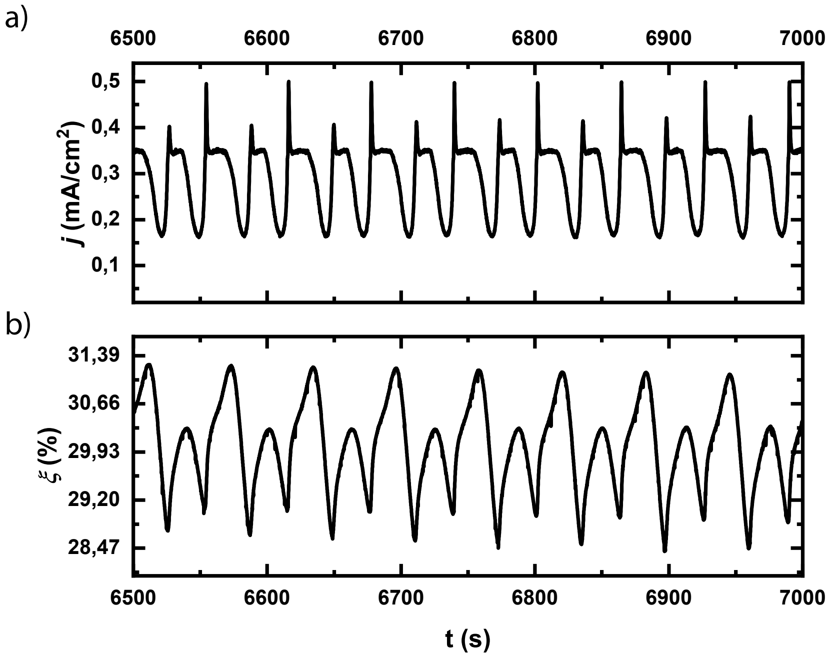

Figure 4.8: Time series of the current density in a) and the spatial average of ξ in b) of the state exhibiting type II HAOs patterns (Type II HAPAs) depicted in Fig.4.9. Measured with a n-doped WE at U=6.70-7.05 V vs., SHE $R_{ext}A=6\,k\Omega cm^2$ and an illumination intensity of 0.95 mW/cm^2.

formation on the WE and a period-two behaviour of parts of the WE and of the global signals, i.e. the spatial average. Apart from some transient behaviour which can probably be related to the potential sweep, the spatiotemporal behaviour appears to be periodic.

In contrary to this rather uniform spatial behaviour shown in Fig.4.9, we take a look at a similar state, which displays less spatially uniform behaviour. The state was measured during a slow CV with an external resistor yielding $R_{ext}A=6\,k\Omega cm^2$ and an illumination intensity of the WE of 1.2 mW/cm^2. This time the state was found immediately prior to the transition from an HAO state to an LAO state during the backward scan. Fig.4.11 a) depicts the time series of the current density and b) the time series of the spatial average of ξ. The maxima of the oscillations in the current density are slightly cut off due to the low illumination frequency, but not as pronounced as in previously presented states. The current minima are alternating between high and low values which gives the current oscillations a period-two character. The time series of the spatial average of ξ also shows period-two behaviour. The overall dynamics in the time series of the global signals seem to be uniform. Let us now turn our focus to the spatiotemporal dynamics on the WE. The snapshot of the WE in Fig.4.12 a) shows nicely how the electrode splits up into two parts. One can see that the majority of the left side of the WE shows a relatively high signal compared to the

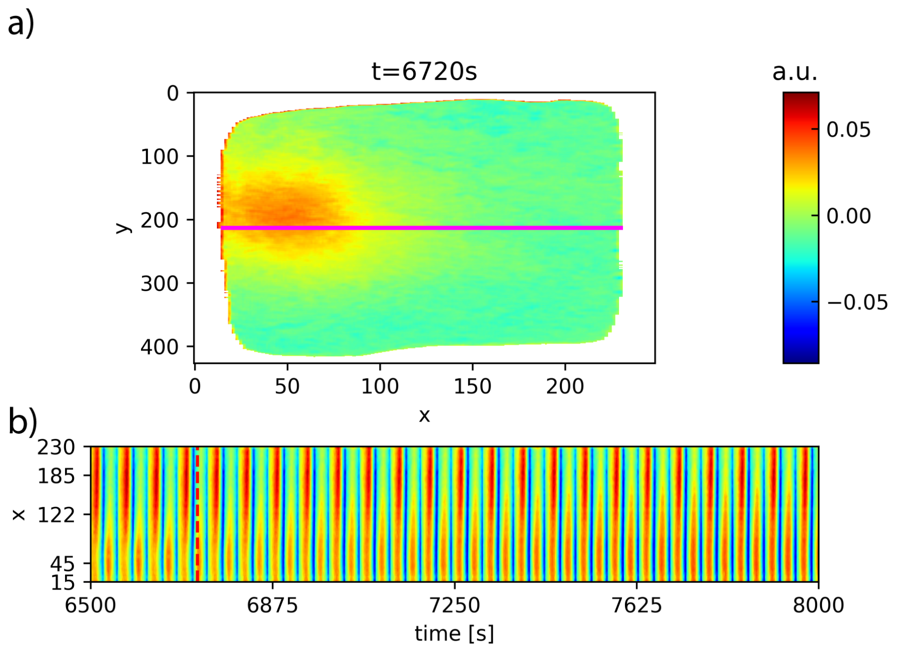

Figure 4.9: Type II HAPAs measured with a n-doped WE at U=6.70-7.05 V vs., SHE $R_{ext}A$=6 kΩcm^2 and an illumination intensity of 0.95 mW/cm^2. a) depicts a snapshot of the WE taken at 6720 s and b) depicts the 1D spatiotemporal cut along the magenta coloured line in a). The top of the cut is the right side of the WE and the bottom is the left side. The red dashed line in the cut marks the time of the snapshot.

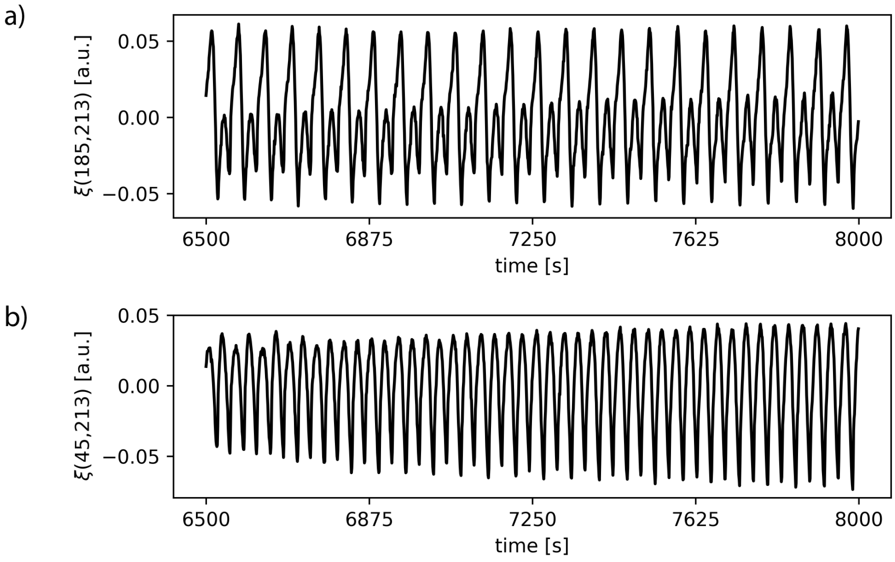

Figure 4.10: Local time series of ξ of the Type II HAPA state depicted in Fig.4.9 at two different pixels of the 1D spatiotemporal cut. a) time series of $X = 185$ and b) at $x = 45$. $U_{app} = 6.70 - 7.05$ V vs. SHE $R_{ext}A$=6 kΩcm^2 and an illumination intensity of 0.95 mW/cm^2.

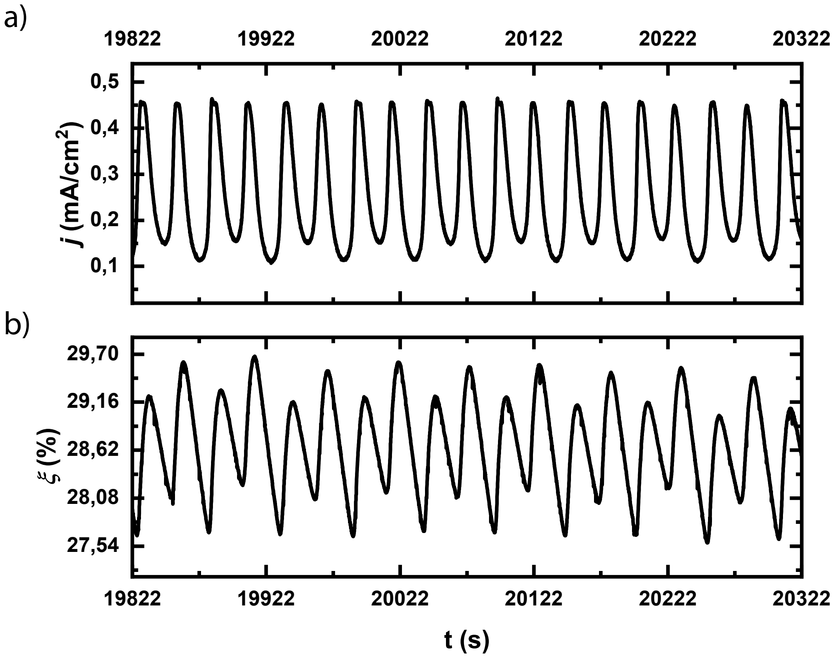

Figure 4.11: The time series of the global signals from the Type II HAPA state depicted in Fig.4.12. In a) is the current density and b) is the spatial average of ξ. Measured with a n-doped WE at U=6.60-5.55 V vs., SHE $R_{ext}A$=6 kΩcm^2 and an illumination intensity of 1.2 mW/cm^2.

right side of the electrode. When looking at Fig.4.12 b), one observes that both cluster on the electrode exhibit non-periodic oscillations. The local maxima and minima of the ellipsometric signal vary strongly and it appears as if one cluster often has a large maximum when the other cluster has a low maximum. Fig.4.13 shows the local time series of the ellipsometric signal of two points along the cut. Fig.4.13 a) shows the local time series at $(x, y) = (185, 215)$ and Fig.4.13 b) the time series at $(x, y) = (45, 215)$. Both oscillations appear non-periodic but have a period four character. Upon a close look at a) one recognises that the oscillations follow a pattern in which every second maximum is lower than its consecutive maximum but the second and third maxima are both larger than the fourth and fifth maxima, the forth and the fifth maxima are in turn smaller than the sixth and seventh maxima and so on. This means that the oscillation of the local signal is not truly alternating between high and low maxima, like it would be the case of a state in the period doubling cascade, but it is rather that groups of two maxima are alternating in height. Furthermore the first maximum within these groups is always smaller than the second one. The direct comparison between the time series in a) with the one in b) shows that the one depicted in b) displays qualitatively the same behaviour as the one depicted in a). However it appears that whenever a) is in an episode of two large maxima b) is often exhibiting two small maxima.

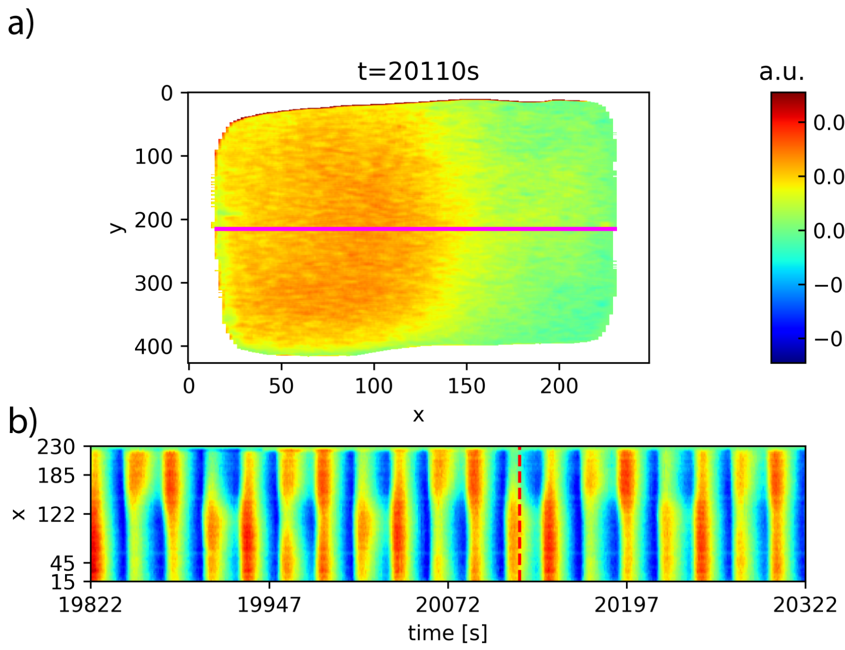

Figure 4.12: Type II HAPAs measured with a n-doped WE at U=6.60-5.55 V vs., SHE $R_{ext}A$=6 kΩcm^2 and an illumination intensity of 1.2 mW/cm^2. a) depicts a snapshot of the WE taken at 20110 s and b) depicts the 1D spatiotemporal cut along the magenta coloured line in a). The top of the cut is the right side of the WE and the bottom is the left side. The red dashed line in the cut marks the time of the snapshot.

This shows that only the modulation of the oscillations of the two cluster are in a kind of antiphase configuration, however, both cluster will be in a maximum at the same time.

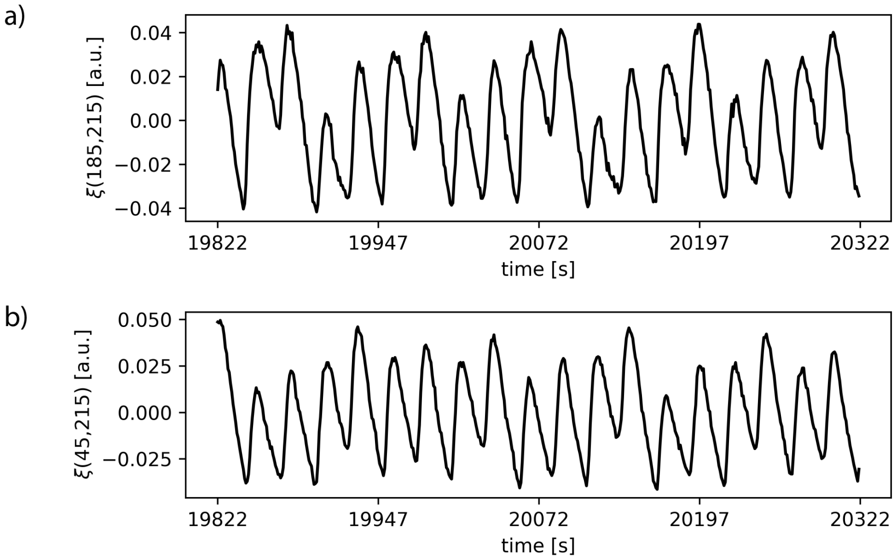

Figure 4.13: Local time series of ξ of the Type II HAPA state depicted in Fig.4.12 at two different pixels of the 1D spatiotemporal cut. a) time series of $X = 185$ and b) at $x = 45$. $U_{app} = 6.60 - 5.55$ V vs. SHE $R_{ext}A$=6 kΩcm^2 and an illumination intensity of 1.2 mW/cm^2.

The state depicted in Fig.4.9 and the one in Fig.4.12 have in common that in both cases the global signals, i.e. the current density and the spatial average of ξ exhibit period-two oscillations and that in both cases the WE splits up into two cluster. As the cut off of the current maximum is a typical feature of the HAOs, we will classify this type of pattern as an HAO state. Henceforth we will denote this type of HAOs pattern Type II HAOs pattern (Type II HAPA). The differences between the two examples presented for the Type II HAPAs will be discussed later in this chapter, where the different states will be contextualised within the parameter space. For now we claim that the period-two character displayed by the Type II HAPAs has its origin in the intrinsic coupling between the HA limit cycle and the LA limit cycle, as these states arise close to the transitions from an LAO state to an HAO state or vice versa. Note that Type II HAPAs are especially found for higher external resistances opposed to the Type I HAPA which is found for low resistances. Hence, another strong indication that the applied external resistor is strongly related to the intrinsic coupling between LAO limit cycle and the HAO limit cycle.

4.2.3 *The Mixed States*

In the previous part we presented spatiotemporal heterogeneities which we think are related to dynamics either primary dominated by the LAO mechanism as in Fig.4.4, or the HAO meachanism as in Fig.4.7, Fig.4.9 and Fig.4.12. In the following part, we will show some states displaying features of both types of oscillations.

Fig.4.14 shows a state which was initialised by switching the potential from OCP to 7.18 V vs. SHE while the WE was illuminated with an intensity of 2.28 mW/cm^2 and an external resistor was inserted yielding $R_{ext}A$=3.00 kΩcm^2. This resulted in a homogeneous but non-periodic type of LAOs. After t =689 s the illumination was reduced to 1.21 mW/cm^2 and the system attained the state depicted in Fig.4.14.

The snapshot illustrated in Fig.4.14 a) was taken at t=2425 s. The upper left corner has a higher signal than the right part of the WE. This brighter part seems to be separated from the darker part by two curved bands, where the left one is a local minimum and the right one a maximum.

The spatiotemporal dynamics in Fig.4.14 b) exhibits initially rather coherent oscillations with comparably high amplitudes. The oscillation frequency increases abruptly after the first three oscillations and the maximum value of the oscillations decreases. After about four of this faster oscillations a nucleus of a second oscillation phase with larger period forms at the top left corner of the WE. This can be seen in a discontinuity in phase in Fig.4.14 b). In the following, this nucleus spreads, oscillation by oscillation, further into the WE. The amplitude of the oscillations in the nucleus are smaller, the maxima are less defined and they seem to drift apart in time, i.e. they tend towards lower frequencies. The oscillations outside this nucleus seem to be unaffected by the dynamics spreading from the top left corner of the WE. Only in some intermediate region, some wave like transition between the two phases manifests itself in the time series of the 1D-cut. As the state which spreads over the WE covers about half of the active area, a checker board pattern emerges in the 1D-cut with isles of relatively high intensity. This checker board pattern in the 1D-cut corresponds to adjacent bands on the WE which are in antiphase configuration, as can be observed in Fig.4.14 a). Once the state has spread over the whole WE the checker board pattern starts homogenising until the system jumps back to the homogeneous state with the higher frequency. After a few periods, a new nucleus of the slow oscillations forms again and the whole process repeats. This cycle between the two states is stable and repeats itself over several thousand seconds.

The process of a nucleus emerging on an oscillating background and spreading over the WE under the formation of checker board patterns in the time series of the 1D-cut is reminiscent of the stepwise phase dependent transition from HAOs to LAOs whose frequencies are locked in a 1:2 ratio [102]. In each period of the HAOs, the LAOs phase spreads a little further into the HAOs region. As this process occurs in each period of the HAOs and as the frequencies of the two phases are locked in a 1:2 ratio, the checker board pattern emerges in the time series of the 1D-cut. On the WE the checkerboard pattern manifest itself as a series of bands spreading over the WE, in antiphase configuration, oscillating with half the frequency of the HAOs. Hence we identify the homogeneous oscillations with the high frequency as HAOs and the parts which spread from a nucleus as LAOs. It seems that the transitions back to the HAOs are preceded by a homogenisation process during the LAOs.

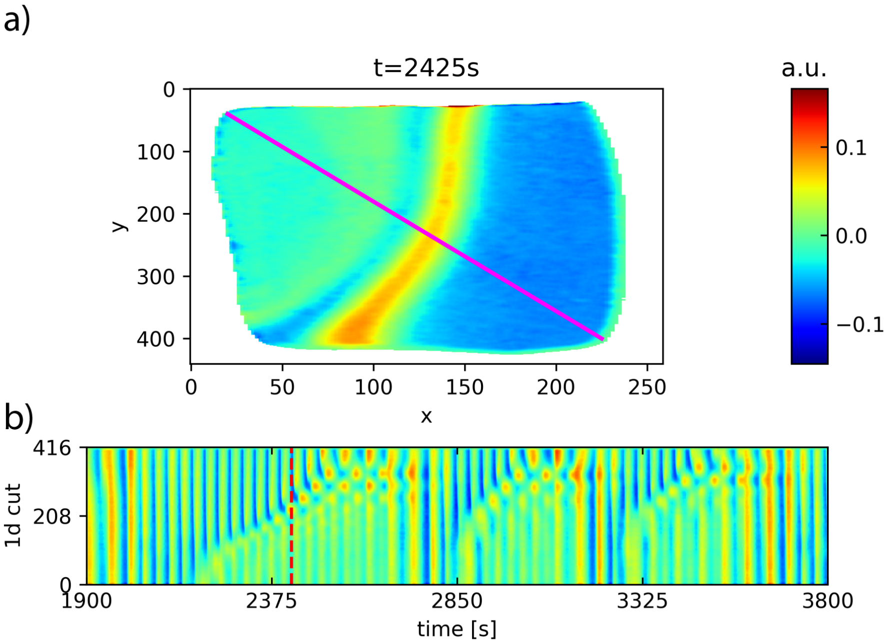

Figure 4.14: Double metastable (DOMES) pattern measured with an n-doped WE at U=7.18 V vs. SHE, $R_{ext}A$=3 kΩcm^2 and an illumination intensity of 1.21mW/cm^2. a) depicts a snapshot of the WE taken at 2425 s and b) depicts the 1D spatiotemporal cut along the magenta coloured line in a). The top of the cut is the lower right corner of the WE and the bottom is the top left corner. The red dashed line in the cut marks the time of the snapshot.

Fig.4.15 depicts the time series of the current density in a) and the one of the spatial average of ξ in b). The current oscillations show, during the time when only HAOs are present on the WE, some of the typical features of the HAOs, which are a cut off maximum and a relatively high amplitude. As the phase of LAOs forms on the WE and spreads, the amplitude of the current oscillations decreases, until the dynamics suddenly switch back to HAOs and the amplitude of the current oscillations increases drastically. The time series of ξ displays a similar behaviour.

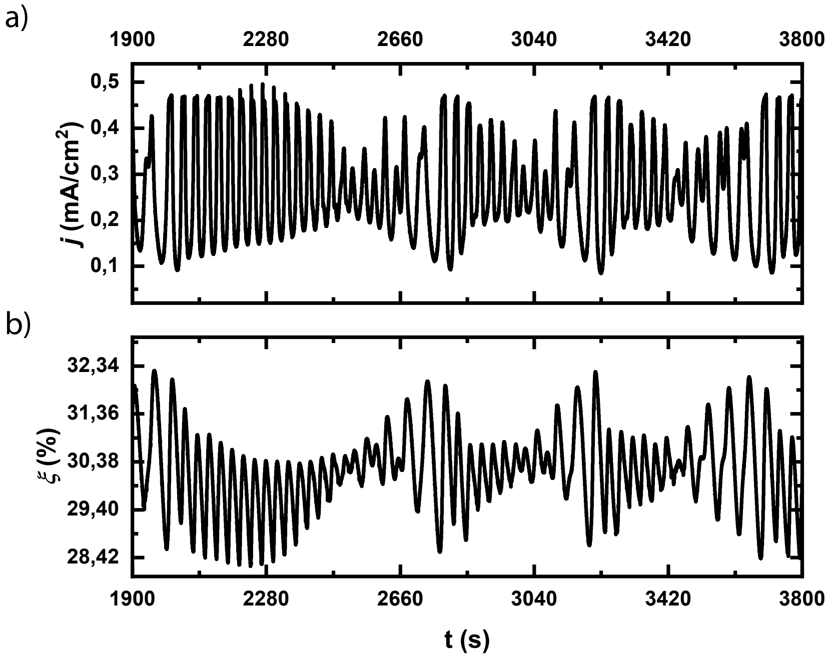

Figure 4.15: Time series of the global signals during the DOMES pattern depicted in Fig.4.14. a) the current density and b) the spatial average of ξ. Measured with an n-doped WE at $U_{app} = 7.18\,V$ vs. SHE, $R_{ext}A=3\,k\Omega cm^2$ and an illumination intensity of $1.21 mW/cm^2$.

This self-organised repeating transitions between the two states is peculiar, as one would expect for a bistable system, that either one of the two states is metastable and the other one is globally stable, or both are equally stable. In the first case, the system should settle in the globally stable state and in the latter case, when the system is at its equistability point, one would naively expect that neither of the two states spread over the electrode as both are equally stable. That is why we think that the state depicted in Fig.4.14 is a double metastable state, which means that the HAO state and the LAO state are both metastable for the given parameters. To further elaborate on what this means and how such a state could arise, we take a look at Fig.4.16, where we have sketched different configurations of nullclines of a bistable two dimensional reaction-diffusion system with the two variables u and v in Fig.4.16 a) and b), and the potential landscape of the mechanical analogue for $v = v_1$ and $v = v_2$ in c) and d), respectively. Fig.4.16 a) shows the z-shaped nullcline of the variable u which has a fast time scale compared to v. The two green lines are two different possible cases for the nullclines of v. Both are constant in v, one at $v = v_1$ and the other at $v = v_2$. P_1 and P_2 mark the two fixed points

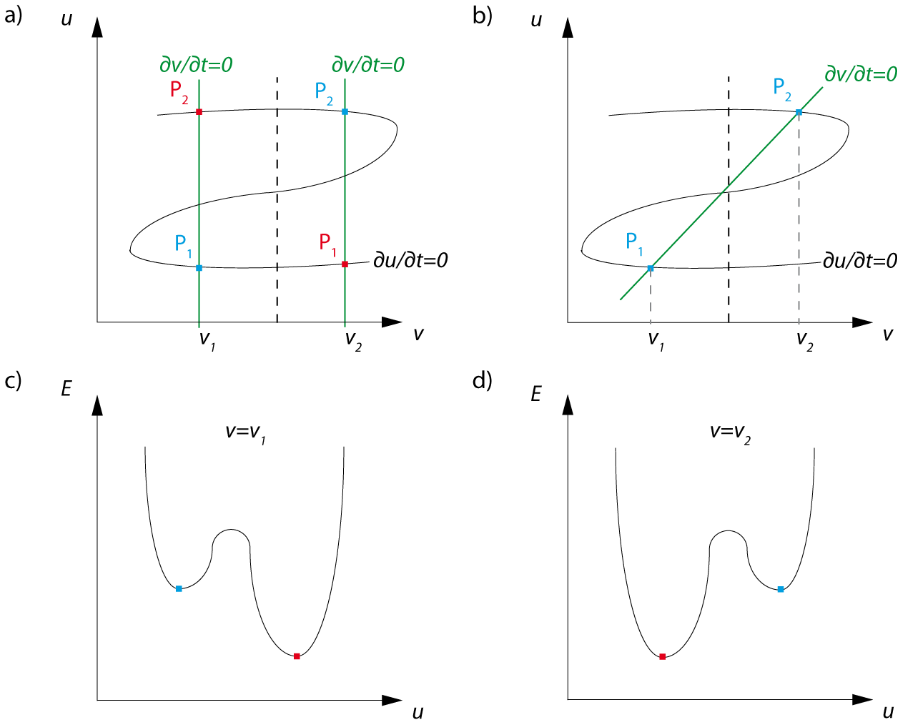

Figure 4.16: In a) and b) two exemplary sketches of different configuration of intersecting nullclines in the phase plane spanned by the variables u and v. a) depicts two cases for the position of a vertical v-nullcline intersecting the z-shaped u-nullcline. In the first case at $v = v_1$ and the second case at $v = v_2$. Each case is on one side of the system with respect to equistability point (dashed line). b) depicts the case for a non-vertical v-nullcline intersecting the u-nullcline such that the two stable fixed points, P_1 and P_2, are each on one side with respect to the equistability point (dashed line). c) and d) depicts two exemplary sketches of the potential landscape of the mechanical analogue for the case of a vertical v-nullcline at $v = v_1$ and $v = v_2$, respectively.

for each position of the v-nullcline. A red point is globally stable in the respective configuration and a blue one is metastable. For a better visualisation of this concept we take a look at the potential landscapes in Fig.4.16 c) and d). Fig.4.16 depicts the case at $v = v_1$. Here the two minima of E are stable fixed points whereas the maximum is the unstable fixed point. It can be seen that less energy is needed to perturb the system such that it moves out of the basin of attraction of the metastable fixed point at small u than it is needed to leave the basin of attraction of the globally stable fixed point for large u. In the other case, as the vertical v-nullcline is located at $v = v_2$ in Fig.4.16 a), the potential landscape has changed to the one depicted in Fig.4.16 d). Now P_2, i.e. the stable fixed point at large u, is the metastable fixed point and P_1 is the globally stable one. Note that the qualitative difference of these two cases is the relative position of the v-nullcline to the equistability point. The equistability point is indicated by the dashed line in Fig.4.16 a) and is the point where the potentials of the two fixed points would be on the same level, and thus equally stable. The nullclines drawn in Fig.4.16 b) draw another picture. Here the v-nullcline is not constant in v, but has a slope and crosses the equistability point in a way that both stable fixed points are metastable. As the system attains P_1 at $v = v_1$, the analogous potential landscape is that of Fig.4.16 c). If the system is then adequately perturbed, it would move fast to the upper branch of the u-nullcline and from there it would move slowly towards P_2. As it attains the state at P_2, the analogous potential landscape is that depicted in Fig.4.16 d), and thus P_2 is also metastable. Hence, we call this state a double-metastable state (DOMES). Double metastable states have also found in numerical investigations of spiral waves during the CO oxidation on Pt, where in a bistable parameter region two different front solutions could be found, both unstable to a supercritical nucleus [9]. However in this case we seem to have two metastable oscillatory states, which has, to the best of our knowledge, not been reported so far.

The next state we want to present is the coexistence of an LAO state and an HAO which are spatially separated on the WE. Fig.4.17 depicts a state in which a part of the WE seems to exhibit LAOs locked to half the frequency of the HAOs which are active on the other part of the WE. This state has never been completely stabilised, however the transients are so slow that the spatial coexistence of the LAO and the HAO state persists for several thousand seconds.

To adjust this state, we first let the system attain HAOs at 6.65 V vs. SHE with an external resistor yielding $R_{ext}A$=4.77 kΩcm^2 and an illumination intensity of 2.79 mW/cm^2. After 500 s the illumination was reduced to 1.21 mW/cm^2 and the resistance lowered to $R_{ext}A$=1.00 kΩcm^2. Subsequently the applied voltage was reduced to 5.65 V vs. SHE. Now the system exhibits homogenous HAOs. We then perturbed this state with a heterogeneous illumination for 60 s , such that the rightmost 1/3 of the WE is illuminated with an illumination intensity of 3.62 mW/cm^2 while keeping the remaining two thirds of the WE illuminated with 1.2 mW/cm^2. After 60 s of heterogeneous illumination we switched back to a homogeneous illumination of 1.2 mW/cm^2.

Fig.4.17 a) shows a snapshot of the WE taken at t=4500 s. It can be seen that the electrode is seperated into two regions. The one in the upper right corner shows a relatively low signal at the time of the snapshot and the other region a rather medium signal. The two regions are separated by a bright band.

Fig.4.17 b) depicts the 1D spatiotemporal cut of the measurement, beginning when the heterogeneous illumination was introduced. The black dashed line marks the moment when the illumination was switched back to homogeneous 1.2 mW/cm^2. One can see, that the local increase of the illumination induced heterogeneities in the top half of the cut, which persist even as the illumination is switched back to homogeneous 1.2 mW/cm^2. In the beginning these heterogeneities will arrange themselves to a synchronised region which oscillates slower but with a higher amplitude than the initial HAO state. The lower border of this region then moves towards the top while the region also grows and spreads towards the top edge. Once it reaches the top edge of the electrode at roughly t=4300 s, the lower border of the region will slowly start spreading. At roughly t=7000 s the LAOs region develops some heterogeneities reminiscent of LAPAs and at about t=8000 s the spreading of the slower oscillations accelerates until the whole electrode is covered by the slow oscillating phase before it globally switches back to the initial state. Quickly after the transition to the initial HAO state, a nucleus of the slow oscillations forms again, only this time it is in the bottom of the cut.

To further elucidate the dynamics, Fig.4.17 c) depicts a magnification of the 1D spatiotemporal cut between t=4500 s and t=6000 s. In the zoom one clearly recognises the two described regimes. The two different dynamics are phase locked at their border. The main frequency of the oscillations in the top part seems to be 1/2 of the one in the bottom part. The oscillations in the top regime with the higher amplitude is simple periodic, however its maxima become narrower towards the border of the two states. In addition the region loses homogeneity as the oscillations at the top edge of the cut evolve a wavefront character at roughly 4800 s. The wavefront propagates from the top of the cut towards the centre of the slow oscillating region, from where on the rest of the region is approximately homogeneous. The wave character at the top of the cut becomes more pronounced with time. The lower part of the cut exhibits Type II HAPAs, with a main frequency twice as high as the one in the upper region. The region of Type II HAPAs has split into three clusters, each exhibiting period-two oscillations.

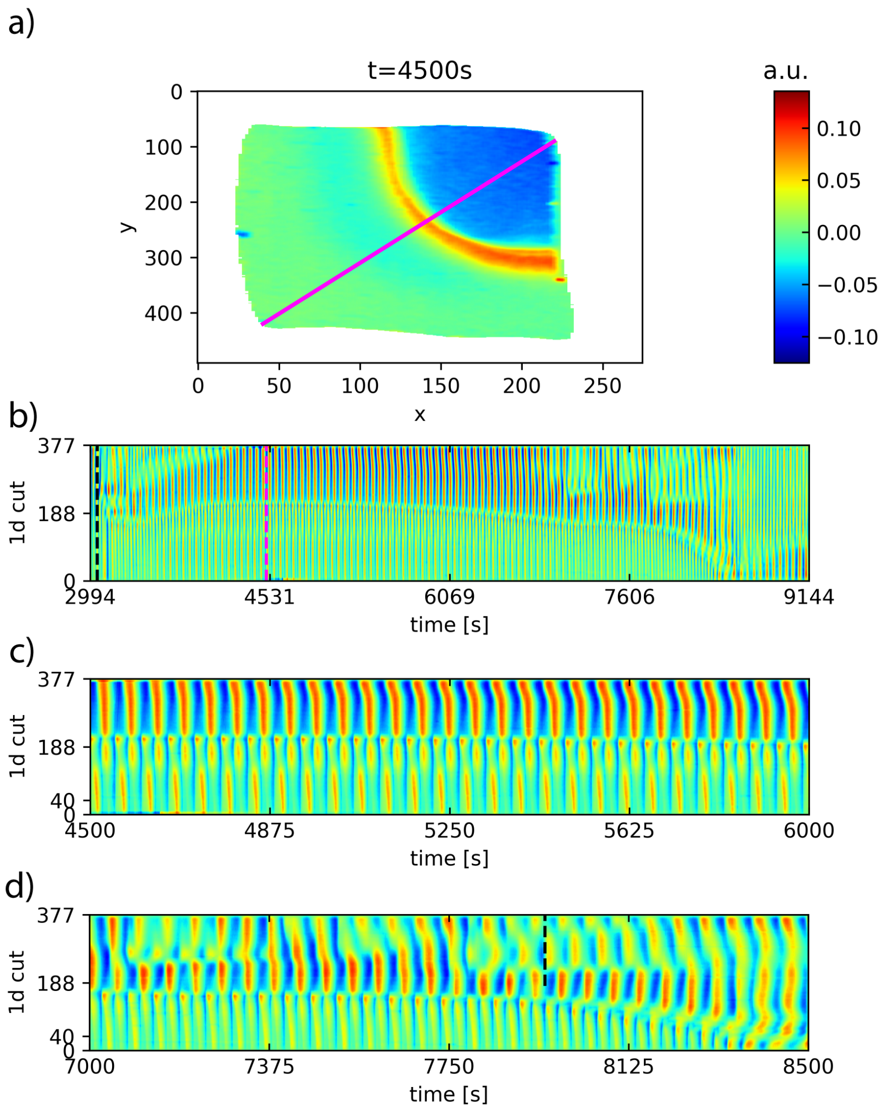

Figure 4.17: Spatial coexistence (SPACO) pattern measured with an n-doped WE after heterogeneously illuminating the rightmost 1/3 of the WE at an illumination intensity of 3.62 mW/cm^2 for 60 s while keeping the other 2/3 under a constant illumination intensity of 1.1 mW/cm^2. The applied voltage was U_{app}=5.65 V vs. SHE, and the product of the external resistor and the WE area yielded $R_{ext}A$=5 kΩcm^2. After the perturbation, the illumination intensity was kept constant and homogeneous at 1.1 mW/cm^2. a) is the snapshot of the WE taken at 4500 s, the magenta coloured line marks the 1D spatiotemporal cut depicted in b). The dashed black line in b) marks the point from which the perturbation stopped and the illumination was homogeneous and the magenta coloured dashed line marks the time of the snap shot. c) is the zoom into the spatiotemporal cut between 4500 s and 6000 s. d) is the zoom into the spatiotemporal cut between 7000 s and 8500 s.

Fig.4.17 d) depicts a zoom into the time range of the time series of the 1D spatiotemporal cut, when the spreading of the LAO region suddenly accelerates and spreads over the entire WE. In the cut one can see that episodes of antiphase clusters and LAPAs seem to appear in the LAOs region, in the upper part of the cut. The other region of the WE still displays Type II HAPAs, however, it seems that the period-two character, or in other words the difference between the small and the large maximum, is less pronounced than it is in Fig.4.17 c). This seems to be especially true at the point when the acceleration of the border between the two regimes start, which is marked by the black dashed line. In order to take a closer look at the local dynamics in the Type II HAPA region, we have plotted the time series of pixel 40 of the 1D spatiotemporal cut in Fig.4.18. Fig.4.18 a) covers the same time range as in Fig.4.17 c) and Fig.4.18 b) the same as in Fig.4.17 d). The time series in Fig.4.18 a) shows a relatively uniform period-two oscillation. The difference between the large maxima and the small ones is comparable high. In the local time series depicted in Fig.4.18 b) the oscillations are not as uniform as in a), but change in time. In the beginning, the period-two character is still quite pronounced, but the difference between the large and the small maxima is less than in Fig.4.18 a). By the time marked by the red dashed line, which is the same time as the black dashed line in Fig.4.17 d), the period-two character is only slightly visible and continues to decrease until the dynamics undergo a transition to an LAO state. When looking at the 1D time series of the spatiotemporal cut in Fig.4.17 b), one notices that the overall behaviour is reminiscent to DOMES state depicted in Fig.4.14, as there is a part of the electrode in an LAO state which spreads over the entire WE. The most prominent difference is clearly the long period of time in which the front between the LAO region and the Type II HAPA region is almost stationary in Fig.4.17 compared to the case of the DOMES where the LAO regions spread over the electrode within a comparable short amount of time. It is noteworthy that the HAOs region in the DOMES state does not show any kind of period-two behaviour or cluster formation and that the period-two behaviour in Fig.4.17 is distinctly less pronounced when the LAOs region spreads fast, compared to the time the border appears to be stationary. This could suggest that the state of spatial coexistence is stabilised by the coupling between the two phases, which seems to lock the LAOs to half of the main frequency of the HAOs and induces a period-two behaviour in the region exhibiting an HAO state. And as the period-two behaviour in the region exhibiting Type II HAPAs becomes less pronounced the region exhibiting LAOs starts spreading.

Stich et al. found, in numerical studies on a birhythmic reaction-diffusion medium, self organised pacemakers in the form of two spatially separated coexisting oscillatory regions, where each region attains a different limit cycle. In his case the size of the core of the region with a higher frequency could be destabilised by phase slips, which occur if the frequency difference between the two regions is increased above a critical value [90]. Maybe in the case depicted in Fig.4.17, the period-two behaviour of the region displaying an HAO state and the 1:2 locking of the LAOs to the main freuency of the HAOs reduces the frequency difference sufficiently, such that the front can be stabilised. The fact that in our case it is the slowly oscillating region which spreads throughout the system might point towards a negative dispersion relation, which is discussed in [91]. Nevertheless one must be careful to compare our results to the ones in [90], as Stich et al. investigated a reaction-diffusion system with local coupling, whereas we have a global and a nonlocal coupling. Furthermore the investigations of the self-organised pacemakers by Stich et al. have been in the Benjamin-Feir stable regime, whereas in our case we expect to be in the Benjamin-Feir unstable regime, at least for the LAPAs. Fig.4.19 depicts the time series of the current density and the spatial average of the ellipsometric signal during the same time interval as in Fig.4.17 c). In the time series of the current density in Fig.4.19 a) the oscillations show clear period-two behaviour, where the current maxima, which follow the low current minima show the typical behaviour of cut off HAOs, with the sharp overshoot in the beginning of the current plateau. The consecutive maxima, on the other Hand, do not seem to be affected by the illumination limit as they exceed the current of the plateau and seem to be of normal shape as it does not display any signs of a sharp current limit. The time

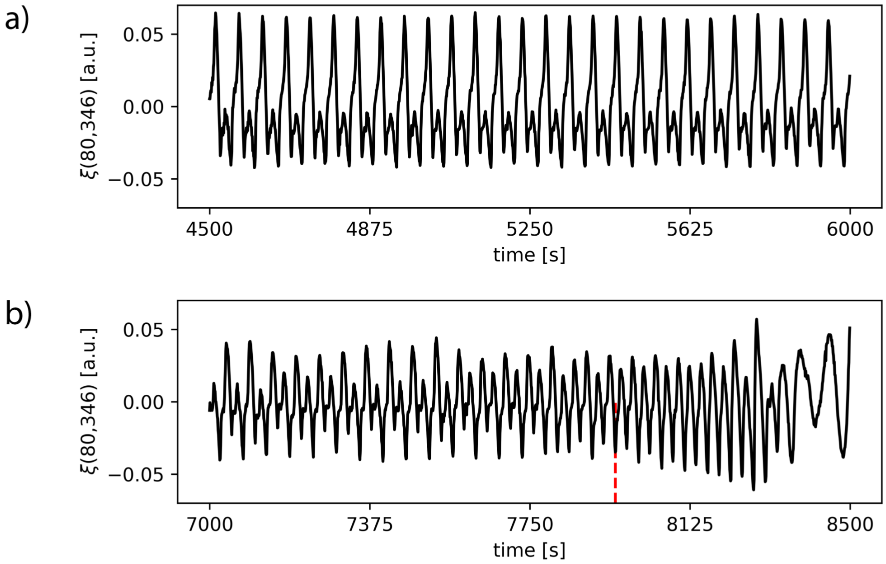

Figure 4.18: Local time series of ξ of the state depicted in Fig.4.17 at $(x, y) = (80, 346)$ which is pixel 40 in the 1D-cut for two different time intervals of Fig.4.17 c) and d). Measured with an n-doped WE at U_{app} =5.65 V vs. SHE, R_{ext}A=5 kΩcm^2 and an illumination intensity of 1.1mW/cm^2.

series of the spatial average of ξ, depicted in Fig.4.19 b) also displays a clear period-two behaviour. The low minima of ξ coincide with the spikes of the current in the maxima of the periods with the typical HAOs characteristics.

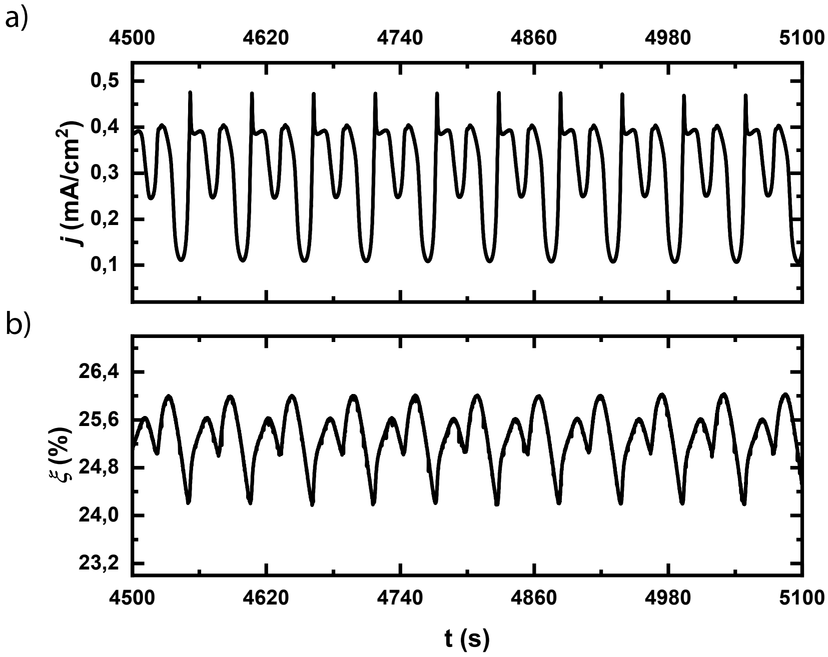

Figure 4.19: Time series of the global signals during the SPACO pattern depicted in Fig.4.17. a) the current density and b) the spatial average of ξ. Measured with an n-doped WE at U_{app} =5.65 V vs. SHE, $R_{ext}A$=5 kΩcm^2 and an illumination intensity of 1.1mW/cm^2.

In general the state depicted in Fig.4.17 c) is a very interesting state as it displays the spatial coexistence of LAO and HAO dynamics on one WE. Henceforth we refer to this state as 'spatial coexistence' (SPACO) state.

4.3 THE PATTERNS IN PARAMETERSPACE

In the last section we presented an example of each of the different types of spatiotemporal dynamics found in the investigated parameter regime during the electrodissolution of n-doped silicon. In this section we will try to relate the different types of spatiotemporal phenomena to the applied parameters to get a better understanding of the system and especially the effect of the different couplings on the dynamics. Thereby we keep in mind that we suspect the external resistor to couple the two limit cycles with each other and thus creating complex temporal behaviour but at the same time having a homogenising effect on the spatial dynamics. We also remember that reducing the illumination intensity below a certain value is necessary for spatial symmetry breaking to occur. As mentioned above we explored the parameter space using different techniques of initialisation and many different parameter sets. Slow potential scans for different combinations of illumination intensities and $R_{ext}A$ values turned out to give most insights into the dynamics and their relation to a given set of parameters. By scanning up and down between 4.65 V vs. SHE and 8.15 V vs. SHE, we could detect the LAOs, the HAOs and the transitions from one type of oscillations to another as well as a possible hysteretic behaviour for several different sets of parameters. The slow scan rate of either 0.3 mV/s or 0.1 mV/s ensured that the experiments were conducted close to quasi-stationary conditions such that we screened, at least qualitatively, a complete picture of the dynamics.

	1.0 kΩcm^2	3.0 kΩcm^2	6.0 kΩcm^2
2.25 mW/cm^2	Type I HAPA		- - -
1.20 mW/cm^2		LAPA DOMES SPACO	LAPA SPACO Type II HAPA
0.95 mW/cm^2		LAPA Type II HAPA	LAPA Type II HAPA

Table 4.1: The different patterns encountered during the different scans. Note that the scan with an illumination intensity of 1.2 mW/cm^2 and $R_{ext}A$=3 kΩcm^2 was scanned with 0.1 mV/s whereas all the others were scanned at 0.3 mV/s. The scan at 2.25 mW/cm^2 and $R_{ext}A$=1 kΩcm^2 was scanned from 8.15 V vs. SHE down to 4.65 V vs. SHE and was initialised in an HAOs state, whereas all the other scans started at 4.65 V vs. SHE in an LAOs state and were scanned up to 8.15 V vs. SHE and back down.

In Table 4.1 we listed the different types of patterns encountered during the different scans. So far no scans have been conducted for the parameter sets of the empty cells. For the measurements in the first row with the highest illumination of 2.25 mW/cm^2 the variety of the different spatial phenomena is the smallest. The measurement measured with an external resistor of 6.0 kΩcm^2 shows exclusively homogeneous dynamics and the one measured with an external resistor of 1.0 kΩcm^2 shows only the Type I HAPA and the checkerboard pattern The latter is transient behaviour observed during and right after the transition from an HAOs state to an LAOs state and, thus, it is qualitatively different from the other patterns which are stable states. The Type I HAPAs can be observed during cut off HAOs with no or low applied external resistance and high applied voltages.

The two measurements in the second row of Table 4.1 , measured at an intermediate illumination intensity of 1.20 mW/cm^2 show the most variety of spatiotemporal phenomena as they show all the above presented spatiotemporal features except for the Type I HAPAs. However the scan measured with an $R_{ext}A$ value of 3 kΩcm^2 is the only low illuminated scan which did not exhibit Type II HAPAs. Note that these two scans are the only ones which displayed the patterns of mixed dynamics, i.e. the SPACOs and the DOMESs, where the scan with an resistance of 3.0 kΩcm^2 showed both types and the one with the higher resistance of 6.0 kΩcm^2 only showed the SPACO state.

The scans in the last row measured at the lowest illumination intensity of 0.95 mW/cm^2 and resistances yielding 3.0 kΩcm^2 and 6.0 kΩcm^2 show the typical patterns emerging from the two oscillation types , i.e. the LAPAs and Type II HAPAs.

Table 4.1 gives a nice overview on which patterns can be found for which sets of parameters but it does not illustrate our claims concerning the effect of the two types of couplings, i.e. the linear global coupling introduced by the external resistor and the nonlinear nonlocal coupling introduced by the limitation of the amount of photo generated charge carriers. The latter is thought to decrease spatial coherence, whereas the global coupling introduced by the external resistor on the one hand has an homogenising effect on the dynamics but on the other hand introduces a temporal complexity by coupling the two existing oscillation mechanisms, i.e. the LAO and HAO, to each other as discussed in chapter 3.

4.3.1 *The Coupling Types and Spatial Complexity*

Let us first investigate the effect of the two parameters on the spatial synchrony of the phase. A good way to do that is to look at Kuramoto's order parameter S which is defined as follows [47]:

$$S(t) = \left| \frac{1}{N} \sum_{n=1}^{N} e^{i\Phi_n(t)} \right| \tag{4.2}$$

Here, N is the number of oscillators in the system, in our case all the pixels which map the active WE area, and $\Phi_n(t)$ is the phase of the nth oscillator. Note that the phase is obtained from the analytic signal as described in section 2.3.2. We determined the order parameter S for measurements during which the voltage was slowly scanned to detect spatial inhomogeneities. The type of these inhomogeneities could then be identified by looking at the video material and the 1D spatiotemporal cuts. S is a good measure for the synchrony of the phase dynamics and has proven to work best as a measure for the coherence of LAO states, i.e. the LAPAs, which are dominated by wave dynamics. In the case of Type I HAPAs which display inhomogeneities in the amplitude but have rather coherent phases the above defined order parameter is not the right tool to measure spatial coherence. But since in this measurement series, the Type I HAPA was only observed with an external resistor yielding a $R_{ext}A$ value of 1.0 kΩcm^2, we will restrict our discussion of the coherence to the phase dynamics, and thus to S. For a detailed analysis of the synchrony of clusters, which is the case for the Type II HAPAs, one would use the Daido-Kuramoto order parameter instead of Kuramoto's phase order parameter. Nevertheless, although Kuramoto's phase order parameter is certainly not the optimal tool for a quantitative analysis on the spatial behaviour of Type II HAPAs, it is definitely sufficient to detect the patterns which can then be further analysed separately. In this context, we use the order parameter to discuss the coherence of the phase dynamics on the WE and to point out the parameter values at which the individual attractors, transitions and patterns exist in the scan, in a hopefully clearer manner than walking the reader through hundreds of thousands of seconds of spatiotemporal cuts.

In order to illustrate the parameter dependence of the coherence of the dynamics, we plotted the order parameter of some of the scans of Table 4.1 in Fig.4.20. The plots are arranged such that the ones on the right side, in column II, are measured with large external resistor with 6 $k\Omega cm^2$ and the one on the left side, in column I, with only 3 $k\Omega cm^2$. The highest illumination was applied during the scan depicted in row a) and the lowest illumination during the one depicted in row c). All the scans, for which the order parameters are depicted in Fig.4.20 were initialised at low applied potentials in an LAO state. The potential was then slowly swept to a relatively high applied potential in the forward scan, during which a transition from an LAO state to an HAO state occurred. On the backward scan the system eventually goes back to an LAO state. Usually we observed a hystereses between LAO and HAO states, which means there are potential ranges in which the LAO and HAO states are bistable. We highlighted these bistable regions in red. Hence, the borders of the potential ranges for which the system is bistable also mark the transitions between the different types of dynamics. The high potential border is at the potential at which the dynamics change from an LAO state to an HAO state during the forward scan and vice versa.

A first rough comparison of the three curves in column II shows that, overall, the highest order parameter is reached during the scan depicted in a) II, which is constant at 1, as no pattern formation can be observed for these parameters. As we reduce the illumination intensity, the synchrony of the WE is reduced as well, which can be seen at the decreasing minimal values of the the order parameters depicted in b) II and c) II. Comparing the order parameter in b) I, which was measured with a lower external resistance of 3 $k\Omega cm^2$, with the one measured with the higher resistance in b) II, one sees that the overall order parameter is less noisy and higher for the one with the larger external resistance. The increased coherence observed for the larger external resistance is due to the homogenising effect of the linear global coupling introduced by the resistor.

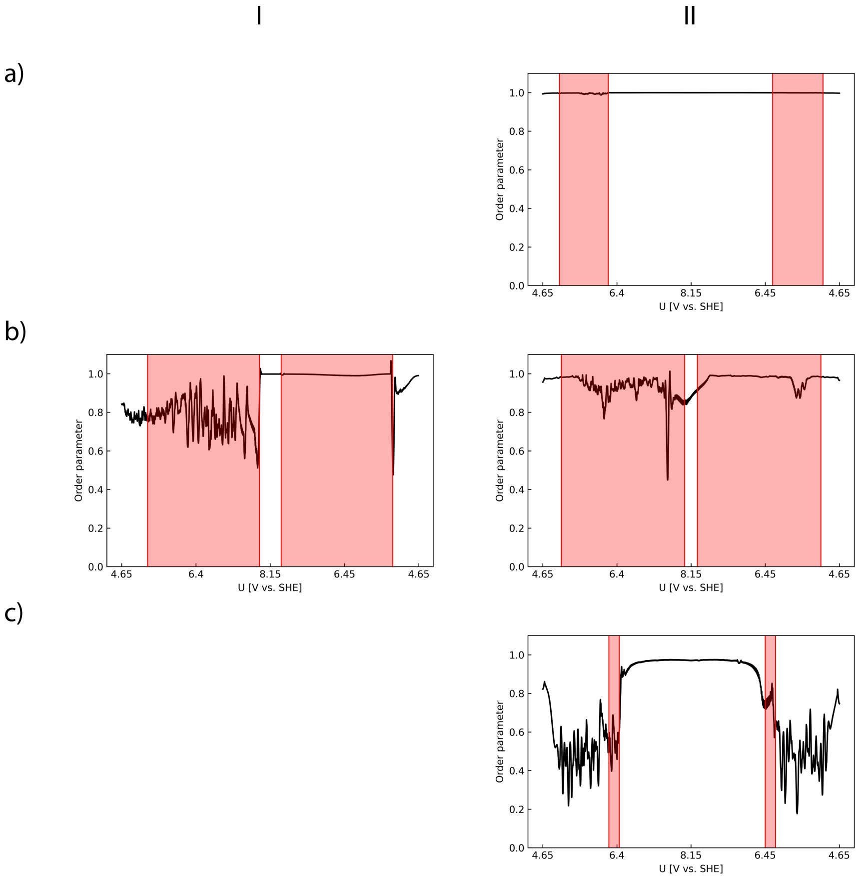

Figure 4.20: Kuramoto's phase order parameters of oscillations during slow CVs. The scan in column I was conducted with an external resistance of 3 kΩcm^2 and the scans in column II with 6 kΩcm^2. In row a) the WE was illuminated with 2.25 mW/cm^2, in b) the WEs were illuminated with 1.20 mW/cm^2 and in c) with 0.95 mW/cm^2. The red areas mark the regions for which the system displayed a hysteresis. The order parameters were smoothed using a Savitzky-Golay filter with a 2nd degree polynomial and a 301 point window.

We now take a closer look at the curves in in Fig.4.20 column II and connect the features in the order parameters with the different dynamical states and spatiotemporal patterns presented above. We start with the scan in Fig.4.20 c) II, which is the one with the lowest illumination. In the beginning of the scan the order parameter starts at a relatively high value, slightly above 0.8, as the system attained an LAO state during which some LAPAs begin to form. As we follow the curve towards slightly higher potentials we observe a significant decrease of the order parameter together with an increase of its noise. Here we have fully developed unordered LAPAs similiar to those presented in Fig.4.4. The order parameter stays low and noisy until it suddenly increases to a high value around 0.9, as the dynamics changes to the HAPA II state depicted in Fig.4.9. As the scan proceeds to higher potentials the Type II HAPA disappears and the system performs homogenous HAOs which lead to a constant order parameter at roughly 1. On the backward scan the order parameter drops down to values between 0.8 and 0.9 in the bistable region, as again Type II HAPA form on the WE. A further decrease of the potential leads to a transition from Type II HAPA to LAPA, which manifests itself in a sudden decrease of the order parameter and increase of its fluctuations. For the low potentials at the end of the scan, the LAPA state becomes more coherent again, which leads to an increase in the order parameter.

We now take a look at the order parameter depicted in Fig.4.20 b) II. In the beginning of the scan the order parameter is close to 1 with almost no fluctuations, indicating homogenous LAOs. As the potential is increased the order parameter decreases slightly and becomes a little noisy. Here, the dynamic on the WE desynchronises slightly as some LAPAs start to form in the bistable region of the scan. At the high potential border of the bistable regime the dynamics change from LAPA to SPACO. The transition from the SPACO state to homogenous HAOs is rather slow in this case, and it seems as if the transition does not occur until the backward scan, which can be seen by the slowly growing order parameter. However, we defined the local minimum of the order parameter in the SPACO state as the transition point to the HAOs, as it marks the point for which the area of the LAO region on the WE starts to shrink in favour for the HAO region. It seems as this is the point where the LAO phase becomes unstable and disappears slowly. As the order parameter reaches one, the system exhibits homogenous HAOs. On the backward scan, within the low potential region of the bistable regime where the order parameter decreases, we find the Type II HAPA state depicted in Fig.4.12. After this Type II HAPA pattern disappears, the dynamics change from homogenous HAOs to LAOS. During the scan depicted in Fig.4.20 a) II the oscillations were spatially homogenous, thus, the order parameter is constant at 1.

The order parameter of the scan depicted in Fig.4.20 b) I was measured with the same illumination intensity as the one in Fig.4.20 b) II, but with a smaller resistance. It begins at roughly 0.8, as the WE exhibits LAPAs. Upon an increase of the potential the order parameter decreases slightly, until it reaches the bistable regime. Within the bistable regime, suddenly, large spikes to values of almost 1 arise followed by large drops of the order parameter to values of around 0.6. This behaviour associated with DOMES dynamics similar to the ones depicted in Fig.4.14. Note that the high spikes depict moments of very high synchrony in the system and are related to the phase of the DOMES state in which the system abruptly jumps to homogeneous HAOs, right after the LAO state sufficiently synchronised, and before a new nucleus of the LAOs state has formed. At the end of the bistable region in the forward scan one recognizes two almost identical features consisting of a spike in the order parameter which reaches up to values above 0.9 followed by a gradual decrease towards roughly 0.6 and then again a sudden spike up to 0.9 and a subsequent gradual decrease towards approximately 0.5 before the order parameter abruptly jumps up to a value close to 1. These features are related to SPACO states similar to the one depicted in Fig.4.17. The spike in the order parameter is, analogously to the above described synchronous phase in the DOMES, associated with periods of coherent HAOs. The subsequent decrease of the order parameter is related to a nucleus of LAOs, which forms and spreads over the WE. However in contrast to the DOMES state, the spreading of the LAOS during SPACOs happens much slower, thus we see the gradual decrease in the smoothed order parameter. Subsequent to the SPACO state, the system attains a homogenous HAO state, which is associated with the large value of the order parameter. It continues to exhibit homogenous HAOs in the backward scan, until the dynamics changes back to LAPAs at the low potential border of the bistable potential range. Towards the end of the scan the WE becomes more homogeneous, until it exhibits homogenous LAOs, which can be seen as the order parameter approaches 1.

The comparison of the order parameters in Fig.4.20, shows that we have homogenous oscillations if the WE is sufficiently high illuminated, and that the spatial synchrony decreases with decreasing illumination intensity. It also demonstrates the homogenising effect of the linear global coupling introduced by the external resistor, as can be seen by the overall higher order parameter for the scan with higher external resistance in Fig.4.20 b) II compared to the one with smaller external resistance in Fig.4.20 b) I.

4.3.2 *The Effect of the External Resistor on the Current*

Fig.4.21 depicts two spectrograms of the currents during two scans measured with an illumination intensity high enough, such that no stable spatiotemporal pattern formed on the WE, except for Type I HAPAs. One scan was measured at $1.0\,\mathrm{k\Omega cm^2}$ and one at $6\,\mathrm{k\Omega cm^2}$. Note that for the scan with the low applied resistance of $1.0\,\mathrm{k\Omega cm^2}$ we inverted the scan direction and scanned from 8.15 V vs. SHE to 4.65 V vs. SHE and back. This was done since the system would not bifurcate from the LAOs into the HAOs for the given range of parameters. Hence we first initialised the HAOs and scanned from there into the LAOs region. For these parameters the only pattern the system displays are the Type I HAPA presented in Fig.4.7 and the checkerboard pattern. The latter is usually observed during the transition from an HAOs state to an LAOs state if the oscillation maxima of the HAOs are cut off by the reduced illumination. At this illumination intensity the scan with $1\,\mathrm{k\Omega cm^2}$ was the only one showing spatial symmetry breaking. We highlighted the changes from HAO to LAO dynamics and vice versa with vertical red lines. In addition we labelled the bistable regions of the scan, as well as the potential regions where only HAOs or LAOs could be found, respectively.

Fig.4.21 a) shows a spectrogram of the scan with low external resistance, which was initialised in Type I HAPAs at high potentials, which soon vanish in favour for spatially homogenous HAOs. It can be seen that the main frequency of the HAO state, which is the bright yellow band, starts roughly at 20 mHz and increases almost linearly to approximately 30 mHz at 6.25 V vs. SHE. The spectrum has relatively low background and except for the second harmonic it has no other active frequency bands which indicates that the system exhibits periodic oscillations. At roughly 6.25 V vs. SHE the oscillations change from HAOs to LAOs, which can be seen in the spectrogram, as the main frequency abruptly jumps to half its value. That it drops to half its previous frequency becomes especially clear as we look at the second harmonic of the LAOs, which seems to be a continuation of the main frequency of the HAO. In addition to the second harmonic of the LAOs the spectrogram also shows their third and later in the scan also their forth harmonic. As we approach the minimum potential of the scan, i.e. the turning point of the CV, the main frequency approaches its maximum. After the turning point the frequency is symmetric to the forward scan up to the potential, highlighted by the red line, at which the dynamics changed from HAOs to LAOs in the forward scan. On the backward scan the system stays on the LAO limit cycle with the lower frequency, thus exhibiting a hysteresis. We labelled the potential range of the hysteresis as 'bistable'. By the end of the scan, a non-periodic episode emerges in the current signal. A part of the time series of the current density during this episode is depicted in Fig.4.22. In the spectrogram this non-periodic behaviour shows itself as a drastic increase of the background. As a result the main frequency and the higher harmonics are not clearly visible any more. Apart from this non-periodic episode at the end, the system displays periodic behaviour throughout the scan, which brings us directly to the other spectrogram, measured with a comparably high external resistance, which shows all kinds of complex behaviour.

Fig.4.21 b) depicts the spectrogram of the current during the scan with high illumination intensity and a high external resistance of 6.0 kΩcm^2. During the entire scan, no spatial symmetry breaking was observed. Note that this CV started at 4.65 V vs. SHE exhibiting LAOs. At the beginning of the scan we see basically just one active frequency band without much noise or background which is an indication for periodic oscillations. The main frequency starts above 40 mHz and drops comparably fast down to almost 30 mHz, where the spectrogram develops a strong background such that one cannot identify a main frequency. In the potential range where the background is high, the current oscillations deviate from periodic LAOs and become more complex. A part of the time series during this complex behaviour is exemplary depicted in Fig.4.23. Despite the high background in the spectrogram, one can recognise some lines which follow roughly the slope of the main frequency the LAOs had before becoming complex. This makes it seem as if the overall frequency of the oscillations is still decreasing with increasing potential. The second red line from the left highlights the potential at which the dynamics change from a non-periodic LAO state into periodic HAOs, which can be seen at the transition from the blurry region in the spectrogram to a region with a distinct main frequency and relatively low background. The two relatively thick vertical stripes in the HAOs region are artefacts resulting from a brief interruption of the data recording. The main frequency of the HAOs also decreases with increasing potential. At higher applied voltages also the second harmonic of the HAOs becomes visible. On the backward scan as the applied potential decreases the oscillation frequency increases and is at first symmetric to the forward scan. This symmetry is broken as the dynamics do not change into an LAO state at the third red line from the left, which highlights the potential at which the system changed from an LAO to an HAO state in the forward scan. Hence, also in this scan the system shows hysteretic behaviour. In the bistable region during the backward scan, the HAOs seem to show a period-two behaviour as depicted in Fig.4.24, which leads to the emergence of the subharmonic frequency in the spectrogram. Close to the end of the CV the subharmonic frequency vanishes and the main frequency drops from approximately 40 mHz to some value slightly below 40 mHz as the dynamics change from the HAO state to periodic LAOs.

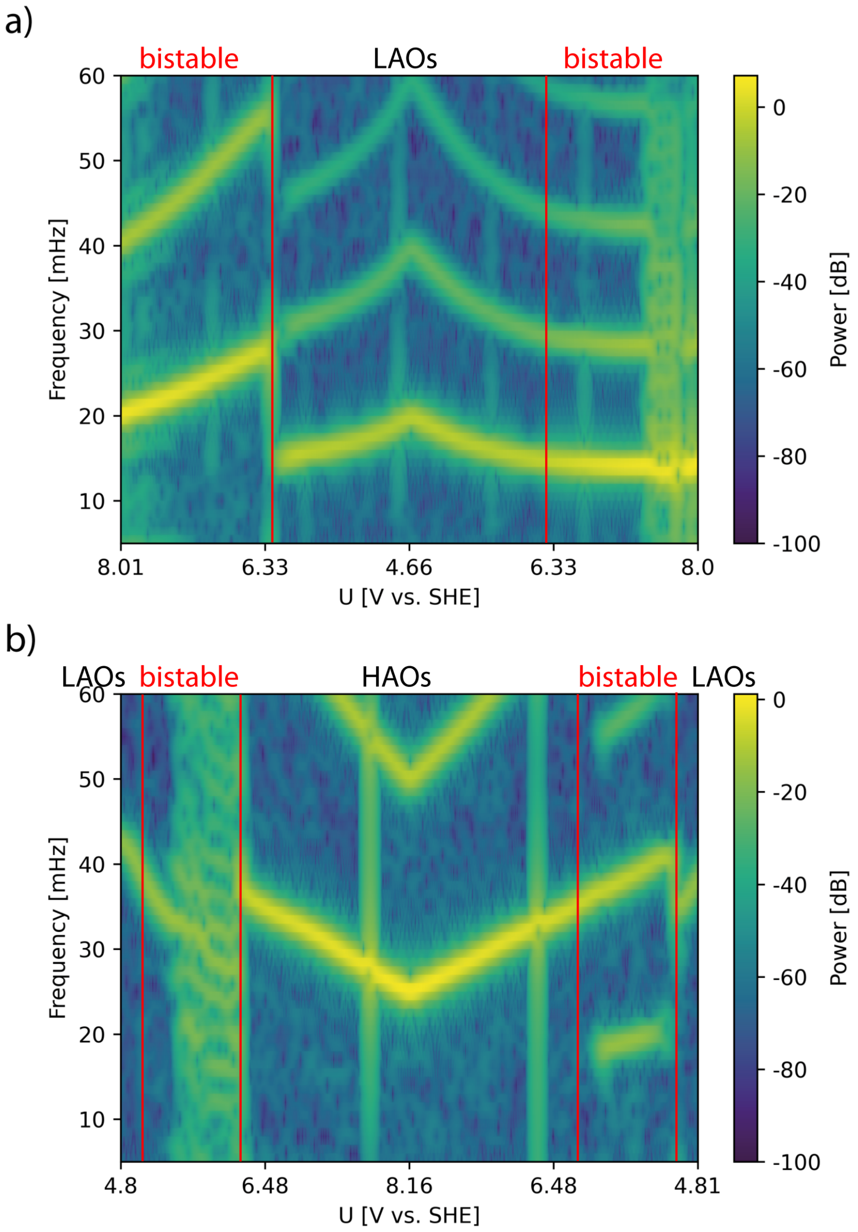

Figure 4.21: Spectrograms of the current during voltage scans with a scan rate of 0.3 mV/s and an illumination intensity of 2.25 mW/cm^2. In a) HAOs were initialised and the voltage was scanned from 8.15 V vs. SHE to 4.65 V vs. SHE and back up, with an applied resistance yielding 1 kΩcm^2. In b) LAOs were initialised and the voltage was scanned from 4.65 V vs. SHE up to 8.15 V vs. SHE and back with an external resistor yielding 6 kΩcm^2. The red lines mark the potentials under which the qualitative behaviour of the system changed from an LAO into an HAO state or vice versa.

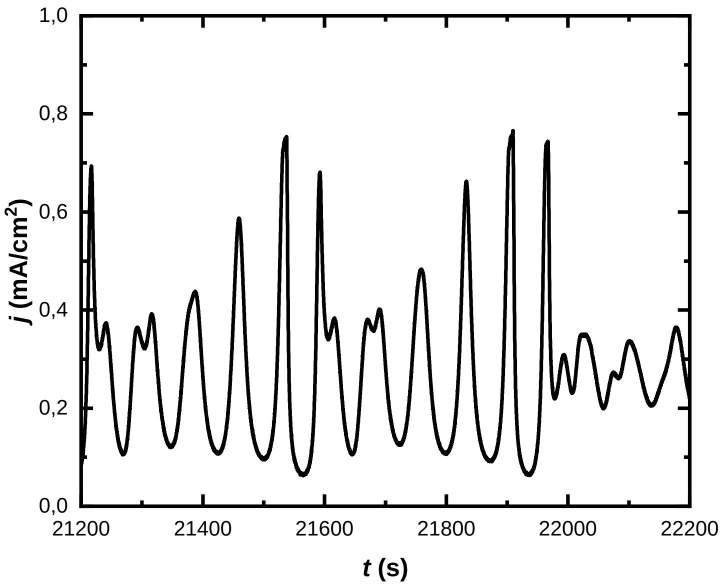

Figure 4.22: Current density of LAO state in bistable region during forward scan. Spectrogram of the scan depicted in Fig.4.21 a) Illumination intensity 2.25 mW/cm^2, $R_{ext}A$=1 kΩcm^2, U_{app} =5.70-5.82 V vs. SHE.

Note that the non-periodic LAO state depicted in Fig.4.23, as well as the period-two HAO state depicted in Fig.4.24, are both reminiscent of the complex states presented in chapter 3. Both were measured during the scan with the large external resistance, depicted in Fig.4.21 b). Similar to the bistability we presented in the case of p-doped Si WEs, the complex dynamics emerge in the potential range of the hysteresis. The potential range for which the system shows a bistability of complex temporal behaviour, separates the ranges in which we find only periodic LAOs from the one where we only find periodic HAOs. We find period-two behaviour when we enter the bistable region from the HAOs and a seemingly chaotic LAO state if we enter the bistable region from the LAOs side. We therefore believe, that the bistability detected during the scan in Fig.4.21 b) is of the same nature as the one presented in chapter 3. Hence, this is another strong indication that the oscillatory electrodissolution of n-doped Si and p-doped Si exhibit similar dynamics, if the n-doped WE is illuminated with a sufficiently high intensity. In the case of the scan in Fig.4.21 a), where we initialised an HAO state with an external resistance of only 1 kΩcm^2 the maxima of the current density oscillations during this state were cut off, despite the high illumination intensity. This can be seen in Fig.4.6, as this was the state measured at the starting point of the CV from Fig.4.21 a). The cut off current oscillations made it possible to stabilise the HAO state for such a low external resistance and gave us the opportunity to further investigate the effect of the external resistor on the behaviour of the dynamics. As during both of the scans no patterns were observed which influenced the current signal, all the features can be related to the global behaviour of the system. The low background in the spectrogram, as well as the lack of subharmonics shows, that the dynamics during the scan with the low external resistance is for most parts periodic. This means that the system attains either the LAO limit cycle or the HAO limit cycle and undergoes unperturbed, periodic oscillations. Only in the end of the scan the dynamics in the LAO state deviate from periodic behaviour, which might indicate that a bistable parameter region where the dynamics display complex oscillations can be reached for very high potentials, despite a low external resistance. To clarify if this is true one would need to do more measurement at even higher potentials than 8.15 V vs. SHE.

As we compare both spectrograms, we obtain the impression that the external resistance introduces a complexity in the time series of the current density in a similar way as we have observed it in chapter 3 for p-Si electrodes. We believe that the complex behaviour of the global signals, such as the current density, is due to an intrinsic coupling of the two coexisting limit cycles. Furthermore, it seems that the external resistance plays an important role for this type of coupling. However the non-periodic episode in the end of the scan depicted in Fig.4.21 a) could suggest that for large enough applied potentials a mutual influence of the two limit cycles on each other can be triggered, even for small external resistors. These results point, similarly to the results from chapter 3, towards an effect of the external resistor on the reaction term of the system. As we have merely homogenous dynamics during the scan depicted in Fig.4.21 b) and during most of the scan depicted in Fig.4.21 a), for which we can consider the homogenising coupling term, introduced by the external resistor according to Eq. 3.1, to be zero. Instead the external resistor seems to have an effect on the reaction term of the system like we have implied in Eq. 3.2.

We think that the main frequency of the oscillations depends on or is at least largely influenced by the thickness of the oxide layer. It is interesting that independently of the measurement or the attractor, the main frequency decreases with increasing anodic polarisation. To show the possible correlation between frequency and oxide layer thickness we first take a look at the correlation of the oxide layer thickness and the applied voltage. Fig.4.25 shows the spatial average of the ellipsometric signal for an n-doped Si WE during a CV between 0.65 V vs. SHE and 6.65 V vs. SHE conducted with a scan rate of 20 mV/s and zero external resistance. The arrows indicate the scan direction.

Note that changes in the ellipsometric signal measure relative changes of the optical pathway which include changes of the physical pathway as well as changes of the refractive index. In the beginning of the scan, in the voltage range of the electropolishing branch, the

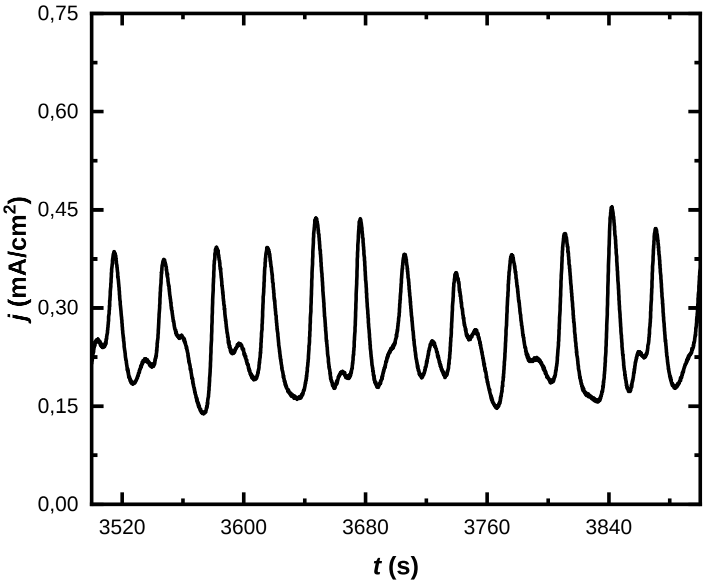

Figure 4.23: Current density of an LAO state in the bistable region during a forward scan. Measured from U_{app} =5.70 V vs. SHE to 5.82 V vs. SHE. Spectrogram of the scan depicted in Fig.4.21 b). Illumination intensity 2.25 mW/cm^2, $R_{ext}A$=6 kΩcm^2

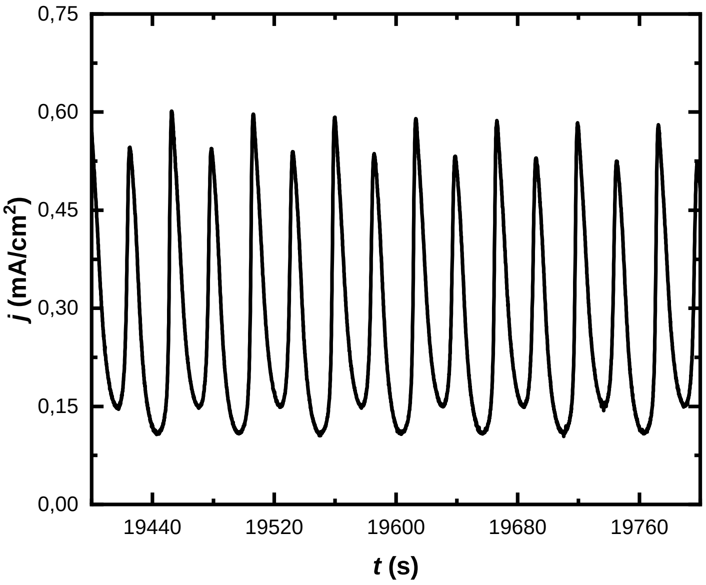

Figure 4.24: Current density of HAO state in bistable region during backward scan. Spectrogram of the scan depicted in Fig.4.21 b). Illumination intensity 2.25 mW/cm^2, $R_{ext}A$=6 kΩcm^2, U_{app} =5.82-5.70 V vs. SHE.

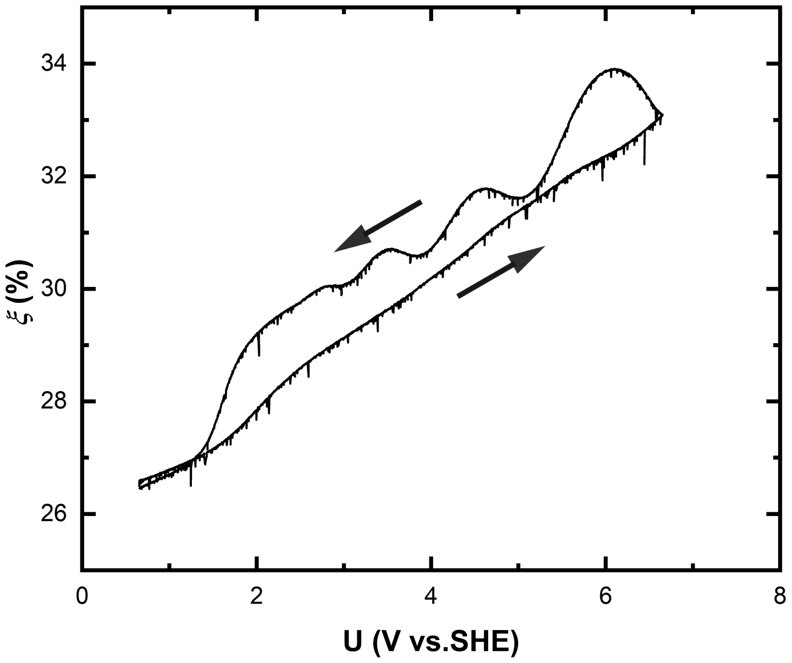

Figure 4.25: The spatial average of the ellipsometric signal vs. U_{app} during a CV measured at a scan rate of 20 mV/s with no external resistor.

ellipsometric signal increases slightly, although a stable oxide layer has not yet formed under these conditions. Hence the increase of the ellipsometric signal is probably induced by changes of the refractive index. Note that short living oxide nuclei might have an impact on the refractive index in this voltage range [20]. The consecutive region, between roughly 1.6 V vs. SHE and 2.5 V vs. SHE, in which the ellipsometric signal increases fast coincides with the NDR branch and can thus be related to the formation and growth of an oxide layer. The increase of the ellipsometric signal for higher applied voltages suggests strongly that the oxide layer thickness increases with the applied voltage, which is also in line with findings in the literature [10–12, 74, 82, 93].

Therefore we think that the decrease of the frequency with increasing applied voltage together with the increase of the oxide layer thickness with the applied voltage might hint towards a dependence of the oscillation frequency on the oxide layer thickness. Note that the frequencies in the spectrogram of the scan with 6 kΩcm^2 depicted in Fig.4.21 b) are overall higher than in the spectrogram of the scan measured with 3 kΩcm^2. Since the potential drop at the WE surface decreases with increasing external resistance, the oxide layer thickness at a given applied potential will also be smaller for a larger external resistance. Hence, that the overall frequencies in Fig.4.21 b) are higher than in Fig.4.21 a) is in line with the hypotheses that the frequency decreases with increasing oxide layer thickness.

Again we have shown a lot of evidences that the external resistor introduces a coupling between the two oscillation mechanisms and thereby introduces the temporal complexity to the system. We have seen that for a spatial symmetry breaking the illumination intensity must be reduced below a certain threshold. This threshold depends also on the applied voltage and the external resistance. Below the illumination threshold for pattern formation, a lower illumination intensity results in less coherent behaviour. The external resistance has a homogenising effect on the spatial dynamics but is also crucial for the Type II HAPAs to occur, as they are strongly connected to the higher periodic HAOs which are a result of the coupling induced by the external resistance. It also became clear that the nonlinear coupling induced by the reduced illumination can have an enhancing effect on the coupling mechanism introduced by the linear global coupling due to the external resistor. We could see this especially for the two scans with an external resistance of $3\,\mathrm{k}\Omega\mathrm{cm}^2$, where the higher periodic HAOs, i.e. the Type II HAPAs, could only be observed for the lower illuminated case. This shows that the influences of the low illumination and the external resistance cannot be clearly separated. In addition we showed a probable connection between the oxide layer thickness and the oscillation frequency.

4.4 DISCUSSION

4.4.1 *The Coupling Parameters*

Apart from the spatial heterogeneities it could be shown that the system will exhibit similar behaviour in the $R_{ext}A$-U_{app} parameter plane as in the p-doped case presented in chapter 3. The main difference to the p-doped case is, that, in the n-doped case, HAOs which are cut off due to a reduced illumination intensity, will reach much further into the low resistance side of the parameter plane. This also seems to enable birhythmicity as opposed to the bichaoticity observed with p-Si. As the generation rate of charge carriers becomes of the same order of magnitude as their consumption, the effective reaction resistance of the space charge layer increases and the potential drop across the space charge layer becomes significant for the local dynamics. As the amount of charge carries in the space charge layer is low, lateral motion of the charge carrier density becomes possible and depends on the local charge carrier concentration and the local potential drop across the space charge layer. The latter, in turn, depends on the potential drop across the external resistor, and thus, the global current, as well as the potential drop through the oxide layer [64, 67]. We have demonstrated, that the reduction of the illumination intensity not only enables the formation of spatiotemporal patterns, but also that the coherence of these patterns decreases with decreasing illumination intensity. This effect is especially noticeable for LAPAs. The increased reaction resistance in the space charge layer might also play a significant role for the stabilisation of the HAOs at zero external resistances, as it might compensate for the lack of external resistance. Note that we showed in chapter 3 that a sufficient external resistance seems to be crucial for the stabilisation of HAOs.

An external resistor in series with the WE introduces a linear global coupling to the system, which acts homogenising on the dynamics. In addition it seems to have some significant influence on the reaction current. We could show that a sufficiently large external resistance leads to complex oscillations in the global signal. Since the coupling term of the linear global coupling is zero in the homogeneous case, and we see this behaviour also in the homogeneous case we conclude that there is some additional effect of the external resistor on the electrochemical reaction.

4.4.2 *Type II HAPAs and LAPAs*

Spatial symmetry breaking can be observed for both types of oscillations, i.e. the LAOs and the HAOs, however each type of oscillations displays its own characteristic type of spatiotemporal behaviour. LAOs develop LAPAs which are dominated by wave fronts moving across the electrode leading to a low degree of synchrony of the phase. For the LAPAs phase coherence increases with increasing applied external resistor which has an homogenising effect on the dynamics [64, 65, 101, 102].

The HAPAs are the patterns characteristic for the HAOs and can be divided into two types. The Type I HAPA is characterised by irregular heterogeneities in the amplitude but a rather coherent overall phase and is found especially for low applied external resistances and high voltages. The Type II HAPA also exhibits modulations of the amplitude, however they are found for higher resistances and the modulations arise as clusters in an antiphase configuration.

We introduced the TYPE II HAPAs as typical patterns which are formed in the HAO branch of the system for sufficiently low illumination and a sufficiently large external resistor. We characterised the patterns as cluster states, with a kind of period-two behaviour in the global signals. Especially with larger external resistors, cluster formation seems to be the most prominent spatial feature during HAOs states. The clustering only appears in, or close to the bistable region. In section 4.3.2 we explained that we believe that the hystereses measured during the slow potential scans with n-doped Si is qualitatively of the same nature like the bistability of the complex oscillations presented in chapter 3. With this in mind we want to take a closer look on where we have measured the Type II HAPA states from Fig.4.9 and Fig.4.12. The state depicted in Fig.4.9 has been measured right after the transition from the LAPAs to the HAO branch on the forward scan for which the Kuramoto phase order parameter is plotted in Fig.4.20 c) II. The state depicted in Fig.4.12, was measured towards the end of the bistable region in the backward scan of the CV for which the order parameter is depicted in Fig.4.20 b) II. The latter state shows more complexity, which can especially be seen at the period four behaviour in the local time series depicted in Fig.4.13. The trend that a rather simple period-two behaviour can be found on the HAO branch close to the onset of the bistable regime and that more complex HAO states can be detected within the bistable potential range close to the transition to LAO attractors is in line with the findings in chapter 3. It seems possible, that the complexity of the states in the n-doped case, especially in their global signals, is also introduced by the intrinsic coupling of the two limit cycles, like it is in the case of p-doped Si. The difference in the n-doped case at lower illuminations is that due to the nonlinear nonlocal coupling, pattern formation is possible. The reason why the HAO states especially tend to form antiphase pattern, might be the relaxational character of the HAOs. In [45], Kiss et al., predicted a strongest mutual entrainment of relaxational oscillators to be in antiphase configuration. They based their prediction on phase response curves, measured during the oscillatory electrodissolution of a single nickel electrode. Subsequently they confirmed their results experimentally with an ensemble of 64 coupled nickel electrodes, which formed two clusters in antiphase configuration for the parameters under which the oscillations have relaxational character. It seems likely that, in our system, the complexity, i.e. the deviation from simple periodic HAOs, is in the first place introduced by the intrinsic coupling of the two limit cycles, but the cluster formation is especially influenced by the relaxational character of the oscillations themselves.

No interaction between the limit cycles like described in 3.5 is necessary for the LAPAs to emerge, as they can also be found far from the onset of the bistable regime. We suggest the LAPAs to emerge as the system enters a parameter region for which it is Benjamin-Feir unstable.

4.5 CONCLUSION

We started this chapter by a presentation of the effect of the nonlinear nonlocal coupling, i.e. the reduction of the illumination intensity, on the behaviour of the system. We pointed out its similarities and differences to the linear global coupling by presenting illumination limited current-potential curves. We also showed that the structure of the emergence of the attractors within the U_{app}-R_{ext}-parameter plane under reduced illumination is similar to the one for p-doped silicon depicted in Fig.3.4, except that HAOs can also be stabilised down to zero external resistance in the n-doped case.

We continued to present the different kinds of patterns that we observed in the investigated parameter range. We pointed out that the spatiotemporal behaviour can also be classified as evolving either from LAOs or HAOs.

We presented the typical spatiotemporal behaviour during LAOs under reduced illumination as spatiotemporal chaos with travelling wave-like features on the WE and coined this state LAPA.

The typical pattern during HAOs with low applied external resistance and reduced illumination is a state dominated by amplitude turbulence with an approximately constant phase velocity, if averaged over several oscillations, but a distinct dependence of the local phase on the local amplitude. We called these patterns Type I HAPA. For larger applied external resistances we found HAOs with a higher periodicity in the global signals, which form clusters in antiphase correlation on the WE. We named these states Type II HAPA.

In addition to the pattern found while the system is dominated by one of the two oscillation types we presented also mixed dynamics. In the DOMES state the system alternates between an LAOs state and an HAOs state. This state showed the typical transition from HAOs to LAOs where a region exhibiting LAOs spreads further and further across the WE. This transition shows a characteristic checker board pattern in a 1D-cut. When the LAOs spread over the whole WE, the dynamics on the electrode starts synchronising before eventually it jumps back to HAOs. Then a new LAOs nucleus forms on the WE and the circle repeats. Hence, both, the LAO and the HAO states are metastable.

The SPACO state is a state where a region exhibiting a Type II HAPA coexist with a region displaying homogenous LAOs which are locked to half the main frequency of the region in the HAO state.

In the second part of this chapter we connected the different spatiotemporal phenomena with the control of the experimental parameters. Therefore we looked at slow voltage scans with different external resistances under different illumination intensities. We used the Kuramoto phase order parameter to show that the spatially synchrony overall decreases with decreasing illumination intensity. This effect is related to the nonlinear nonlocal coupling introduced by a lack of charge carriers in the space charge layer. We could also show that in the case of LAPAs and Type I HAPAs it increases with increasing external resistance. This is due to the homogenising effect of the linear global coupling introduced by the external resistor. In the case of the HAO dynamics we also showed that although the homogenising effect of the external resistor impedes Type I HAPAs, for the Type II HAPAs an adequate external resistance is needed to induce a temporal complexity in the dynamics which seems to be the pre-condition for this pattern. However, the cluster formation in this state is attributed to the relaxational character of the HAOs.

In the end of the chapter we used the spectrograms of a scan with an external resistance of $1\,\mathrm{k\Omega cm^2}$ and a scan with $6\,\mathrm{k\Omega cm^2}$ to further underpin the fact that the external resistor induces the temporal complexity into the system by coupling the two coexisting limit cycles with each other. This was unveiled by an overall simple periodic behaviour during the scan with lower external resistance and a relatively complex spectrum of the scan with larger external resistance. During the latter more or less the same dynamics as in chapter 3 were found. In the spectrogram this was displayed by a subharmonic frequency in the HAOs region and a high background during the LAOs, both in the coexistence region.

In addition we pointed out a possible inverse relation between the oxide layer thickness and the oscillation frequency.

5

SUMMARY AND OUTLOOK

The goal of this thesis was to elucidate various facets of birhythmicity in the oscillatory electrodissolution of silicon, as an example of a spatially extended reaction-diffusion type system. This is, to the best of our knowledge, the first experimental investigation of an spatially extended birhythmic system.

Our efforts can be split in two parts. In the first part we investigated p-doped silicon where we have the external resistance as only coupling parameter. In the second part we investigated n-doped silicon WEs where, apart from the linear global coupling via the resistor, we can also control the strength of a nonlocal nonlinear coupling via the reduction of the illumination intensity which can lead to pattern formation, as observed in the spatially resolved ellipsometric signal.

In the first part, we focused on the dynamics found during the electrodissolution of p-doped silicon. The external resistance R_{ext} introduces a linear global coupling, however, the coupling term of a linear global coupling becomes zero for spatially homogenous dynamics, as it is always the case for p-doped Si. Nevertheless, the external resistor has large influence on the dynamics of the system. We thus could demonstrate that in addition to the linear global coupling, it has to have an influence on the reaction term of the system.

We showed that the system displays two types of oscillations with different underlying mechanisms, so-called LAOs and HAOs. In the U_{app}-$R_{ext}A$ parameter plane the regions of the two distinct oscillations is separated by a region where two bistable branches, each displaying complex and even chaotic dynamics, can be found. The complex dynamics in each of the two branches can be related to one of the two oscillation types. The chaotic motions suggests that the dynamics live in an, at least, 3-dimensional phase space, as more than two essential variables are needed for chaotic oscillations.

We suggest that the bichaotic regime in parameter space arises as a result of an inherent birhythmicity in the system. As the two coexisting limit cycles come sufficiently close to each other in phase space, they influence each other via an intrinsic coupling through a shared oscillation variable. Later in this thesis we could show that $R_{ext}A$ seems to be the crucial quantity for the inherent coupling of the two limit cycles as the complex temporal dynamics only arise in the presence of a sufficiently large resistance inserted in the external circuit. We thus conclude that the shared variable involved in the intrinsic coupling, which renders the oscillations more complex, is the potential drop U_{el} across the WE. This type of inherent birhythmicity, which leads, via an intrinsic coupling, to two different, but coexisting routes into chaotic motion, is to the best to our knowledge unique compared to other birhythmic systems.

In the second part we focused on n-doped silicon where the WE needs to be illuminated to generate holes in the valence band which drive the oxidation process. We showed that the different spatiotemporal dynamics can be related to one of the two oscillation types found in the system. The LAOs exhibit patterns characterised by travelling wavefronts on the WE, irregular in shape, velocity and direction, thus, resulting in spatiotemporal chaos. We coined these patterns LAPAs. These patterns seem to result from a Benjamin-Feir instability.

The HAOs show two different types of patterns. The Type I HAPAs which are especially found for low external resistances and high applied potentials, can be described as an irregular and somewhat cloudy non-stationary modulation of the amplitude, i.e. amplitude turbulence. For higher applied external resistances, clusters in antiphase configuration will form on the WE. We call this state Type II HAPA.

The third group of spatio temporal pattern exhibits spatial features related to both types of oscillations. The first one is a double metastable state, where the dynamics on the WE repeatedly undergo the transition from HAOs to LAOs and then from LAOs to HAOs. This is a process, which typically takes several oscillations as the LAO state slowly spreads across the WE. This process may be accompanied by checkerboard patterns in the 1D-cut, which are often observed during the transition from LAOs to HAOs under reduced illumination. Characteristic for the double metastable state is that once the LAO state spread over the entire electrode the system globally relaxes back to the HAO state. Subsequently, a new LAO nucleus forms and the whole process repeats. We can rationalize this with the picture of the two limit cycles lying on the opposite side of an equistability point, when looking at the nullclines, analogously to the case of two metastable steady states. So far this is, to the best of our knowledge, the first case in which a system switches selforganized between the two limit cycles of a birhythmic system.

Another state displaying dynamics of both types of oscillations is a state, where the WE splits up into two regions, one displaying a Type II HAPA and the other one homogeneous LAOs, locked to half of the dominant frequency of the Type II HAPA region. We suggest that the period-two behaviour in the HAO region and the locking of the LAOs to this dynamics might stabilise the front between the two states.

We found that the resistance seems to be merely responsible for introducing the temporal complexity to the oscillations by coupling the two limit cycles with each other, like we have already demonstrated for p-doped WEs. Otherwise, the linear global coupling it induces, has an homogenizing effect on the patterns. In contrast, reducing the illumination intensity down to the point where the valence band holes available for the oxidation step are limited might induce pattern formation. We showed that the coherence on the WE decreases with decreasing illumination intensity. Overall it seems that the two limit cycles are intrinsically coupled via the external resistance which has a strong influence on their temporal behaviour and periodicity. However an adequate reduction of the valence band holes introduces an additional degree of freedom which allows a lateral redistribution of the charge carriers in the space charge layer and thus the potential landscape, which in turn has an effect on the local dynamics. This introduces a nonlinear nonlocal coupling, which seems to be responsible for the spatial symmetry breaking.

To further elucidate the interaction between the two limit cycles, and thus the coupling introduced by the external resistance, it might be helpful to conduct phase response measurements during zero external resistance oscillations as well as simple periodic LAOs and HAOs, such that the response of the system towards potential perturbations in each phase can be better understood. In a next step, experiments could be conducted which introduce a periodic forcing via the applied potential to see in what way the system deviates from periodic motion and if states similar to the complex dynamics presented for p-doped silicon can be enforced. This should be done under homogenous conditions, probably with p-doped WEs. Since the pattern formation seems to arise from a spatial symmetry breaking of the potential landscape at the Si surface, a deep understanding of the behaviour of the system towards potential perturbations should be helpful to understand the processes which lead to the different kinds of patterns.

We already know that the HAOs do not seem to react sensitively towards potential perturbations but the LAOs do [64, 102]. Similar behaviour has been demonstrated in phase response measurements during the electrodissolution of Nickel electrodes, where the system was particularly unresponsive in the linear deactivation region of the relaxation oscillations [45]. The authors could show, that it is especially the relaxational character of the oscillations, which leads to antiphase clusters. This is in line with our experimental results, as antiphase clusters are merely found in HAO states. In addition the phase response curves during homogenous HAOs should be measured to see if similar conclusions as in [45] can be drawn. If this would be the case, a result of this would be, that the amount of clusters found on the WE should depend on the extent of the relaxational character. It is likely that the relaxational character of HAOs measured with electrolytes with a much slower etch rate is more distinct, as relaxation oscillations arise due to a separation of the time scales of the processes involved in the oscillation mechanism. Thus, it could be investigated if the amount of clusters can be controlled via the composition of the electrolyte.

To further elucidate the nonlinear nonlocal coupling, one could use n-doped Si WE with different doping levels, which should have an affect on the diffusion length of the charge carriers in the semiconductor. Thus, conclusions on the range of the nonlocal coupling and the resulting types and dimensions of the different patterns could be drawn.

BIBLIOGRAPHY

[1] M. [Sbreve]KEREN, I. RICHTER and P. FIALA. 'Iterative Fourier transform algorithm: comparison of various approaches'. In: *Journal of Modern Optics* 49.11 (2002), pp. 1851–1870. DOI: `10.1080/09500340210140542`.

[2] V. Afraimovich and L. P. Shilnikov. 'Invariant two-dimensional tori, their breakdown and stochasticity'. In: *Amer. Math. Soc. Transl* 149.2 (1991), pp. 210–212.

[3] V. Afraimovich and L. Shilnikov. 'On invariant two-dimensional tori, their disintegration and stochasticity'. In: *Methods of the qualitative theory of differential equations, Gos. Univ. Gorkij, Gor'kov* (1983).

[4] M. Alamgir and I. R. Epstein. 'Birhythmicity and Compound Oscillation in Coupled Chemical Oscillators: Chlorite-Bromate-Iodide System'. In: *Journal of the American Chemical Society* 105.8 (Apr. 1983), pp. 2500–2502. ISSN: 15205126. DOI: `10.1021/ja00346a080`.

[5] M. Alamgir and I. R. Epstein. 'Systematic design of chemical oscillators. Part 19. Experimental study of complex dynamical behavior in coupled chemical oscillators'. In: *J. Phys. Chem.* 88.13 (June 1984), pp. 2848–2851. ISSN: 0022-3654. DOI: `10.1021/j150657a036`.

[6] F. T. Arecchi, R. Meucci, G. Puccioni and J. Tredicce. 'Experimental Evidence of Subharmonic Bifurcations, Multistability, and Turbulence in a Q-Switched Gas Laser'. In: *Phys. Rev. Lett.* 49.17 (1982), pp. 1217–1220. ISSN: 0031-9007. DOI: `10.1103/PhysRevLett.49.1217`.

[7] J. Argyris. *Die Erforschung des Chaos : Eine Einführung in die Theorie Nichtlinearer Systeme*. Heidelberg, Dordrecht, London, New York: Springer, 2010. ISBN: 978-3-540-71071-4.

[8] O. V. Astakhov, S. V. Astakhov, N. S. Krakhovskaya, V. V. Astakhov and J. Kurths. 'The emergence of multistability and chaos in a two-mode van der Pol generator versus different connection types of linear oscillators'. In: *Chaos* 063118 (2018). ISSN: 1054-1500. DOI: `10.1063/1.5002609`.

[9] M. Bär, N. Gottschalk, M. Eiswirth and G. Ertl. 'Spiral waves in a surface reaction: model calculations'. In: *The Journal of chemical physics* 100.2 (1994), pp. 1202–1214.

[10] J. A. Bardwell, E. M. Allegretto, J. Phillips, M. Buchanan and N. Draper. 'Influence of the Initial Electrochemical Potential on the Growth Mechanism and Properties of Anodic Oxides on (100) Si'. In: *Journal of The Electrochemical Society* 143.9 (1996), pp. 2931–2938. ISSN: 0013-4651. DOI: 10.1149/1.1837129.

[11] J. A. Bardwell, N. Draper and P. Schmuki. 'Growth and characterization of anodic oxides on Si(100) formed in 0.1 M hydrochloric acid'. In: *Journal of Applied Physics* 79.11 (1996), pp. 8761–8769. ISSN: 00218979. DOI: 10.1063/1.362502.

[12] J. A. Bardwell, P. Schmuki, G. I. Sproule, D. Landheer and D. F. Mitchell. 'Physical and Electrical Characterization of Thin Anodic Oxides on Si(100)'. In: *Journal of The Electrochemical Society* 142.11 (1995), pp. 3933–3940. ISSN: 0013-4651. DOI: 10.1149/1.2048437.

[13] D. Battogtokh and J. J. Tyson. 'Turbulence near cyclic fold bifurcations in birhythmic media'. In: *Physical Review E - Statistical Physics, Plasmas, Fluids, and Related Interdisciplinary Topics* 70.2 (Aug. 2004), p. 7. ISSN: 1063651X. DOI: 10.1103/PhysRevE.70.026212.

[14] D. L. Baulch, J. F. Griffiths, A. J. Pappin and A. F. Sykes. 'Stationary-state and oscillatory combustion of hydrogen in a well-stirred flow reactor'. In: *Combust. Flame* 73.2 (Aug. 1988), pp. 163–185. ISSN: 00102180. DOI: 10.1016/0010-2180(88)90044-2.

[15] T. Bem and J. Rinzel. 'Short duty cycle destabilizes a half-center oscillator, but gap junctions can restabilize the anti-phase pattern'. In: *Journal of Neurophysiology* 91.2 (2004), pp. 693–703.

[16] D. Biswas, T. Banerjee and J. Kurths. 'Control of birhythmicity through conjugate self-feedback: Theory and experiment'. In: *Physical Review E* 94.4 (2016), pp. 1–7. ISSN: 24700053. DOI: 10.1103/PhysRevE.94.042226.

[17] D. Biswas, T. Banerjee and J. Kurths. 'Control of birhythmicity: A self-feedback approach'. In: *Chaos* 27.6 (2017). ISSN: 10541500. DOI: 10.1063/1.4985561.

[18] D. J. Blackwood, A. M. Borazio, R. Greef, L. M. Peter and J. Stumper. 'Electrochemical and optical studies of silicon dissolution in ammonium fluoride solutions'. In: *Electrochimica Acta* 37.5 (1992), pp. 889–896. ISSN: 00134686. DOI: 10.1016/0013-4686(92)85040-R.

[19] V. Booth and J. Rinzel. 'A minimal, compartmental model for a dendritic origin of bistability of motoneuron firing patterns'. In: *Journal of computational neuroscience* 2.4 (1995), pp. 299–312.

[20] Y. Boudinar, K. Belmokre, M. Touzet, O. Devos and M. Puiggali. ‘Investigation of the passivation process of plastically deformed 316L stainless steel using the high frequency capacitance obtained by EIS’. In: *Materials and Corrosion* 70.2 (2019), pp. 206–215. ISSN: 15214176. DOI: 10.1002/maco.201810094.

[21] H. Broer. ‘Perspectives on the legacy of Poincaré in the field of dynamical systems’. In: *Nieuw Archief voor Wiskunde* 5.13 (2012), p. 3.

[22] S. Cattarin, I. Frateur, M. Musiani and B. Tribollet. ‘Electrodissolution of p-Si in Acidic Fluoride Media Modeling of the Steady State’. In: *Journal of The Electrochemical Society* 147.9 (2000), p. 3277. ISSN: 00134651. DOI: 10.1149/1.1393895.

[23] J.-N. Chazalviel. ‘Ionic processes through the interfacial oxide in the anodic dissolution of silicon’. In: *Electrochimica Acta* 37.5 (1992), pp. 865–875. ISSN: 00134686. DOI: 10.1016/0013-4686(92)85038-M.

[24] J.-N. Chazalviel, M. Etman and F. Ozanam. ‘A voltammetric study of the anodic dissolution in fluoride electrolytes of p-Si’. In: *J. Electroanal. Chem.* 291 (1991), pp. 533–540.

[25] J.-N. Chazalviel and F. Ozanam. ‘A Theory for the Resonant Response of an Electrochemical System: Self-Oscillating Domains, Hidden Oscillation, and Synchronization Impedance’. In: *Journal of The Electrochemical Society* 139.9 (1992), p. 2501. ISSN: 00134651. DOI: 10.1149/1.2221253.

[26] J.-N. Chazalviel, F. Ozanam, M. Etman, F. Paolucci, L. M. Peter and J. Stumper. ‘The p-Si/fluoride interface in the anodic region: Damped and/or sustained oscillations’. In: *Journal of Electroanalytical Chemistry* 327.1-2 (1992), pp. 343–349. ISSN: 00220728. DOI: 10.1016/0022-0728(92)80160-6.

[27] D. S. Cohen and J. P. Keener. ‘Multiplicity and stability of oscillatory states in a continuous stirred tank reactor with exothermic consecutive reactions A $\rightarrow$ B $\rightarrow$ C’. In: *Chem. Eng. Sci.* 31.2 (1976), pp. 115–122. ISSN: 00092509. DOI: 10.1016/0009-2509(76)85046-4.

[28] O. Decroly and A. Goldbeter. ‘Birhythmicity, chaos, and other patterns of temporal self-organization in a multiply regulated biochemical system.’ In: *Proceedings of the National Academy of Sciences* 79.22 (1982), pp. 6917–6921. ISSN: 0027-8424. DOI: 10.1073/pnas.79.22.6917.

[29] M. J. Eddowes. ‘Anodic dissolution of p- and n-type silicon: Kinetic study of the chemical mechanism’. In: *Journal of Electroanalytical Chemistry and Interfacial Electrochemistry* 280.2 (1990), pp. 297–311. ISSN: 00220728. DOI: 10.1016/0022-0728(90)87005-5.

[30] M. J. Feigenbaum. 'Quantitative universality for a class of nonlinear transformations'. In: *Journal of Statistical Physics* 19.1 (1978), pp. 25–52. ISSN: 00224715. DOI: `10.1007/BF01020332`.

[31] E. Foca, J. Carstensen and H. Föll. 'Modelling electrochemical current and potential oscillations at the Si electrode'. In: *Journal of Electroanalytical Chemistry* 603.2 (2007), pp. 175–202. ISSN: 00220728. DOI: `10.1016/j.jelechem.2007.01.019`.

[32] H. Föll, M. Leisner, A. Cojocaru and J. Carstensen. 'Self-organization phenomena at semiconductor electrodes'. In: *Electrochimica Acta* 55.2 (2009), pp. 327–339. ISSN: 00134686. DOI: `10.1016/j.electacta.2009.03.076`.

[33] D. Gabor. 'Theory of communication. Part 1: The analysis of information'. In: *J. Inst. Electr. Eng. - Part III Radio Commun. Eng.* 93.26 (Nov. 1946), pp. 429–441. ISSN: 2054-0604. DOI: `10.1049/ji-3-2.1946.0074`.

[34] V. García-Morales and K. Krischer. 'The complex Ginzburg–Landau equation: an introduction'. In: *Contemporary Physics* 53.2 (2012), pp. 79–95.

[35] V. García-Morales, J. A. Manzanares and K. Krischer. 'Chimera states under genuine local coupling'. In: *Chaos, Solitons & Fractals* 165 (2022), p. 112808.

[36] F. Gaspard, A. Bsiesy, M. Ligeon, F. Muller and R. Herino. 'Charge Exchange Mechanism Responsible for P-Type Silicon Dissolution during Porous Silicon Formation'. In: *J. Electrochem. Soc.* 136.10 (1989), pp. 3043–3046. ISSN: 0013-4651. DOI: `10.1149/1.2096399`.

[37] A. Gerrard and J. Burch. *Introduction to Matrix Methods in Optics*. Dover Books on Physics. Dover, 1994. ISBN: 9780486680446.

[38] A. Goldbeter and J. Yan. 'Multi-synchronization and other patterns of multi-rhythmicity in oscillatory biological systems'. In: *Interface Focus* 12.3 (2022), p. 20210089.

[39] B. F. Gray and J. C. Jones. 'The heat release rates and cool flames of acetaldehyde oxidation in a continuously stirred tank reactor'. In: *Combust. Flame* 57.1 (July 1984), pp. 3–14. ISSN: 00102180. DOI: `10.1016/0010-2180(84)90132-9`.

[40] M. Guevara, A. Shrier and L. Glass. 'Chaotic and complex cardiac rhythms'. In: *Cardiac electrophysiology: from cell to bedside* (1990), pp. 192–201.

[41] A. Heinrich. 'Mechanistische und dynamische Eigenschaften der Elektrodissolution von Silizium'. Master's thesis. Technische Universität München, 2013.

[42] R. Hueck. 'From Subcritical to Strong Nonlinear Spatial Coupling during Electrodissolution of n-type Si : Phase Waves , Frequency Clusters and Tristability'. Master's Thesis. Technische Universität München, 2017.

[43] B. R. Johnson, J. F. Griffiths and S. K. Scott. 'Characterisation of oscillations in the H2+ O2reaction in a continuous-flow reactor'. In: *Journal of the Chemical Society, Faraday Transactions* 87.4 (1991), pp. 523–533. ISSN: 09565000. DOI: 10.1039/FT9918700523.

[44] J. S. Judge. 'A Study of the Dissolution of SiO[sub 2] in Acidic Fluoride Solutions'. In: *Journal of The Electrochemical Society* 118.11 (1971), p. 1772. DOI: 10.1149/1.2407835.

[45] I. Z. Kiss, Y. Zhai and J. L. Hudson. 'Predicting mutual entrainment of oscillators with experiment-based phase models'. In: *Physical review letters* 94.24 (2005), p. 248301.

[46] K. Krischer. 'Modern Aspects of Electrochemistry: Principles of Temporal and Spatial Pattern Formation in Electrochemical Systems'. In: *Modern Aspects of Electrochemistry, No. 32*. Ed. by B. E. et al Conway. Vol. 213. Part_2. Kluwer Academic/ Plenum Publisher, 1999. Chap. 1, pp. 216–217.

[47] Y. Kuramoto. *Chemical Oscillations, Waves, and Turbulence*. Dover Publications, Inc. (Mineola, New York), 1984. ISBN: 9783642126000. DOI: 10.1007/978-3-642-12601-7.

[48] P. Lamba and J. L. Hudson. 'Experimental Evidence of Multiple Oscillatory States in a Continuous Reactor'. In: *Chem. Eng. Commun.* 32.6 (Jan. 1985), pp. 369–375. ISSN: 0098-6445. DOI: 10.1080/00986448508911657.

[49] J. L. Laugesen, E. Mosekilde and Z. T. Zhusubaliyev. 'Bifurcation structure of the C-type period-doubling transition'. In: *Physica D: Nonlinear Phenomena* 241.5 (2012), pp. 488–496. ISSN: 01672789. DOI: 10.1016/j.physd.2011.11.004.

[50] V. Lehmann. 'The Physics of Macropore Formation in Low Doped n-Type Silicon'. In: *Journal of The Electrochemical Society* 140.10 (1993), p. 2836. ISSN: 00134651. DOI: 10.1149/1.2220919.

[51] V. Lehmann and H. Föll. 'Formation Mechanism and Properties of Electrochemically Etched Trenches in n-Type Silicon'. In: *Journal of The Electrochemical Society* 137.2 (Feb. 1990), p. 653. DOI: 10.1149/1.2086525.

[52] M. Levi, F. C. Hoppensteadt and W. Miranker. 'Dynamics of the Josephson junction'. In: *Quarterly of Applied Mathematics* 36.2 (1978), pp. 167–198.

[53] H. J. Lewerenz. 'Spatial and temporal oscillation at Si (111) electrodes in aqueous fluoride-containing solution'. In: *The Journal of Physical Chemistry B* 5647.111 (1997), pp. 2421–2425. ISSN: 1520-6106. DOI: 10.1021/jp962694x.

[54] J. Maselko and H. L. Swinney. 'Complex periodic oscillations and Farey arithmetic in the Belousov–Zhabotinskii reaction'. In: *J. Chem. Phys.* 85.11 (1986), pp. 6430–6441. ISSN: 0021-9606. DOI: `10.1063/1.451473`.

[55] R. Memming and G. Schwandt. 'Anodic dissolution of silicon in hydrofluoric acid solutions'. In: *Surface Science* 4.2 (1966), pp. 109–124.

[56] I. Miethe. 'Spatio-temporal pattern formation during the anodic electrodissolution of silicon in ammonium fluoride solution'. PhD thesis. Technische Universität München, 2010.

[57] I. Miethe, V. García-Morales and K. Krischer. 'Irregular Subharmonic Cluster Patterns in an Autonomous Photoelectrochemical Oscillator'. In: *Physical Review Letters* 102.19 (2009), pp. 94–101. ISSN: 00319007. DOI: `10.1103/PhysRevLett.102.194101`.

[58] I. Miethe and K. Krischer. 'Ellipsomicroscopic studies of the anodic oxidation of p-type silicon in fluoride containing electrolytes during current oscillations'. In: *Journal of Electroanalytical Chemistry* 666 (2012), pp. 1–10. ISSN: 15726657. DOI: `10.1016/j.jelechem.2011.11.027`.

[59] E. Mitterreiter. 'Characterization and Parameter Dependence of Current Spikes Occuring During the Illumination-Limited, Oscillatory Electrodissolution of n-Type Silicon'. 2013.

[60] Y. Murakami. 'Controlling Patterns with a Spatial Light Modulator during Si Electrodissolution'. Master's Thesis. Technische Universität München, 2021.

[61] S. Newhouse, D. Ruelle and F. Takens. 'Occurrence of strange Axiom A attractors near quasi periodic flows on Tm, m≧3'. In: *Communications in Mathematical Physics* 64.1 (1978), pp. 35–40. ISSN: 00103616. DOI: `10.1007/BF01940759`.

[62] I. Newton, A. Motte and J. Machin. *The Mathematical Principles of Natural Philosophy*. The Mathematical Principles of Natural Philosophy v. 1. B. Motte, 1729.

[63] M. Patzauer. *Multistability in the Oscillatory Electrodissolution of Silicon*. 2016.

[64] M. Patzauer. 'ON EMERGENT BEHAVIOUR DURING THE OSCILLATORY ELECTRODISSOLUTION OF SILICON'. Doctor Thesis. Technical University Munich, 2022.

[65] M. Patzauer, R. Hueck, A. Tosolini, K. Schönleber and K. Krischer. 'Autonomous Oscillations and Pattern Formation with Zero External Resistance during Silicon Electrodissolution'. In: *Electrochim. Acta* 246 (Aug. 2017), pp. 315–321. ISSN: 00134686. DOI: `10.1016/j.electacta.2017.06.005`.

[66] M. Patzauer and K. Krischer. 'Self-organized Multi-Frequency Clusters in an Oscillating Electrochemical System with Strong Nonlinear Coupling'. 2020.

[67] M. Patzauer and K. Krischer. 'Self-Organized Multifrequency Clusters in an Oscillating Electrochemical System with Strong Nonlinear Coupling'. In: *Phys. Rev. Lett.* 126.19 (May 2021), p. 194101. ISSN: 0031-9007. DOI: `10.1103/PhysRevLett.126.194101`.

[68] J. S. Pendergast, K. D. Niswender and S. Yamazaki. 'The complex relationship between the light-entrainable and methamphetamine-sensitive circadian oscillators: evidence from behavioral studies of Period -mutant mice'. In: *Eur. J. Neurosci.* 38.7 (July 2013), pp. 3044–3053. ISSN: 0953816X. DOI: `10.1111/ejn.12309`.

[69] R. Perez and L. Glass. 'Bistability, period doubling bifurcations and chaos in a periodically forced oscillator'. In: *Physics Letters A* 90.9 (1982), pp. 441–443.

[70] A. Pikovsky, M. Rosenblum and J. Kurths. *Synchronization*. Cambridge University Press, 2001. ISBN: 9780521533522. DOI: `10.1017/CBO9780511755743`.

[71] A. N. Pisarchik and U. Feudel. 'Control of multistability'. In: *Phys. Rep.* 540.4 (July 2014), pp. 167–218. ISSN: 03701573. DOI: `10.1016/j.physrep.2014.02.007`.

[72] H. Poincaré. 'Mémoire sur les courbes définies par une équation différentielle (2nde partie)'. In: *Journal de mathématiques pures et appliquées* 8 (1882), pp. 251–296.

[73] H. Poincaré. *New methods of celestial mechanics*. Vol. 2. National Aeronautics and Space Administration, 1967.

[74] J. Proost, F. Blaffart, S. Turner and H. Idrissi. 'On the Origin of Damped Electrochemical Oscillations at Silicon Anodes (Revisited)'. In: *ChemPhysChem* 15.14 (2014), pp. 3116–3124. ISSN: 14397641. DOI: `10.1002/cphc.201402207`.

[75] J. Proost, F. Blaffart, S. Turner and H. Idrissi. 'On the Origin of Damped Electrochemical Oscillations at Silicon Anodes (Revisited)'. In: *ChemPhysChem* 15.14 (2014), pp. 3116–3124. ISSN: 14397641. DOI: `10.1002/cphc.201402207`.

[76] A. Provata. 'Chimera states formed via a two-level synchronization mechanism'. In: *J. Phys. Complex.* 1.2 (July 2020), p. 25006. ISSN: 2632-072X. DOI: `10.1088/2632-072X/ab79bd`.

[77] J.-C. Roux. 'Experimental studies of bifurcations leading to chaos in the Belousof-Zhabotinsky reaction'. In: *Phys. D Nonlinear Phenom.* 7.1-3 (1983), pp. 57–68. ISSN: 01672789. DOI: `10.1016/0167-2789(83)90115-X`.

[78] F. Rueller, D and Takens. ‘On the Nature of Turbulence, common. Math. Phys., 20,167-192’. In: *Nature* (1971).

[79] M. Schell, S. Fraser and R. Kapral. ‘Subharmonic bifurcation in the sine map: An infinite hierarchy of cusp bistabilities’. In: *Physical Review A* 28.1 (1983), pp. 373–378. ISSN: 10502947. DOI: `10.1103/PhysRevA.28.373`.

[80] L. Schmidt, K. Schönleber, V. García-Morales and K. Krischer. ‘Unusual synchronization phenomena during electrodissolution of silicon: the role of nonlinear global coupling’. In: *Engineering of Chemical Complexity II* 12 (2014), pp. 239–260. DOI: `10.1142/9789814616133_0014`.

[81] L. Schmidt, K. Schönleber, K. Krischer and V. García-Morales. ‘Coexistence of synchrony and incoherence in oscillatory media under nonlinear global coupling’. In: *Chaos (Woodbury, N.Y.)* 24.1 (2014), p. 13102. ISSN: 10897682. DOI: `10.1063/1.4858996`.

[82] P. Schmuki, H. Böhni and J. A. Bardwell. ‘In Situ Characterization of Anodic Silicon Oxide Films by AC Impedance Measurements’. In: *Journal of The Electrochemical Society* 142.5 (1995), pp. 1705–1712. ISSN: 0013-4651. DOI: `10.1149/1.2048644`.

[83] K. Schönleber. ‘Self-organization phenomena during the electrodissolution of silicon’. PhD thesis. Technische Universität München, 2015.

[84] K. Schönleber and K. Krischer. ‘High-amplitude versus low-amplitude current oscillations during the anodic oxidation of p-type silicon in fluoride containing electrolytes’. In: *Chem. Phys. Chem.* 13.12 (Aug. 2012), pp. 2989–2996. ISSN: 14394235. DOI: `10.1002/cphc.201200230`.

[85] K. Schönleber, M. Patzauer and K. Krischer. ‘A comparison of modeling frameworks for the oscillatory silicon electrodissolution’. In: *Electrochim. Acta* 210 (Aug. 2016), pp. 346–351. ISSN: 00134686. DOI: `10.1016/j.electacta.2016.05.144`.

[86] K. Schönleber, C. Zensen, A. Heinrich and K. Krischer. ‘Pattern formation during the oscillatory photoelectrodissolution of n-type silicon: Turbulence, clusters and chimeras’. In: *New Journal of Physics* 16.6 (June 2014), p. 63024. ISSN: 13672630. DOI: `10.1088/1367-2630/16/6/063024`.

[87] O. Sporns, S. Roth and F. F. Seelig. ‘Chaotic dynamics of two coupled biochemical oscillators’. In: *Physica D: Nonlinear Phenomena* 26.1 (1987), pp. 215–224. ISSN: 0167-2789. DOI: `https://doi.org/10.1016/0167-2789(87)90226-0`.

[88] K. Srinivasan and G. A. Rechnitz. ‘Activity measurements with a fluoride-selective membrane electrode’. In: *Analytical Chemistry* 40.3 (1968), pp. 509–512.

[89] M. Stich, M. Ipsen and A. S. Mikhailov. 'Self-organized stable pacemakers near the onset of birhythmicity'. In: *Physical Review Letters* 86.19 (2001), pp. 4406–4409. ISSN: 00319007. DOI: `10.1103/PhysRevLett.86.4406`.

[90] M. Stich, M. Ipsen and A. S. Mikhailov. 'Self-organized pacemakers in birhythmic media'. In: *Physica D: Nonlinear Phenomena* 171.1-2 (2002), pp. 19–40. ISSN: 01672789. DOI: `10.1016/S0167-2789(02)00549-3`.

[91] M. Stich and A. S. Mikhailov. 'Complex pacemakers and wave sinks in heterogeneous oscillatory chemical systems'. In: *Zeitschrift fur Phys. Chemie* 216.4 (2002), pp. 521–533. ISSN: 00443336. DOI: `10.1524/zpch.2002.216.4.521`.

[92] S. H. Strogatz. *Nonlinear {D}ynamics and {C}haos : with {A}pplications to {P}hysics, {B}iology, {C}hemistry, and {E}ngineering*. Boulder, CO: Westview Press, a member of the Perseus Books Group, 2015. ISBN: 9780813349114.

[93] S. T. Sulaiman. 'The Growth and Investigation of Interface of SiO 2 / Si by Anodic Oxidation Technique Using Acetic Acid Medium'. In: 23.4 (2012), pp. 117–126.

[94] A. Tosolini. 'Characterization of Multiple Bifurcation Scenarios during the Electrodissolution of p-Type Si in Fluoride Containing Electrolytes'. Master's Thesis. Technische Universität München, 2017.

[95] A. Tosolini, M. Patzauer and K. Krischer. 'Bichaoticity induced by inherent birhythmicity during the oscillatory electrodissolution of silicon'. In: *Chaos* 29.4 (Apr. 2019), p. 043127. ISSN: 1054-1500. DOI: `10.1063/1.5090118`.

[96] D. R. Turner. 'Electropolishing Silicon in Hydrofluoric Acid Solutions'. In: *J. Electrochem. Soc.* 105.7 (1958), pp. 402–408. ISSN: 00134651. DOI: `10.1149/1.2428873`.

[97] A. Uhlir. 'Electrolytic Shaping of Germanium and Silicon'. In: *Bell System Technical Journal* 35.2 (1956), pp. 333–347. ISSN: 15387305. DOI: `10.1002/j.1538-7305.1956.tb02385.x`.

[98] W. Vance and J. Ross. 'A detailed study of a forced chemical oscillator: Arnol'd tongues and bifurcation sets'. In: *The Journal of Chemical Physics* 91.12 (1989), pp. 7654–7670. ISSN: 00219606. DOI: `10.1063/1.457235`.

[99] X.-J. Wang and J. Rinzel. 'Alternating and synchronous rhythms in reciprocally inhibitory model neurons'. In: *Neural computation* 4.1 (1992), pp. 84–97.

[100] R. Westfall. *Never at Rest: A Biography of Isaac Newton*. Cambridge paperback library. Cambridge University Press, 1983. ISBN: 9780521274357.

[101] J. Wiehl. 'Birhythmicity and Intrinsic Entrainment in a Diffusively Coupled Oscillatory System: An Experimental Study'. Master's Thesis. Technische Universität München, 2020.

[102] J. C. Wiehl, M. Patzauer and K. Krischer. 'Birhythmicity, intrinsic entrainment, and minimal chimeras in an electrochemical experiment'. Submitted to *Chaos*. July 2021.

[103] R. Yamapi, G. Filatrella and M. A. Aziz-Alaoui. 'Global stability analysis of birhythmicity in a self-sustained oscillator'. In: *Chaos* 20.1 (2010). ISSN: 10541500. DOI: 10.1063/1.3309014.

[104] A. R. Yehia, D. Jeandupeux, F. Alonso and M. R. Guevara. 'Hysteresis and bistability in the direct transition from 1: 1 to 2: 1 rhythm in periodically driven single ventricular cells'. In: *Chaos: An Interdisciplinary Journal of Nonlinear Science* 9.4 (1999), pp. 916–931.

[105] A. Yeldesbay, A. Pikovsky and M. Rosenblum. 'Chimeralike states in an ensemble of globally coupled oscillators'. In: *Physical Review Letters* 112.14 (2014), p. 144103. ISSN: 10797114. DOI: 10.1103/PhysRevLett.112.144103.

[106] A. Zakharova, M. Kapeller and E. Schöll. 'Amplitude chimeras and chimera death in dynamical networks'. In: *Journal of Physics: Conference Series*. Vol. 727. 1. IOP Publishing. 2016, p. 012018.

[107] C. Zensen. 'Mechanism of Oscillation and Spatio-temporal Pattern Formation in a Semiconductor Electrochemical System'. PhD thesis. Technische Universität München, 2013.

[108] H. Zhang, J. Xie, J. Liu and Y. Wang. 'Elimination of a zero-order beam induced by a pixelated spatial light modulator for holographic projection.' In: *Applied optics* 48.October (2009), pp. 5834–5841. ISSN: 0003-6935. DOI: 10.1364/AO.48.005834.

[109] X. G. Zhang. *Electrochemistry of Silicon and Its Oxide*. Boston: Kluwer Academic Publishers, 2004, p. 510. ISBN: 0-306-46541-8. DOI: 10.1007/b100331.